8-2021

Effect of Deposition Conditions on Properties of Molybdenum Back Electrode for Cu(In,Ga)Se2 Solar Cell and Cu(In,Ga)Se2 Performance Analysis through Numerical Simulation

Meah Imtiaz Zulkarnain
The University of Texas Rio Grande Valley

EFFECT OF DEPOSITION CONDITIONS ON PROPERTIES OF MOLYBDENUM BACK ELECTRODE FOR $Cu(In,Ga)Se_2$ SOLAR CELL AND $Cu(In,Ga)Se_2$ PERFORMANCE ANALYSIS THROUGH NUMERICAL SIMULATION

A Thesis

by

MEAH IMTIAZ ZULKARNAIN

Submitted to the Graduate College of
The University of Texas Rio Grande Valley
In partial fulfillment of the requirements for the degree of

MASTER OF SCIENCE IN ENGINEERING

August 2021

Major Subject: Electrical Engineering

EFFECT OF DEPOSITION CONDITIONS ON PROPERTIES OF MOLYBDENUM BACK ELECTRODE FOR $Cu(In,Ga)Se_2$ SOLAR CELL AND $Cu(In,Ga)Se_2$ PERFORMANCE ANALYSIS THROUGH NUMERICAL SIMULATION

A Thesis
by
MEAH IMTIAZ ZULKARNAIN

COMMITTEE MEMBERS

Dr. Nazmul Islam
Chair of Committee

Dr. Hasina Huq
Committee Member

Dr. Heinrich Foltz
Committee Member

August 2021

ABSTRACT

Zulkarnain, Meah Imtiaz, Effect of Deposition Conditions on Properties of Molybdenum Back Electrode for Cu(In,Ga)Se_2 Solar Cell and Cu(In,Ga)Se_2 Performance Analysis through Numerical Simulation. Master of Science in Engineering (MSE), August, 2021, 120 pp., 24 tables, 70 figures, 76 references.

In the first part of this research, effect of the deposition conditions on properties of molybdenum thin-film were investigated to achieve desired characteristics for its application as the back electrode of Cu(In,Ga)Se_2 solar cell. DC and RF magnetron sputtering modes were employed and two sputtering parameters namely, working pressure and sputtering power, were varied to determine the sputtering mode and the sputtering conditions best suited for Mo thin-films having required properties. Sputtered Mo samples were characterized to determine their structural and mechanical properties such as preferred growth orientation, crystallinity, grain size, dislocation density, adhesion, and micro strain, and electrical property such as sheet resistance. DC sputtering mode, lower working pressure and higher sputtering power yielded single layer Mo thin-films with better properties in general. The single layer Mo thin-films with desired characteristics were then utilized to fabricate bilayer and tri-layer Mo thin-films for further simultaneous improvement of properties such as lower sheet resistance and better adhesion of the films to the substrate along with other features. The all-DC sputtered bilayer andthe DC sputtered single layer Mo thin-film which was deposited under lower working pressure exhibited the best of the characteristics required to employ the films as back contact of

CIGS solar cell. The RF sputtered single layer Mo thin-film deposited under lower working pressure remained very close to above two in terms of desired characteristics. The best of the tri-layer Mo thin-films- all-DC and all-RF sputtered- displayed inferior properties compared to the best of the single layer and bilayer Mo thin-film samples.

In the second part of this research, numerical simulation and analysis of CIGS solar cell were conducted to optimize its performance and compare among the cells using different materials for buffer and window layers. The one-dimensional solar cell simulation program SCAPS-1D (Solar Cell Capacitance Simulator) was used for simulation and analysis purposes. CdS and In_2S_3 for the buffer layer, and ZnO and SnO_2 for the window layer were considered to generate different CIGS cell structures. The effects of variation of bandgap, concentration, and thickness of these materials along with p-type CIGS absorber layer were investigated. Besides the solar cell efficiency, the open-circuit voltage, short-circuit current density, fill factor and quantum efficiency of the cell structures were observed from the simulation. The change in cell efficiency with variation in temperature was studied, too. A comparison among the different CIGS cell structures employing different buffer and window materials was performed. The performance of the modeled cell structures was put to comparison against some laboratory research cell, too. All simulated CIGS structures showed better performance compared to the laboratory cells. In_2S_3 appeared to increase efficiency and thus posed a great potential for non-toxic CIGS solar cells. Though the CIGS absorber layer required more thickness for desired output, the successful application of thinner SnO_2 replacing the ZnO buffer layer can pave the way to less thick CIGS thin film solar cells.

DEDICATION

To my parents- my mother Ayesha Begum and my father Meah Mohammad Esmayeel. All what I am today and all that I have achieved till this day would not have been possible without my parents' unconditional love, endless prayer, countless sacrifices, and absolute support.

To my sisters- Sharmeen Sayema Zakia, Saleha Sarowat Sakeeba and Sumaiya Naznee. Their support and care have played a vital role not only throughout my higher study expedition but over my whole life, too.

ACKNOWLEDGMENT

All praise is due to the Almighty that I am standing on the verge of graduating after two years' hectic journey. I would like to express my heartfelt gratitude toward my supervisor, Professor Nazmul Islam, Ph.D., for his immense support and guidance throughout my MS program here at UTRGV. His support and monitoring were the key behind the completion of this work. Besides supervising research, his mentorship in and out of classroom and laboratory proved invaluable numerous times. I am very much grateful to Dr. Hasina Huq for allowing me to use the sputtering system in her lab. Special mention and thanks go to my colleague Mr. Sajid Mahfuz Uchayash for his tremendous assist in conducting this research. Together we learned to operate the equipment we needed for our experimental work and eventually ended up supporting each other throughout both of our research works. I have learnt a great deal about the sputtering and XRD equipment and their operation from two of my colleagues, Mr. Prosanto Biswas and Mr. Muhtasim Ul Karim Sadaf. I would like this opportunity to thank them for the time and support they provided whenever I needed. Mr. Al Mazedur Rahman and Mr. S M Abdur Rob, another two of my colleagues, also provided cordial support regarding use of the characterization equipment, thanks to them. There are a lot of people here in Edinburg and back in Bangladesh whose support and prayer, I believe, have been crucial for me being here today and looking up to the completion of this thesis book. I am indebted to all of you.

TABLE OF CONTENTS

Page

LIST OF TABLES

Page

LIST OF FIGURES

Page

CHAPTER I

INTRODUCTION

1.1 Solar Energy and Fossil Fuel

Fossil fuel has been proved greatly hazardous to the ecosystem and climate. The amount of CO_2 emission due to fossil fuel use in the earth atmosphere is leading to the global warming at an alarming rate [1, 2]. This is why the quest for clean and sustainable energy is now more necessary and, consequently, more evident than ever in the history of the humankind.

Of the renewable energy resources, solar energy holds the maximum theoretical, extractable and technical potential [3]. In fact, the energy supplied to the earth in one and a half hour by the sun is more than enough to meet the yearly consumption of the whole population of the current world [3]. Such a source of energy- clean, long-lasting if not everlasting, sustainable- remains largely untapped until this day mainly due to geographical, environmental, and technological limitations and complexities.

1.2 Solar Cells and Their Efficiency

Solar cells are used to tap the energy of the light particles i.e. the photons and to convert it into electricity. From hand-held solar cell energized calculator to stand-alone home system to extraterrestrial applications, application of solar cell has found its way to everywhere. The past years have seen a great rise in search for materials suitable for different types of solar cells. A

large variety of fabrication techniques has been employed to fabricate solar cells in order to harvest the maximum of solar energy.

Of the solar cell materials in use, conventional crystalline silicon (C-Si) solar cell is the most extensively employed one. This first generation of solar cell materials holds the biggest share (92% approximately) of the current world market of the photovoltaics [4, 5]. Though it recently has lagged behind one of the second generation solar cell material type in terms of commercial solar module efficiency, the laboratory research efficiency of the C-Si solar cell is still ahead of other types of solar cells [6].

The second generation of the solar cell materials mainly includes the CdTe, the chalcopyrite, the kesterite and the amorphous silicon. Of them, the most promising chalcopyrite compound, copper indium gallium diselenide (Cu(In,Ga)Se2 or CIGS) solar cell, has now a laboratory research cell efficiency of 23.35% [7] close to 26.7% of conventional C-Si solar cell [6]. It beats the CdTe compound (19.2% [8] compared to 18.6% for CdTe solar cells [9]) and lags the C-Si solar cell (24.4% solar module efficiency [6]) in terms of solar module efficiency. Yet, its theoretical efficiency limit of 33.5% surpasses others [10, 11]. The chalcopyrite compound outperforms its kesterite counterpart by a huge difference (23.35% compared to 10% [12]) in terms of laboratory research efficiency and is pushing the limit at a faster rate to exceed that of the conventional C-Si solar cell in near future most probably.

1.3 CIGS Solar Cell

Copper indium Gallium Selenide based solar cell is a promising candidate for solar power technology because it offers following advantages: The absorption coefficients of CIGS is very high. In fact, it has one of the highest known absorption coefficients [13], which makes it a

perfect fit for solar cell application. CIGS is a direct band gap material and the bandgap can be tuned from 1.04 eV to 1.68 eV by adjusting the Ga/In ratio to match the solar spectrum [14]. Due to high absorption co-efficient, CIGS absorber layer is quite thin [1 μm] compared to other types of solar cells [13], results in an overall thinner device reducing cost and raw material usage. Additionally, given the hazards of cadmium extraction and use, CIGS solar cells offer fewer health and environmental concerns than the cadmium telluride solar cells [15]. As illustrated in the paragraph above, there are still scopes to improve the performance of the CIGS solar cell. With further improvement in performance and reliability, CIGS solar cell is very much likely to expand its market share significantly in near future [15].

CIGS solar cell consists of a soda lime glass (SLG) substrate, a molybdenum (Mo) back contact or back electrode, a CIGS absorber layer, a CdS buffer layer, intrinsic ZnO protective layer, Al/Al_2O_3 doped ZnO window layer, as displayed in Figure 1. Each layer of CIGS has a role to play in the working cell and the process of fabrication for each layer will have a direct impact on the efficiency of the device. In the past years, a great deal of research effort has been made to further the efficiency of the CIGS solar cell. Besides applying different fabrication techniques, a range of materials has been employed for every individual layer to maximize the output of the solar cell.

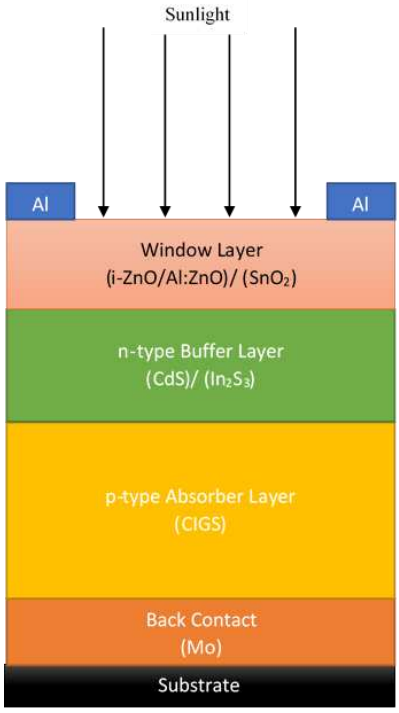

Figure 1.1: Structure of CIGS Solar Cell.

1.4 Molybdenum as the Back Electrode of CIGS Solar Cell

The back contact of the CIGS solar cell acts as a barrier to impede diffusion of impurity to the absorber layer [16], reflects back light to the absorber [17-19] as well as forms an ohmic contact with p-types CIGS absorber material [20]. Other layer of CIGS cells and modules may vary in composition and deposition processes, but the use of sputtered molybdenum (Mo) as a back contact is almost universal [21]. Mo is ideal back contact for CIGS process because of its high conductivity, low resistance contact with the absorber layer, ability of not forming alloy with Cu, low susceptibility to corrosion in a selenium atmosphere, good chemical inertness and thermal stability during the film growth process as well as matching thermal coefficient of expansion with SLG substrate and absorber layers which ensure the device safety while fabrication [16, 20-25]. During selenization process, an intermediate $MoSe_2$ layer is created within back contact and absorber layer which forms a quasi-ohmic transport system between

them and improves adhesion as well [26-30]. Due to wider bandgap of $MoSe_2$ (1.35-1.41 eV), more near infrared light can be absorbed [31]. Additionally, Na ions can diffuse through the Mo back contact into the absorber layer from the soda lime substrate during CIGS deposition; Sodium diffusion helps in formation of a crystalline CIGS film which, in turn has a positive effect on the performance of the solar cell [20, 22, 26, 32-34]. The highest conversion efficiency for CIGS and CZTS thin film solar cell devices has been achieved using Mo as back contacts [19, 35].

Desirable properties of Mo back contact for CIGS solar cells are uniformity, low resistivity, surface smoothness, stress-free, well-adherent, and crystalline molybdenum (Mo) thin films with preferred orientation (110) on substrates [34]. Much of the efficiency of the solar cell depends on how Mo back contact is grown on the substrate, as not only the whole solar cell will be deposited on it but the diffusion of Na from soda lime substrate and creation of the $MoSe_2$ between the absorber layer and back contact is also related to the properties of this film [22, 36, 37]. However, deposition technique (DC or RF) and parameters (sputtering power, working pressure, substrate temperature and target to substrate distance) directly control the properties (crystal structure, grain size, surface morphology, resistivity, stress, reflection) of the back contact; there by altering them, the desired features can be obtained [16, 20, 38, 39].

Despite its suitable characteristics and better performance as back contact material, it faces the problem of mutual exclusivity of better adhesion to the substrate and higher conductivity. To attain both, Mo bilayer might be an excellent option.

1.5 Objective

In the first part of this research, the objective is to explore the effects of sputtering pressure and sputtering power on properties of DC- and RF-sputtered Mo thin-films. The aim is to find out suitable working pressure and sputtering power to obtain Mo thin-film with desired characteristics. For the desired characteristics of the Mo thin-film, the focus will mainly be on three parameters of the film namely, well-grown crystal structure, sheet resistance of the film, and adhesion of the film to the substrate. The single layer Mo thin-films showing optimized characteristics will then be utilized to fabricate Mo bilayer and tri-layer thin-films. The properties of the Mo bilayer and tri-layer thin-films will then be investigated. Finally, the properties of Mo single layer, bilayer and tri-layer thin-films will be compared to identify the films having the best of the desired characteristics.

In the second part of this research, the objective is to maximize the performance of the CIGS solar cell through optimization of different characteristics of different materials used in different layers of the cell structure. For this purpose, different characteristics of p-type CIGS material of the absorber layer, n-type CdS and In2S3 materials for the buffer layer, and ZnO and SnO2 materials for the window layer were optimized. Finally, the output of the optimized CIGS structures will be compared to those of some laboratory-research CIGS solar cell.

CHAPTER II

LITERATURE REVIEW

Earlier works on CIGS solar cell used single layer sputtering technique to form the back contact and focused mainly on the effect of changing sputtering power and working pressure on this layer as they are the most significant parameters that shape the properties of it. When the sputtering power is high, the process gas ions bombard against the target with higher energy, and the excited Mo particles from the target gain higher kinetic energy [16, 31]. Whereas at high pressure, sputtered species undergo more collisions with process gas ions because of the contraction of mean free path, leading to their thermalization and the kinetic energy of the Mo particles decrease. In other words, lowering the pressure ensued in very high energetic bombardment near the surface. This impact process, known as a "peening effect" [26, 34, 36].

2.1 Structural Properties of Sputtered Mo Thin-films

2.1.1 Crystal Structure

The crystalline structural properties of the Mo back contact are generally determined by X-ray diffraction with common source is reported to be Cu-Kα. The XRD patterns having intense peak at $2\theta \approx 40.4^{o}$ are reported in virtually every works, indicating that the Mo thin films crystallize in a body-centered cubic (BCC) crystal structure (ICDD reference No. 004-0809 [20], JCPDS Card no. 3-065-7442 [40-43]), which corresponds to space group symbol and space group number of Im-3 m and 229, respectively [44]. The XRD patterns reveal a dominant (110)

crystal plane orientation through an intense peak [40-43], since the (110) plane possesses the lowest surface energy per unit area [27, 45, 46]. Additional peaks, much weaker compared to the intensity of (110) peak, along (200) crystal plane around $2\theta \approx 58.8°$ [43], (211) crystal plane around $2\theta \approx 73.5°$ and (220) plane around $2\theta \approx 87.5°$ [41] have been observed, too. While the intensity and shift in the position of the (211) peak follow the same trends as those of Mo (110) peak, the intensity of Mo (220) peak increases at 20 mTorr and its position shifts to the higher 2θ/ the right with increasing pressure [41]. At a pressure greater than 6.6 mTorr, the peak corresponding to the (200) crystal plane orientation disappears [43].

As reported in various works, the peaks of the diffraction at (110) increase, become sharper and more intense with increasing of the sputtering power [20, 31] and full width at half maximum (FWHM) of Mo (110) peak decreases [31], which corresponds to the improved crystallinity. Similar results have been derived with lowering the working pressure [16, 40-43]. The kinetic energy of the sputtered molecules from the target is highly connected with the crystalline properties of Mo back contact. Lower working gas pressure (higher gas power) causes lesser scattering effect and results in high energetic bombardment of the target atom on the substrate surface (atomic peening), which facilitates atomic mobility for the diffusion and micro-void fill up, thus creating a conducive requirement for better crystallinity [34]. Likewise, higher sputtering power energizes the target atoms towards substrate surface and improves crystallinity. However, [47] reported that re-sputtering effects and large number of ion-defects occur due to intense bombardment when the working pressure in decreased beyond a certain limit which leads to poorer crystallinity.

The Full width at Half Maximum (FWHM) at Mo (110) orientation decreases [48] and the grain size increases [48, 49] with decreasing working pressure. This is well proved by [26].

They varied the pressure from 2.5 mTorr to 20 mTorr and saw a gradual decrease a grain size. Lattice constant also increase though not gradually with increasing pressure, indicating a less dense structure. At lower sputtering working pressure, there are fewer collisions among the sputtered Mo particles and the sputtering gas Ar atoms and consequently, less Mo ion scattering. The sputtered Mo ions possess higher mean free time between consecutive collisions which results in greater mean free flight path for the sputtered Mo particles. As a result, the Mo particles arriving on the substrate come with larger kinetic energy [40, 42, 43, 49]. When the Mo particles hit the glass substrate, their kinetic energy is converted into thermal energy [43]. The higher the kinetic energy possessed by the sputtered Mo ions with decrease in sputtering pressure, the more thermal energy is produced. The grain nucleation thus is enhanced due to the higher thermal energy and so is the growth of the Mo thin film [26, 43]. At very low pressure (< 3mTorr), however, though the grain size was bigger, the lattice constant is also greater, which suggests that lowering the working pressure a particular limit, a loose microstructure of bigger grain size is formed [26]. This is because of the intense bombardment resulting the re-sputtering effect and large number of ion defects [47]. On the other hand, the collision frequency between the Ar sputtering gas ions and sputtered Mo particles increase with increase in sputtering gas pressure. So, the kinetic energy of the ejected Mo ions gets largely reduced upon reaching the substrate. Consequently, the surface diffusivity as well as mobility of the sputtered Mo particles decrease which, in turn, impedes the crystallization of the deposited Mo film. Subsequently, lesser crystallinity is observed for the Mo film deposited at higher working pressure evident through the less intense Mo (110) diffracting peaks [43]. Hence, the Mo thin film deposited at lower sputtering pressure shows increased crystallinity having sharp (110) peak [40-43], larger

crystallite size [40, 49] with less grain boundaries [40] and compact structure [49]. Zoppi et. al. [50] also support these results.

The crystallite size is found to increase with increasing sputtering power up to a certain point and then decrease with further increase in power. The inspection of the grain size is elaborately done in [16]. They selected three sets of working pressure (3, 8 13 mTorr), DC power (200, 300, 400 W) and temperature (room temperature, 100, 200 ^{o}C) inspect the change properties of Mo back contact by choosing different combination pressure, power and temperature. The lowest grain size was found to be 7.07 nm at 13 mTorr- the highest pressure, 200 W DC power and room temperature, and the highest of that was found to be 18.05 nm at 3 mTorr- the lowest pressure, 300 W DC power- the highest power and 300 ^{o}C- the highest temperature. Primarily, with more molecules with higher kinetic energy arriving at the nucleation sites on the substrate surface with increasing power, nucleation rate starts to escalate, but over the critical point, the increasing nucleation density saturates up the nucleation sites, preventing lateral growth of crystallites resulting in reduction in crystallite size. From the data it can be said that the experimented result, somewhat aberrant but ultimately complied with the theory; higher power and lower pressure yielded greater grain size and the deviation may be the somehow related with the temperature.

2.1.2 Surface Morphology

Surface morphology is one of the properties with which the adhesion of the back contact is related as well as the optical and electrical properties of the solar cell [38]. The surface morphology influences the resistivity of Mo thin film and subsequent growth of chalcogenide absorber. The light reflection is also contingent upon surface morphology. With higher working power, the atoms emitted from the target gain higher kinetic energy and deposit on the substrate

filling up the micro-voids, thus forming densely packed microstructure with less porous surface. Expectedly, the grain size also happens to increase with higher working power. Working pressure has opposite effect; target molecules will face more atomic inter-collision barging through more dense gas layers from target to substrate with the working gas atom with increasing working pressure that substantially slow up the kinetic energy of the depositing target atoms [51-53]. As a result, the lesser chance for the depositing target atoms to fill up the voids over the substrate surface and formation of loosely packed microstructure having smaller grains is obvious. Lowering the working pressure, on the other hand, has similar effect as increasing working power- densely packed microstructure with larger grains.

The deposited Mo thin films consist of spindle [49]/ granular-shape [40]/ fish-like [42, 54]/ flake-like [43] shape nanoparticles with changing feature size with increasing sputtering pressure. While some of the works report transformation of the grains to smaller 'star-like' shaped grains with increase of the working pressure [43, 49], the films have been predicted to exhibit semi-sphere shaped surface morphology at a very high sputtering pressure [40]. With decreasing pressure, the increasing kinetic energy of sputtered Mo particles accelerate the grain growth and migration resulting in larger grain size and decreased defects and voids/microvoids and/or vacancies [49]. The distribution of the grains is more uniform at lower working pressures [49] and the compactness/ density of the surface microstructure increases with decreasing working pressure [40, 42, 49]. At higher sputtering pressure, the deposited Mo films exhibit smaller grain size [40, 49] with much more grain boundaries [40]. The grains agglomerate and the distribution uniformity of the grains decrease with increasing pressure [49]. Consequently, the surface structure is more porous at higher sputtering pressure [40] due to lower kinetic energies of Mo particles causing voids and gaps to increase [40, 49].

As reported by Liu et. al. [41], the deposited Mo films show a columnar microstructure along the direction of the crystal growth. As working pressure goes higher, the microstructure of the Mo films exhibit loose, elongated grains with open grain boundaries [41- 42, 54]. It is because with high Ar gas pressure, the concentration of Ar+ ion goes up, too. This increases the number of collisions between the Ar species and the sputtered Mo particles. The mean free path of the scattered Mo particles gets reduced [41] which results in lesser kinetic energy of the particles when those strike upon the substrate. The grain nucleation is thus weakened and so is the growth of the Mo film [49]. With open grain boundaries, the microstructure shows enlarged voids at higher sputtering pressure [41]. Consequently, a rougher surface morphology is observed at the higher working gas pressures compared to that at the lower pressures as evident from the RMS surface roughness [41, 43, 49]. It has been also reported that a fibrous columnar needle-like structure is favorable for CIGS solar cell fabrication as this structure provides more active nucleation sites for the growth and improves the adhesion of the absorber/Mo interface [36, 55].

2.1.3 Surface Roughness

Roughness is the result of micro-voids and porous remaining on the surface after sputtering. As previously discussed in surface morphology, high working pressure builds up ununiform Mo layer with loosen microstructure with lot of pores and micro-voids [31] whereas at lower working pressure, the average roughness was due to large grain size formed under high kinetic energy gained by the atoms [34]. So, surface roughness tend to increase with rising pressure. Working power on the other hand has opposite effect on surface roughness. High working power results in uniform, densely packed Mo layer which is rather smooth.

2.2 Electrical Properties of Sputtered Mo Thin-films

Resistivity of the sputtered Mo is highly co-related with surface morphology and surface roughness. Different crystallographic imperfections of the Mo microstructure, as [43, 56] reports, including point defects, impurities, grain boundaries, dislocation density, micro-strain etc. may cause scattering of conduction electrons which is related to the resistivity of the films. During their propagation, the conduction electrons experience scattering due to their interactions with the neighboring defects of the Mo crystal structure in the vicinity of their traveling path. These scattering processes, according to [57], determine the electrical resistivity of metallic thin film quantitatively.

The films become more conductive when the working pressure is being lowered down [16, 26]. As seen in the XRD results in [26], lower electrical resistivity is ascribed to enhancements in crystallinity and grain size, which weakens grain boundary scattering and increases carrier lifetime. As the kinetic energy of the sputtered Mo particles increase with the decrease of working gas pressure, the grain size increases resulting in less grain boundaries [49]. The grain boundaries are often regarded as the primary source of dislocation density and the dislocation density is proportionate to the average micro-strain [58]. As evident from the equation below [59, 60], changes in dislocation density predominantly cause mean squared microstrain to vary, yielding a linear proportional relationship between the two:

$$\varepsilon^2_{hkl} = 2\pi b^2 M^2 C_{hkl} P_{dislocation}$$

whereby,

ε^2_{hkl} = mean squared microstrain in along (hkl) plane,

b = Burgers vector,

M = Wilkens factor,

C_{hkl} = Contrast factor of dislocation, and

$P_{dislocation}$ = dislocation density along the same (hkl) plane.

Under lower working gas pressure, the deposition condition renders sputtered Mo particles with higher kinetic energy when these arrive onto the SLG substrates as a result of lower frequency of collision of Mo particles with the working gas atoms. Consequently, the reorganization of the arriving Mo particles becomes more likely, and the lattice point mismatches are decreased [43]. As a result, the microstrain induced by the lattice point mismatches also decreases. These lattice point mismatches are basically dislocation cores. Thus, the decrease in Ar gas pressure yields decreased dislocation density and average micro-strain in the deposited Mo films [43, 49].

On the contrary, the growth of the Mo film is weakened owing to lesser re-arrangement of incident Mo atoms onto the substrate during nucleation stage for their lower kinetic energy because of higher background gas pressure. As a result, lattice point mismatches get bigger, and the dislocation density increases. Subsequently, more microstrain is induced [43]. At High working pressure, sputtered Mo is grown with loosen microstructure with many pores and micro-voids [31]. This, in consequence, not only increase surface roughness but also the resistivity since there is now more scopes for impurities such as oxygen to occupy the intermolecular spaces [34]. In addition, as the grain size become smaller with increasing pressure, charge carrier faces grain boundary potential barrier in shorter time interval, which eventually hamper the carrier transportation and henceforth results in higher resistivity.

Fuchs and Sondheimer proposed surface scattering and isotropic electron scattering to explain the connection between the bulk resistivity and film resistivity in their electrical conductivity model [61, 62]. Mayadaz and Shatzks hypothesized a simultaneous mechanism

where they took grain boundary scattering into account in addition to isotropic electron scattering and surface scattering. According to them [63],

$P_f / P_o = 1/G(\alpha)$

whereby P_f = resistivity of thin film,

P_o = resistivity of single crystal and

$G(\alpha) = 1 – (3/2)\alpha + 3\alpha^2 - 3\alpha^3 \ln (1 + 1/\alpha)$

$\alpha = (\lambda/d) (r/ (1 - r))$

in which α = a pre-factor, which depends on

λ = mean free path for electrons,

d = grain size, and

r = grain boundary reflection coefficient for electrons.

The scattering mechanism of conduction electron assumed by Mayadaz and Shatzks is more likely to take place in the deposited Mo films as evident from the columnar grain boundaries and polycrystalline nature of their microstructures [41, 43, 54]. Since the scattering of conduction electrons due to dislocations depends on the local strain fields generated around the dislocations cores [64] and the resistivity increases linearly with increase in the dislocation density [58]- based on the linear proportional relationship between the mean squared microstrain and dislocation density- the increase in the resistivity is linearly related to the mean squared microstrain [65]. So the Mo films with greater dislocation density possess higher microstrain and in turn, higher resistivity [43, 49], which can be attributed to the decrease in electrical conductivity due to various sources of mechanism of conduction electron scattering [43].

Therefore, the decrease in dislocation density and the average micro-strain of the deposited Mo films with decrease in sputtering gas pressure causes the resistivity of the Mo films to decrease [43, 49], thereby directly increasing the carrier lifetime and Hall mobility [49] as well as carrier density [43].

Higher working power however has opposite effect on the resistivity of the film comparing to working pressure, as densely packed micro-structure grown by high power provides meager opportunity for foreign atoms to accommodate within inter molecular space and larger grain size and improved crystallinity can be responsible for improved carrier mobility during electrical, as the need to cross lesser number of grains with reduced grain boundary potential barrier reduce grain boundary scattering and increases carrier lifetime [20, 66, 67].

Most of the paper reported the change of resistivity of sputtered Mo back contact of CIGS solar cell by varying either sputtering power [20, 31] or pressure [26, 36]. [16] made 9 set of control factors by varying three influential sputtering parameters: working pressure (3, 8, and 13 mTorr), DC power (200, 300, and 400 W), and substrate temperature (room temperature, 100, 200 ^{o}C) and inspect the variation of resistivity. An analysis of variance (ANOVA) was performed in their work, in order to evaluate the coating parameters that were statistically significant. It was found that the contribution of the parameters to the change resistivity of Mo back contact is following- pressure 94.77%, power 2.47%, Substrate temperature 1.11% and residual error 1.65%. The best result where the resistivity of the DC sputtered Mo film found to be minimum was when the pressure was minimum among the set of choice- 3 mTorr, power was maximum among the set of choices- 400 W and room temperature was 200 ^{o}C.

2.3 Optical Properties of Sputtered Mo Thin-films

Smoother surface with lesser voids and porosity sputtered in low pressure condition has higher reflectivity, as expected [34]. Badgujar et. al. [20] reported that the reflectance of the sputtered Mo back contact was found to be almost the same for films deposited at various sputter power while it was found to decrease with increasing Ar gas flow rate in their experiment. Huang et. al. [16] reported the reflectance was found to be maximum (58.87%) when the sputter power and substrate temperature was maximum (400 W and 200 ^{o}C) while the pressure was minimum (3 mtorr) in their choice of selection of 9 set of combination of influential sputtering parameters. Also, when the pressure was low (3 mtorr), varying the power (200, 300, and 400 W) and substrate temperature (room temperature, 100, 200 ^{o}C) did not change the reflectance much (from 55.40% at 200 W DC sputtering power and substrate at room temperature to 58.87% at 400 W power and 400 ^{o}C substrate temperature, change is about 3.47%), but when the pressure was high (13 mTorr), power and substrate temperature variation alters the reflectance at a bigger scale (32.47% at 200 W and 200 ^{o}C to 42.97% at 400 W and 100 ^{o}C, change is about 8.50%). Though the contribution of influential sputtering parameters towards reflectance was not charted in their work, after scrutinizing the of the experiment of above-mentioned papers, it can be concluded that:

1. The influence of working pressure on the reflectance is the greatest among all the other parameters of sputtering process which influence that property.

2. If the pressure is increased after a certain range, the contribution of sputtering power to reflectance becomes more noticeable. Since more sputtering power constructs smooth densely structured surface with lesser porous, micro-voids and better uniformity, the sputtered Mo film tends to be more reflective.

2.4 Mechanical Properties of Sputtered Mo Thin-films

2.4.1 Residual Stress

To ensure reliability of the Mo thin films, mechanical properties such as good adhesion to the glass substrate and low residual stress within the film are essential attributes [20]. The excessive compressive or the tensile stress can result in the poor adhesion between the Mo film and the substrate and may results in delamination of the film [16, 31].

Not only the amount of residual stress of Mo back contact depends on the sputtering pressure, the type of residual stress depends on this parameter also. While primarily slight shift of the Mo (110) peak to the higher 2θ/ the right with increase in the working pressure in the range of 0.75 mTorr to 15 mTorr has been reported [41-43] prior to its shifting to the lower 2θ for higher pressure [41-43], other work has depicted a shift to the lower 2θ of the Mo (110) peak for increasing the pressure all way along [40]. According to [68], the position of Mo (110) peak at $2\theta \approx 40.5^{o}$ refers to a Mo film free from stress-strain with an equilibrium lattice parameter of a ≈ 0.314737 nm. As it has been put in [41], the shift in Mo (110) peak position refers to the change in the lattice spacing according to the Bragg's law. With changing sputtering pressure, variation of average lattice spacing in the direction normal to the Mo (110) plane causes changes in the distribution of inter-planar spacings which, in turn, results in changes in strain. A shift of the Mo (110) peak from the equilibrium position referring to the equilibrium lattice parameter of the Mo unit cell to the lower 2θ/ left implies a shortening of the lattice parameter of the unit cell [43]. So, in this case, the Mo film goes under compressive stress with compared to that of the Mo film under equilibrium condition. On the other hand, Mo films exhibiting a dominant (110) peak at a position close to that of $2\theta \approx 40.4^{o}$ comparatively experience some relaxation, indicating a

lengthening of the Mo unit cell lattice parameter. The Mo films deposited at lower pressures are more compressive stressed compared to those deposited at higher working pressures [41-43].

2.4.2 Adhesion

Single Mo layer has higher chance to have excessive tensile or compressive residual stress which may lead to surface cracking and delamination between the Mo film and the substrate [34, 69]. High compressive stress causes buckle lines on the films and leads to very poor adhesion properties compared with tensile stressed films [16, 70, 71]. Some paper reported a certain pressure limit, lowering under which may result in surface cracking. In [36], films deposited at 0.5 mTorr and 0.75 mTorr initially adhered well but within few minutes of removal from the vacuum chamber a buckling process started from the corners of the sample and spread across the wafer; eventually showed severe delamination. These stress relief patterns were observed in both ion beam and DC magnetron sputtered films. The observed effect was called "wrinkled spots" and "wavy ridges" in [72]. These kinds of micrometer-scale patterns were also reported by Wu et. al. using an optical microscope [71]. Although three fourths of the films deposited at 1 mTorr survived the adhesion test, films peeled from the sample edges. Single layer Mo back contact which is deposited at 2.5 mTorr failed the adhesion test but films deposited up and over 5 mTorr adhered well with the SLG substrate in [26]. Reported in [31], none of the Mo back contact deposited on 30 cm × 30 cm under 5 mTorr pressure, 30 sccm Ar gas flow rate and with 1-3 kW power survived adhesion test, only when the pressure is 7 mTorr and over the samples showed satisfying adhesion. All the samples sputtered at 3 mtorr didn't adhere to the SLG substrate, but samples sputtered at 8 mTorr and 13 mTorr working pressure passed the adhesion test.

CHAPTER III

EFFECT OF PROCESS PARAMETERS ON THE PROPERTIES OF Mo THIN-FILMS

3.1 Material and Sputtering

The Mo target was acquired from Himet Materials and had a diameter of 2 inch. and a thickness of ¼ inch. The target had a purity of 99.98%. All the Mo thin-films were deposited on soda-lime glass (SLG) substrates. Before the deposition, all the soda-lime glass substrates were subjected to the following cleaning sequence: first, the substrates were rinsed with deionized water; then the substrates were cleaned by acetone and ethanol in sequence; next, the substrates were rinsed again with deionized water followed by blow-drying with air.

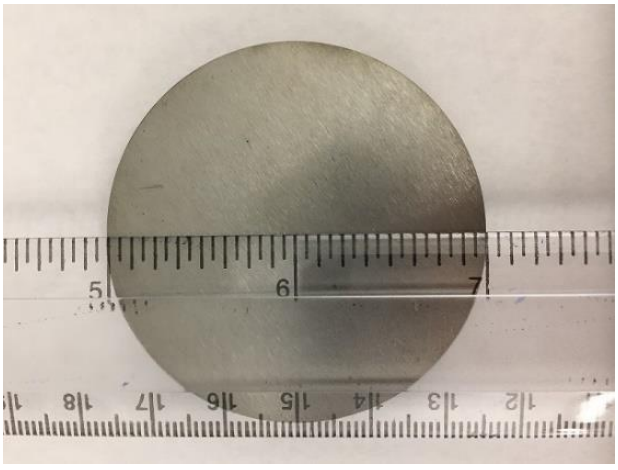

Figure 3.1: Molybdenum target having a diameter of 2 inch.

The magnetron sputtering system employed here to deposit Mo thin-film was of confocal configuration. Both DC and RF sputtering power were used for sputtering purpose. In the RF sputter mode, the power was delivered at 13.56 MHz. Prior to deposition from the target, the sputtering chamber was vacuumed to a pressure of about 10^{-6} torr. To ensure the surface of the molybdenum target does not contain any contaminants, pre-sputtering of the target was performed before the deposition of the samples. All the samples were sputtered at room temperature and the substrate rotation was kept fixed at 40 rpm. Ar gas flow rate was kept constant at 15 sccm.

To inspect the effect of working gas pressure and sputtering power on the properties of Mo thin-film, pressure was varied from 2 to 30 mTorr and power from 100 to 250 W. Five representative pressures were selected for this purpose: 2 mTorr, 3 mTorr, 5 mTorr, 20 mTorr, and 30 mTorr. The sputtering power was varied keeping the pressure constant at each of the five pressures. The power supplied were: 100 W, 150 W, 200 W, and 250 W. Both DC and RF power were used to observe and differentiate between the effect of sputtering modes as well. Sputtering time for different samples were varied to ensure enough deposition in each case. Naturally, the film thickness was also varied from sample to sample. The Table 3.1 below displays the working pressure and sputtering power combinations for different samples for both DC- and RF-sputtered Mo thin-films.

Table 3.1: Pressure and power combinations for depositions of the samples.

	Sample #1	Sample #2	Sample #3	Sample #4	Sample #5
Pressure (mTorr)	2	3	5	20	30
Power (W)	100	100	100	100	100
	Sample #5	**Sample #6**	**Sample #7**	**Sample #8**	**Sample #9**
Pressure (mTorr)	2	3	5	20	30
Power (W)	150	150	150	150	150
	Sample #11	**Sample #12**	**Sample #13**	**Sample #14**	**Sample #15**
Pressure (mTorr)	2	3	5	20	30
Power (W)	200	200	200	200	200
	Sample #16	**Sample #17**	**Sample #18**	**Sample #19**	**Sample #20**
Pressure (mTorr)	2	3	5	20	30
Power (W)	250	250	250	250	250

3.2 Characterization

Crystallography of the deposited Mo samples was done by obtaining X-ray diffraction patterns of the deposited thin-films. A Rigaku Miniflex Cu-Kα diffractometer was employed for this purpose. The diffraction was carried out at room temperature. The wavelength of Cu-Kα radiation was 1.5406 angstrom. The 2θ record range of the diffraction patterns was from 20° to 90°. The scanning was done using a step size of 0.1°.

From the diffraction patterns, the preferred growth orientation of the crystal normal to the surface of the thin-film sample were identified. The preferred crystal orientations were recognized from the corresponding diffraction peak intensities along with the full width at half maximum (FWHM) of the peaks.

We employed Scherrer's formula to obtain the grain size of the deposited thin-film:

$$D = \frac{0.9\,\lambda}{\beta \cos\theta}$$

where

D is the grain size in nm,

λ is the wavelength of the X-ray equal to 0.15406 nm,

β is the full width at half maximum of the corresponding diffraction peak in radians (2θ),

θ is the Bragg X-ray diffraction angle in radians.

The dislocation density of the crystal structure was calculated using the following formula:

$$\delta = \frac{n}{D^2}$$

where

δ is the dislocation density in nm^{-2},

D is the grain size in nm,

n is a factor which becomes unity when dislocation density becomes minimum.

The microstrain induced in the crystal structure was calculated from the following:

$$\varepsilon = \frac{\beta}{4\tan\theta}$$

where

ε is the strain (dimensionless).

The sheet resistance of the deposited Mo thin-films were measured using a four-point sheet resistance meter (R-CHEK 2175).

3.3 Effect of Sputtering Parameters on Properties of DC Sputtered Mo Thin Film

3.3.1 Effect of Pressure and Power on Crystallinity and Structure of DC Sputtered Mo Single Layer

All the Mo thin-films grown with DC sputtering power showed XRD patterns similar to the spectrum documented in ICDD reference 004-0809 or JCPDS Card No. 3-065-7442. This confirms that the deposited Mo thin-films possessed a body-centered cubic (BCC) crystal structure with a preferred growth orientation of the crystal along (110) plane. The preferred crystal orientation was obvious from the intense (110) peak observed in the XRD patterns obtained for all thin-film samples. As the (110) plane in the Mo BCC crystal structure possesses lowest surface energy per unit area, the atoms sputtered from the target tended to occupy the plane requiring lowest amount of energy and thus exhibited a preferential growth along the (110) plane.

In general, the films deposited under lower working pressure at all sputtering powers showed the most intense (110) peaks and the lowest full width at half maximum (FWHM) at the (110) orientation indicating a highly crystalline growth along the (110) plane. The intensity of the (110) peak decreased and the FWHM of the peak increased with increase in working pressure as can be observed from Figure 3.2 (a-d) and Figure 3.3. These figures depict the XRD patterns and variation of FWHM of (110) peak of the samples deposited under varying pressures at different sputtering powers. The sputtered Mo atoms experience more collisions with the process gas Ar ions under increasing pressure which makes the Mo atoms lose their kinetic energy more when they reach the substrate. The atom mobility and, in turn, their diffusivity through the film gets hampered which ultimately results in reduced crystallinity. An exception can be seen in the trend for sample 14 (20 mTorr, 200 W) and sample 18 (5 mTorr, 250 W). These two Mo samples showed an increase in (110) peak intensity compared to their forerunners deposited under 5 mTorr, 200 W (Sample 13) and 3 mTorr, 250 W (sample 17), respectively. The FWHM of the (110) peak for the sample 18 decreased instead of increasing when the pressure was increased from 3 mTorr (sample 17) to 5 mTorr (sample 18), as well. This increase in crystallinity at higher working pressure might be attributed to the increase of film thickness [31], which would have been very likely to take place due to higher deposition time of the corresponding samples.

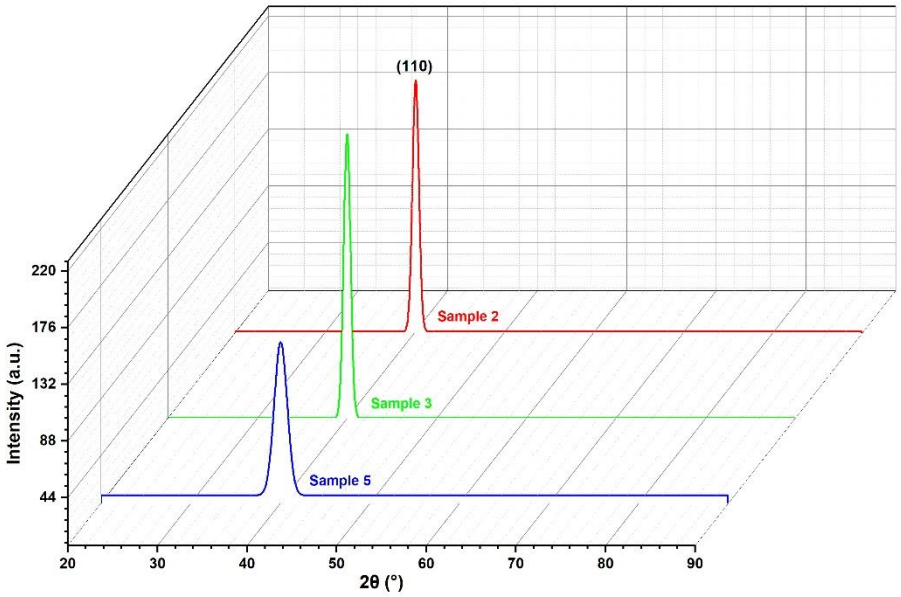

Figure 3.2(a): Sample 2 was deposited under 3 mTorr, Sample 3 under 5 mTorr, and sample 5 under 30 mTorr. Power was kept constant at 100 W.

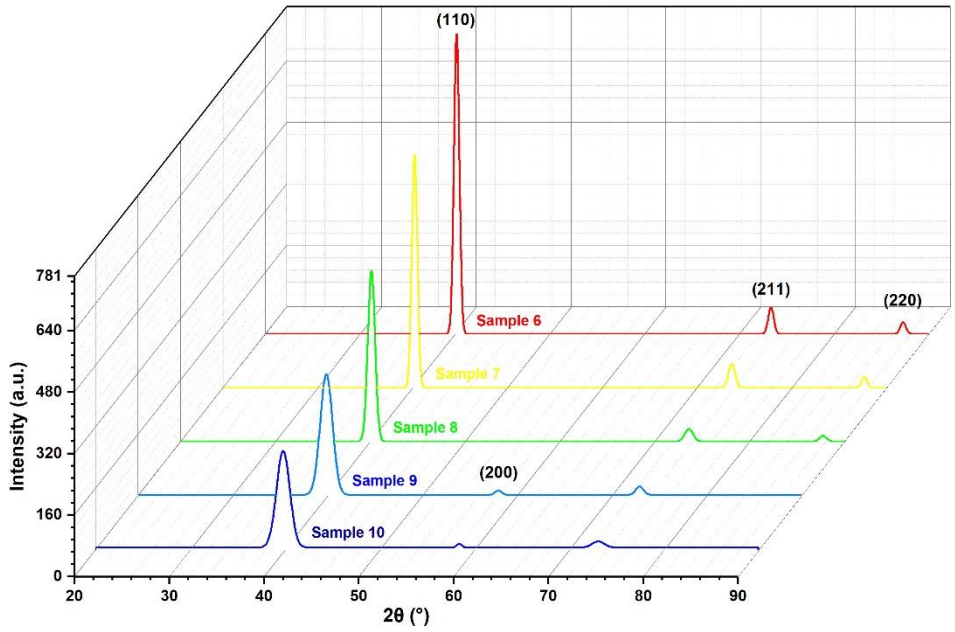

Figure 3.2(b): Sample 6 to sample 10 were prepared under working pressure of 2, 3, 5, 20, and 30 mTorr, respectively. Power was kept constant at 150 W.

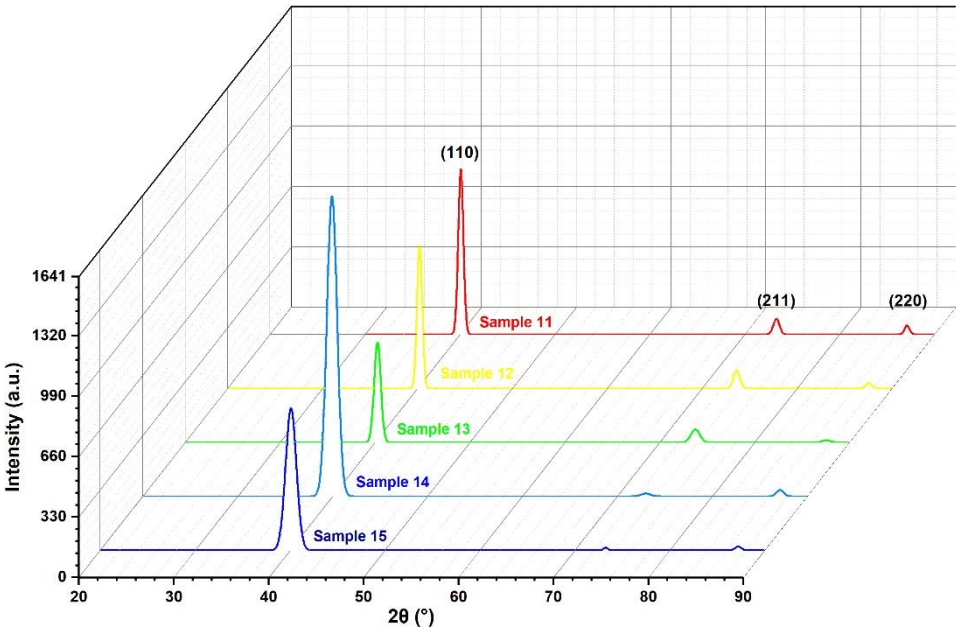

Figure 3.2(c): Sample 11 to sample 15 were prepared under working pressure of 2, 3, 5, 20, and 30 mTorr, respectively. Power was kept constant at 200 W.

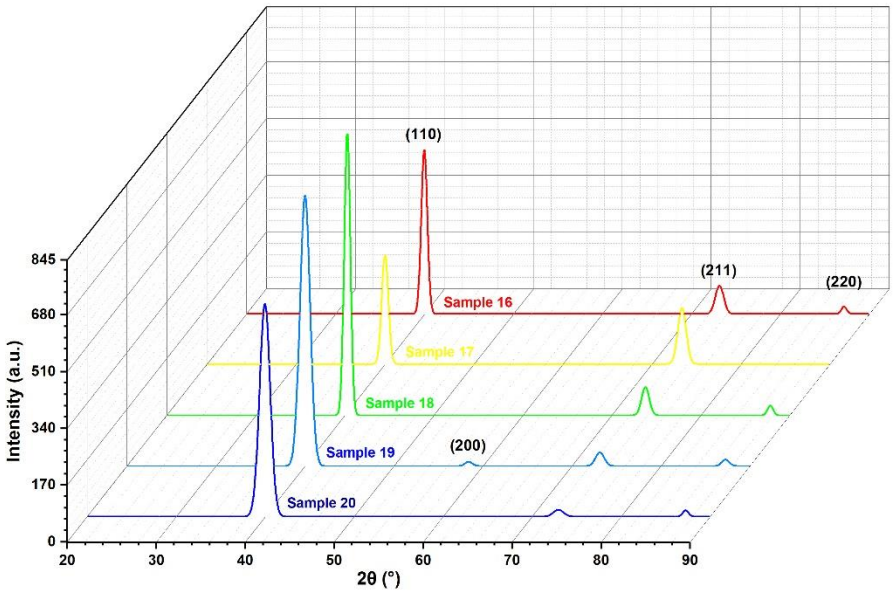

Figure 3.2(d): Sample 16 to sample 20 were prepared under working pressure of 2, 3, 5, 20, and 30 mTorr, respectively. Power was kept constant at 250 W.

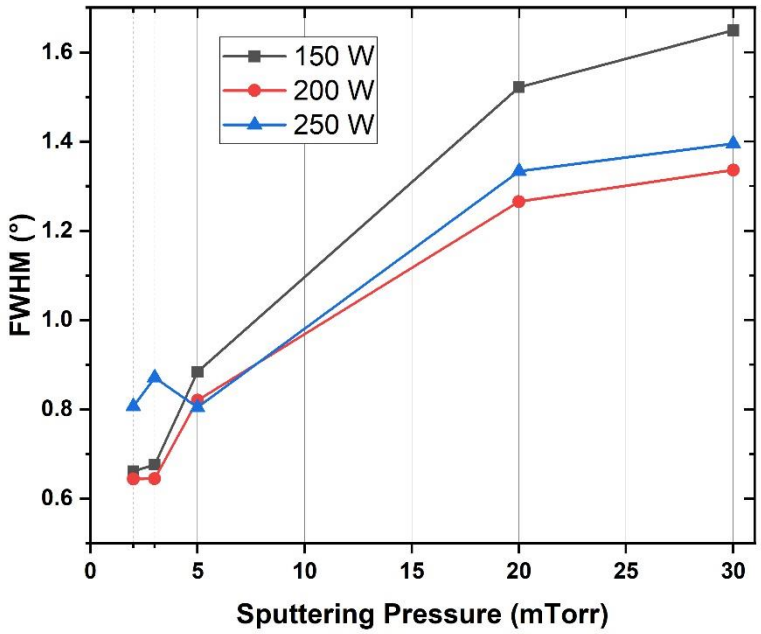

Figure 3.3: Variation of FWHM with variation of working pressures at different sputtering powers.

Similar to the working pressure, sputtering power also had a pronounced effect on the crystallinity of the deposited Mo thin-films. The (110) peak intensity of the samples increased and its FWHM decreased with increase of power from 100 W to 200 W as can be observed from Figure 3.4 (a-e) and Figure 3.5. Apparently, the increase of the sputtering power had the same effect as the decrease of the working pressure had on the crystallinity. When the working gas pressure remains the same, the Ar gas ions bombard the sputtering target with higher kinetic energy at the increased sputtering power. These ions impart more energy to the released target atoms. With the fixed process gas pressure, the Mo atoms with higher kinetic energy experience less scattering events with the process gas ions and higher mean free flight path toward the substrate. The sputtered Mo atoms thus arrive on the substrate with higher kinetic energy resulting in better atom mobility and diffusivity through the film. Consequently, the crystallinity of the films got better with increase in sputtering power unless reached a certain point. With

further increase of power to 250 W, both the intensity and FWHM of (110) peak decreased compared to those observed mostly at 200 W, and sometimes the one at 150 W, too. This is because that the increase of sputtering power beyond 200 W probably triggered re-sputtering [47] of the already-deposited Mo atoms on the substrate. The highly energetic Mo species can impact on the substrate ballistically and cause re-emission of the Mo atoms already deposited. As a result, the thin-film sputtered at 250 W showed decreased crystallinity through a less intense and sharp peak along (110) plane.

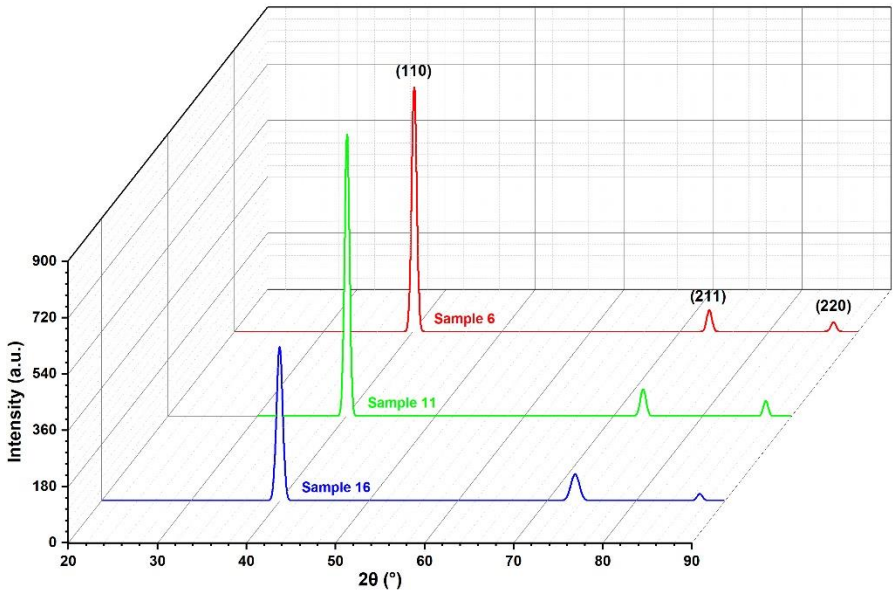

Figure 3.4(a): Sample 6 to sample 16 were prepared under 150, 200 and 250 W, respectively. Pressure was kept constant at 2 mTorr.

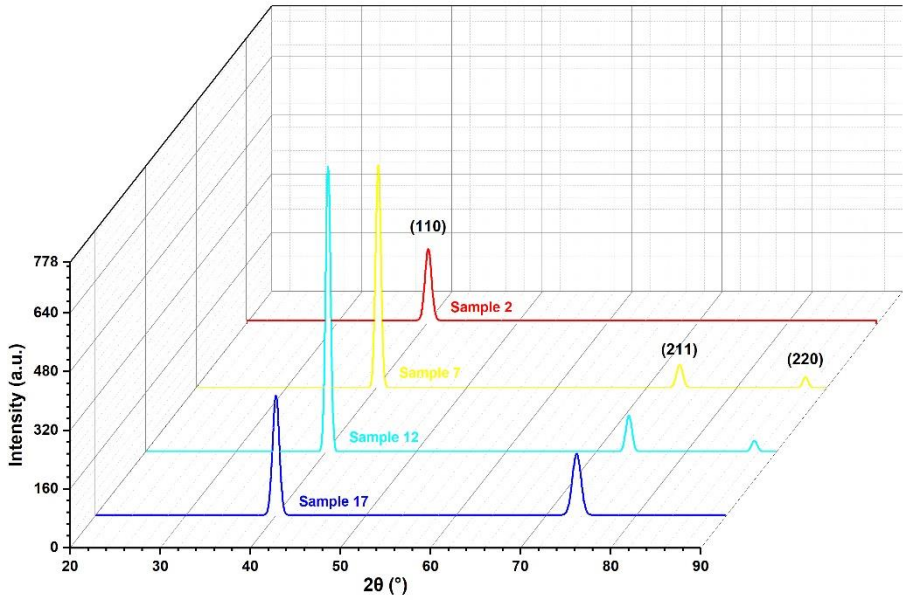

Figure 3.4(b): Sample 2 to sample 17 were prepared under 100, 150, 200 and 250 W, respectively. Pressure was kept constant at 3 mTorr.

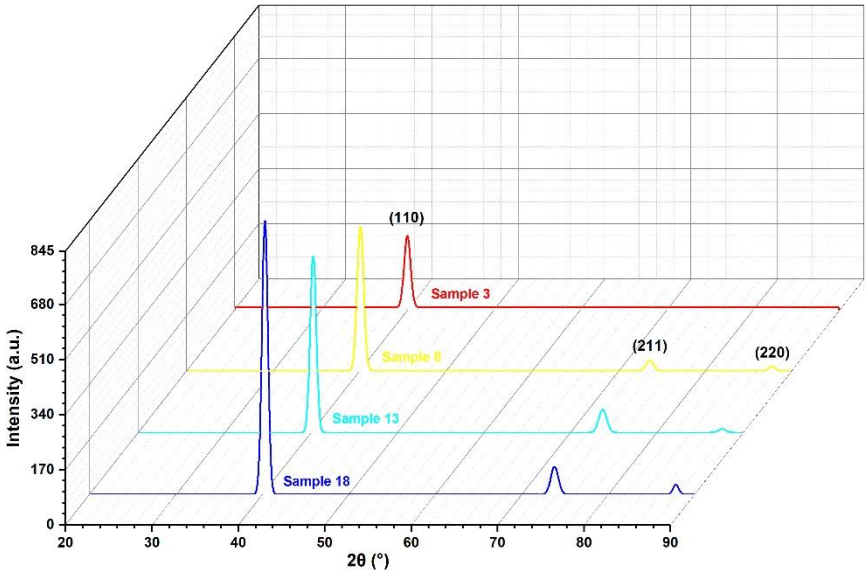

Figure 3.4(c): Sample 3 to sample 18 were prepared under 100, 150, 200 and 250 W, respectively. Pressure was kept constant at 5 mTorr.

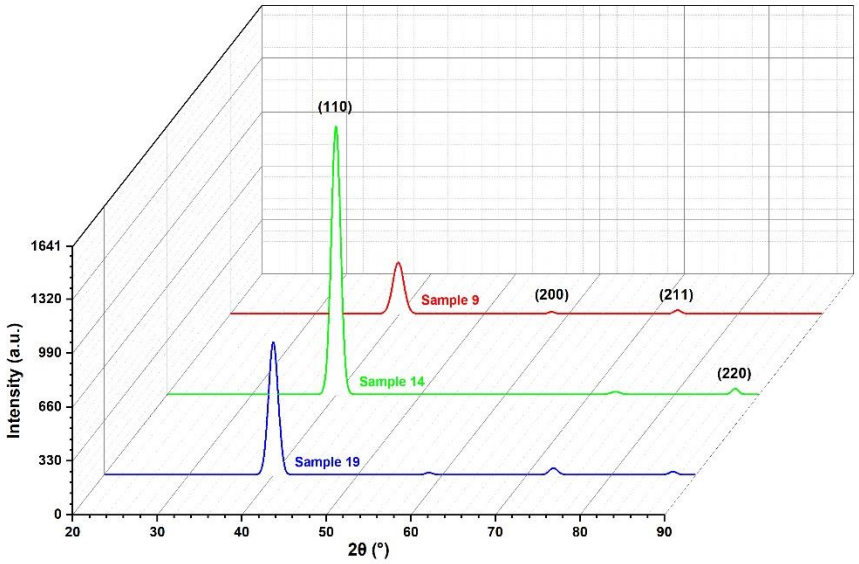

Figure 3.4(d): Sample 9 to sample 19 were prepared under 150, 200 and 250 W, respectively. Pressure was kept constant at 20 mTorr.

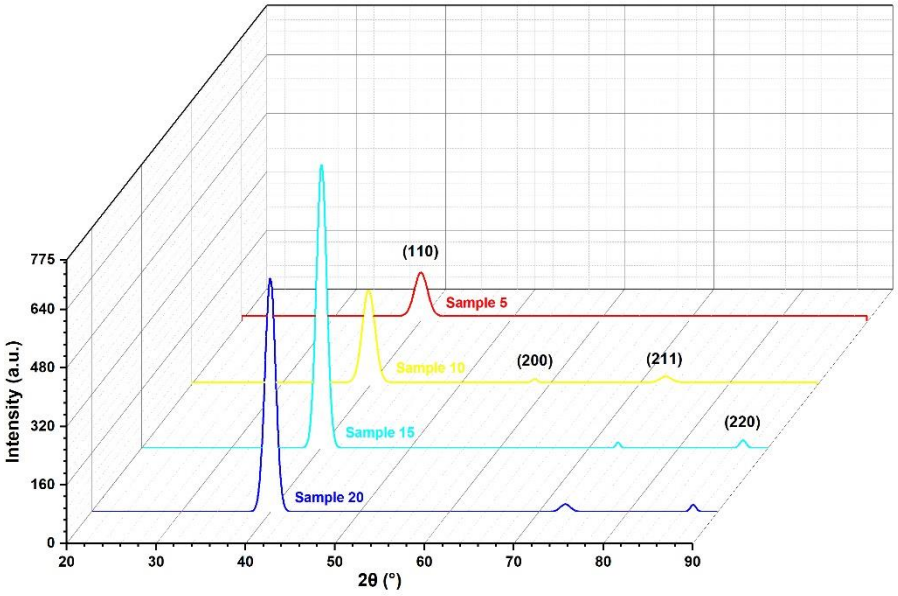

Figure 3.4(e): Sample 5 to sample 20 were prepared under 100, 150, 200 and 250 W, respectively. Pressure was kept constant at 30 mTorr.

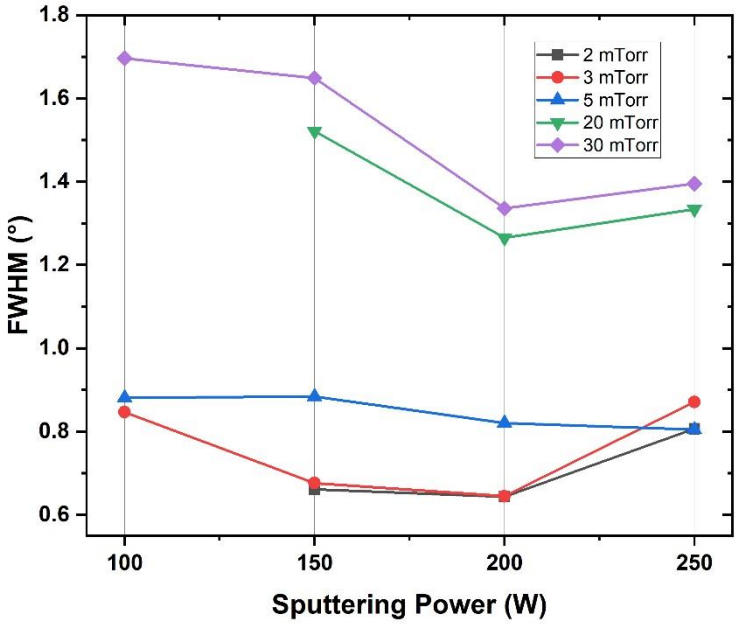

Figure 3.5: Variation of FWHM with variation of sputtering power at different working pressures.

From the discussion of the effect of working pressure and sputtering power on crystallinity of the Mo thin-film, it is obvious that the low process gas pressure and higher working power helped increase the crystallinity of the deposited samples. Though sample 14 displayed the most intense diffraction due to (110) growth orientation among the samples, the FWHM of the peak was 1.265- exceeding those of the samples deposited under lower working pressure by a big margin. The lowest FWHM (0.644) of the (110) peak was observed for sample 11 (deposited under 2 mTorr, 200 W) which also possessed the second most intense (110) peak among all the samples. Both the (110) peak FWHM (0.645) and its intensity of sample 12 (sputtered under 3 mTorr, 200 W) were very close to those of sample 11.

3.3.2 Effect of Working Pressure on Grain Size, Dislocation Density and Strain of DC Sputtered Mo Samples

The Table 3.2 below shows the variation of grain size, dislocation density, and strain at fixed sputtering powers with the change of sputtering pressure. At all sputtering powers, grain size of the samples decreases with increase of working pressure. At lower sputtering pressure, the sputtered Mo atoms face less collision events with process gas ions and hence become less scattered. Upon arrival on the substrate, the sputtered target atoms thus possess greater kinetic energy which is then converted into thermal energy. The higher the thermal energy produced at lower process gas pressure, the higher the grain nucleation and migration become. In turn, the grain size tends to increase at lower working gas pressure. For powers of 100 W, 150 W, and 200 W, the highest grain size was obtained when the samples were deposited at the lowest sputtering pressure, 2 mTorr. The only exception occurred when the sample sputtered at 5 mTorr possessed the maximum grain size among those deposited at 250 W. However, this sample (sample 18) and the sample 16 (deposited under 2 mTorr and 250 W) had almost similar grain size- 10.52 nm and 10.48 nm, respectively. Except sample 18, all other samples followed the same trend for the change of grain size with variation in sputtering pressure. The samples prepared at the highest sputtering pressure of 30 mTorr at all sputtering power had the lowest grain size. The Figure 3.6 below shows the change of the Grain size of the Mo samples sputtered at different DC powers with variation in working pressure.

Table 3.2: Variation of grain size, dislocation density and strain with change in working pressures at different powers.

Sample No.	Sputtering Pressure	Sputtering Power	Grain Size (nm)	Dislocation Density ($\times 10^{-3}$) (nm^{-2})	Strain ($\times 10^{-3}$)
2	3	100	9.9893632	10.0213076	10.105613
3	5	100	9.5938357	10.864643	10.570794
5	30	100	4.9836607	40.262716	20.323719
6	2	150	12.794974	6.10831168	7.8885652
7	3	150	12.507585	6.39224013	8.0627129
8	5	150	9.5663497	10.9271648	10.560768
9	20	150	5.5533683	32.4255276	18.313213
10	30	150	5.122949	38.10307	19.890966
11	2	200	13.134971	5.79617842	7.6984694
12	3	200	13.124497	5.80543358	7.6790597
13	5	200	10.31678	9.395325	9.762407
14	20	200	6.6808624	22.4044837	15.190573
15	30	200	6.3297228	24.9591973	15.972443
16	2	250	10.480273	9.10447317	9.6742262
17	3	250	9.7057274	10.6155824	10.431022
18	5	250	10.516795	9.04134753	9.5742486
19	20	250	6.3384958	24.8901544	15.990062
20	30	250	6.0575133	27.2528078	16.744276

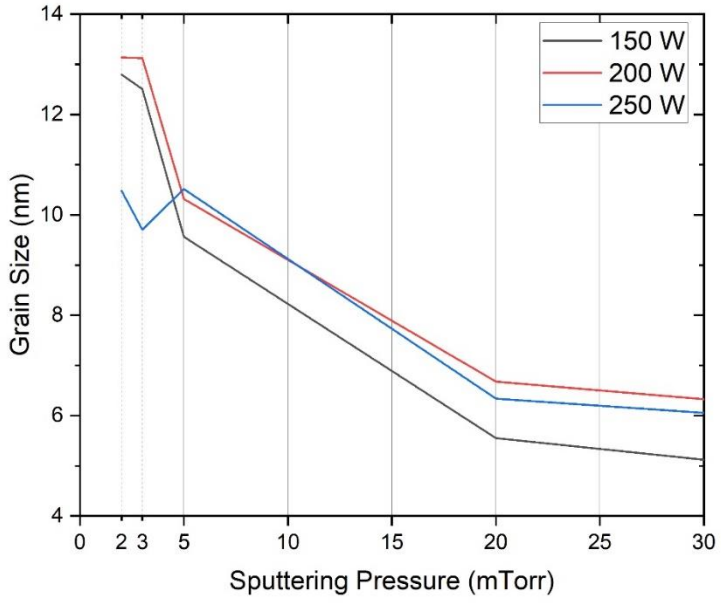

Figure 3.6: Variation of grain size with variation of sputtering pressure at different working powers.

Dislocation densities and strain were the lowest for the samples deposited at the working pressure of 2 mTorr, as could be expected from the data of grain size. As the target atoms sputtered at lower working pressure hit the substrate surface with higher kinetic energy, the higher thermal energy produced causes to accelerate grain growth and migration. The Mo atoms arriving on the substrate surface thus tend to reorganize more and ensue in less lattice point mismatches which effectively act as dislocation cores. As a result, both dislocation density and lattice point mismatch induced strain get reduced at lower sputtering pressure. The linear proportional relationship between dislocation density and microstrain- as we have already outlined in the literature review- becomes more obvious from our experimental observation. With increase of pressure, both dislocation densities and strain increased at all sputtering powers. As observed for the grain size, the only exception to the variation trend of dislocation density and strain took place for the sample 18. Despite pressure higher than 2 mTorr and 3 mTorr, this sample had a larger grain size, so lower dislocation density and strain as well. Both dislocation density (9.04×10^{-3} nm^{-2}) and strain (9.57×10^{-3}) of sample 18 were very close to those of sample 16 (9.01×10^{-3} nm^{-2} and 9.67×10^{-3}). The Figure 3.7 and Figure 3.8 show the variation of dislocation density and strain, respectively, of the samples deposited at different working powers with change in sputtering pressure.

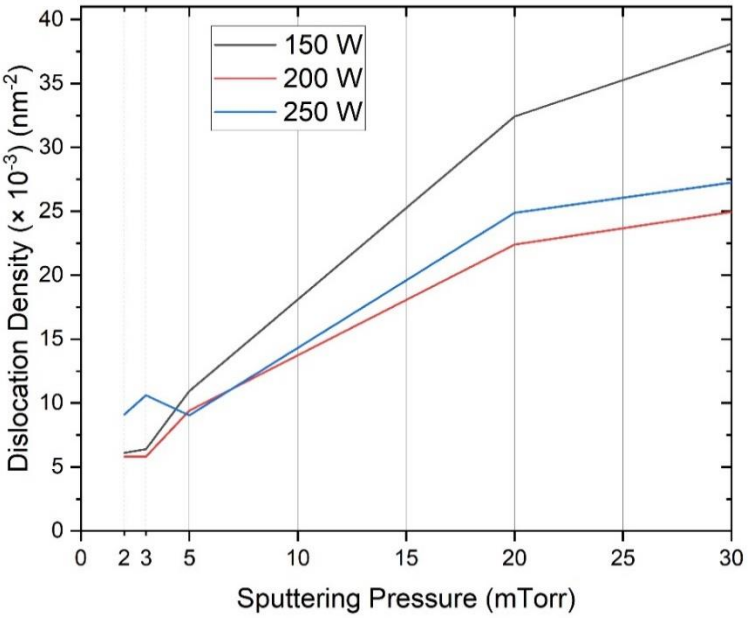

Figure 3.7: Variation of dislocation density with variation of sputtering pressure at different working powers.

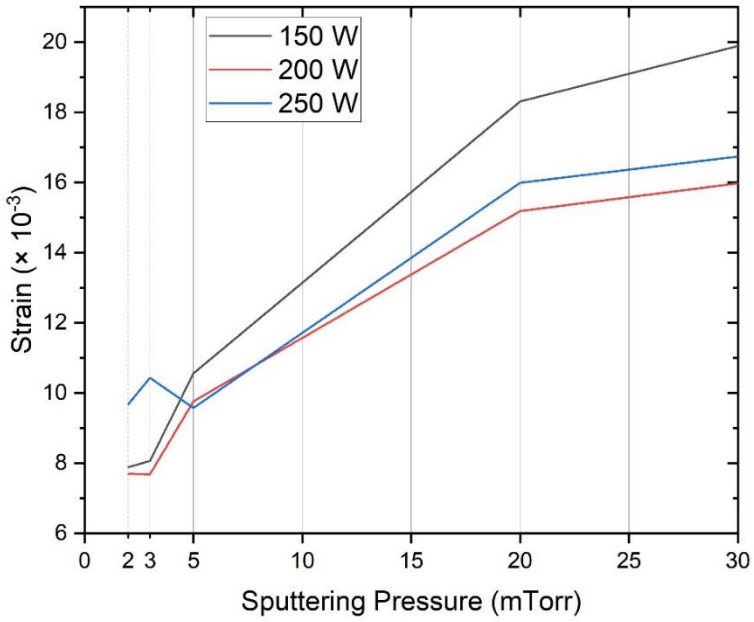

Figure 3.8: Variation of strain with variation of sputtering pressure at different working powers.

In Table 3.3 below, we have tabulated the grain sizes, dislocation densities and strain at the pressures of 2 mTorr and 3 mTorr at different deposition powers. The same has been done in the Table 3.4 for the working pressures 20 mTorr and 30 mTorr. If carefully inspected, an interesting behavior can easily be detected from both tables. That is, both at very low pressures (2 mTorr and 3 mTorr) and high pressures (20 mTorr and 30 mTorr) at all sputtering power, the change of pressure such as from 2 mTorr to 3 mTorr and from 20 mTorr to 30 mTorr does not have a much distinct effect on grain size, dislocation density, and strain. Of course, the differences are discernible but not much as is the usual case when the pressure changes, for instance, from 3 mTorr to 5 mTorr and from 5 mTorr to 20 mTorr. When the pressure changed from 3 mTorr to 5 mTorr at, say, 150 W, it can be seen from Table 3.2 that grain size fell sharply from 12.51 nm to 9.57 nm, and dislocation density as well as strain went up fast- from 6.39×10^{-3} nm^{-2} to 10.93×10^{-3} nm^{-2} and from 8.06×10^{-3} to 10.56×10^{-3}, respectively. Likewise, when the pressure again rose from 5 mTorr to 20 mTorr at, say, 250 W, we can see the same trend- huge difference between grain sizes (10.52 nm and 6.34 nm, respectively), between dislocation densities (9.04×10^{-3} nm^{-2} and 24.89×10^{-3} nm^{-2}, respectively), and between strain (9.57×10^{-3} and 15.99×10^{-3}, respectively).

Table 3.3: Variation of grain size, dislocation density and strain at 2 mTorr and 3 mTorr at different powers.

Sample No.	**Sputtering Pressure**	**Sputtering Power**	**Grain Size (nm)**	**Dislocation Density ($\times 10^{-3}$) (nm^{-2})**	**Strain ($\times 10^{-3}$)**
6	2	150	12.794974	6.10831168	7.8885652
7	3	150	12.507585	6.39224013	8.0627129
11	2	200	13.134971	5.79617842	7.6984694
12	3	200	13.124497	5.80543358	7.6790597
16	2	250	10.480273	9.10447317	9.6742262
17	3	250	9.7057274	10.6155824	10.431022

Table 3.4: Variation of grain size, dislocation density and strain at 20 mTorr and 30 mTorr at different powers.

Sample No.	Sputtering Pressure	Sputtering Power	Grain Size (nm)	Dislocation Density ($\times 10^{-3}$) (nm^{-2})	Strain ($\times 10^{-3}$)
9	20	150	5.5533683	32.4255276	18.313213
10	30	150	5.122949	38.10307	19.890966
14	20	200	6.6808624	22.4044837	15.190573
15	30	200	6.3297228	24.9591973	15.972443
19	20	250	6.3384958	24.8901544	15.990062
20	30	250	6.0575133	27.2528078	16.744276

If we consider sample 11 and sample 12 which were deposited under 2 mTorr and 3 mTorr, respectively, and a power of 200 W, we see from Table 3.3 above that both have almost identical grain size (13.13 nm and 13.12 nm, respectively), dislocation density (5.796×10^{-3} nm^{-2} and 5.805×10^{-3} nm^{-2}, respectively), and strain (7.698×10^{-3} and 7.679×10^{-3}, respectively). Same behavior can be observed from sample 14 and sample 15 where the pressure was changed from 20 mTorr (sample 14) to 30 mTorr (sample 15) with power fixed at 200 W (Table 3.4). Again, the grain sizes (6.68 nm and 6.33 nm, respectively), dislocation densities (22.404×10^{-3} nm^{-2} and 24.959×10^{-3} nm^{-2}, respectively), and strain (15.19×10^{-3} and 15.97×10^{-3}, respectively) were very close. Figure 3.9, Figure 3.10, and Figure 3.11 depict the changes of the Mo thin-film characteristics as described above at pressures 2 mTorr, 3 mTorr, 20 mTorr, and 30 mTorr.

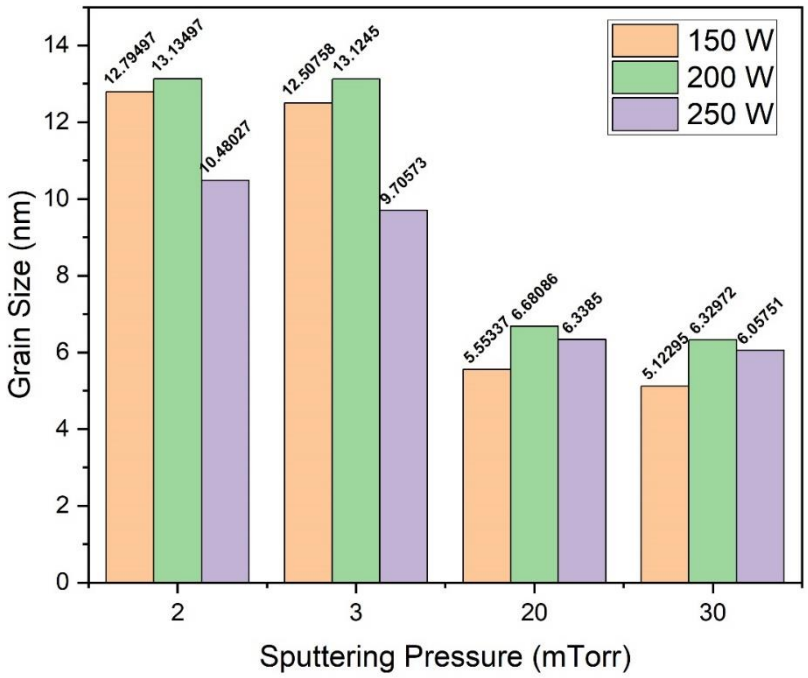

Figure 3.9: Variation of grain size at 2, 3, 20, and 30 mTorr at different powers.

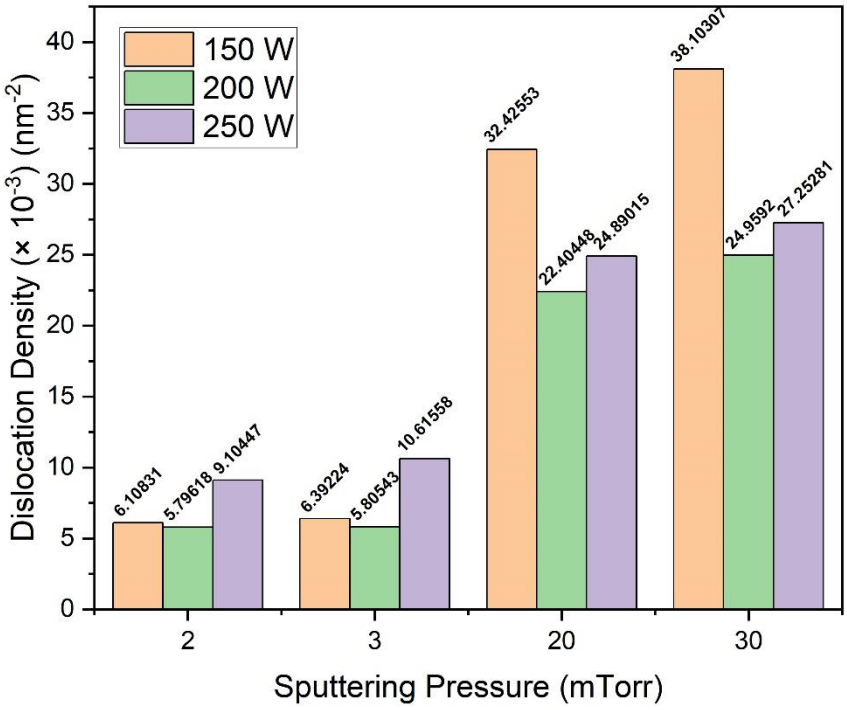

Figure 3.10: Variation of dislocation density at 2, 3, 20, and 30 mTorr at different powers.

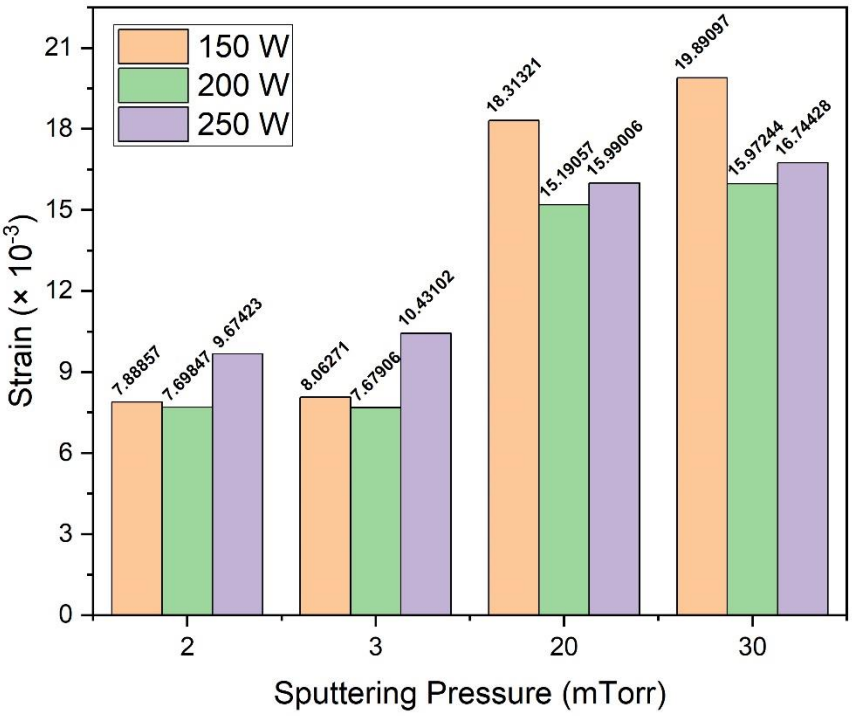

Figure 3.11: Variation of strain at 2, 3, 20, and 30 mTorr at different powers.

3.3.3 Effect of Sputtering Power on Grain Size, Dislocation Density and Strain of DC Sputtered Mo Samples

The grain size of the samples increases with increase in sputtering power up to 200 W. In Table 3.5 below, five different batches of samples can be seen where the samples have been grouped according to their pressure and varying power.

Table 3.5: Variation of grain size, dislocation density and strain with change in sputtering power at different working pressures.

Sample No.	Sputtering Pressure	Sputtering Power	Grain Size (nm)	Dislocation Density ($\times 10^{-3}$) (nm^{-2})	Strain ($\times 10^{-3}$)
6	2	150	12.7949739	6.10831168	7.88856524
11	2	200	13.1349713	5.79617842	7.69846941
16	2	250	10.4802729	9.10447317	9.67422616
2	3	100	9.98936319	10.0213076	10.1056126
7	3	150	12.5075849	6.39224013	8.06271286
12	3	200	13.1244971	5.80543358	7.67905973
17	3	250	9.7057274	10.6155824	10.4310217
3	5	100	9.59383568	10.864643	10.5707941
8	5	150	9.5663497	10.9271648	10.5607678
13	5	200	10.31678	9.395325	9.762407
18	5	250	10.5167952	9.04134753	9.57424864
9	20	150	5.55336827	32.4255276	18.3132126
14	20	200	6.68086244	22.4044837	15.1905729
19	20	250	6.33849577	24.8901544	15.9900618
5	30	100	4.98366069	40.262716	20.323719
10	30	150	5.122949	38.10307	19.8909662
15	30	200	6.32972282	24.9591973	15.9724432
20	30	250	6.05751326	27.2528078	16.744276

When the sputtering power is increased from 100 W to 200 W, the grain size increases. With further increase of power i.e. at 250 W, the grain size decreased. Initially with increasing power, higher number of sputtered Mo atoms with higher kinetic energy arriving at the nucleation sites on the substrate surface intensify the grain nucleation and growth of the thin-film, yielding larger grain up to a certain power- in this case, 200 W. At higher sputtering power of 250 W, the nucleation sites become saturated with increasing nucleation density effectively putting an end to further lateral growth of the grains. Some exceptions- although very little- can be observed for the samples deposited under 5 mTorr. The grain size remains almost the same when the working power is increased from 100 W to 150 W- 9.59 nm and 9.57 nm, respectively.

Another exception was for sample 18- deposited under 5 mTorr and 250 W. The grain size increased for sample 18 compared to sample 13, which was deposited under 5 mTorr working pressure and 200 W. The increment in the grain size of sample 18 was very small though- 10.52 nm compared to 10.32 nm of sample 13. Figure 3.12 below shows the effect of varying sputtering power on the grain size of the samples deposited under different working pressure.

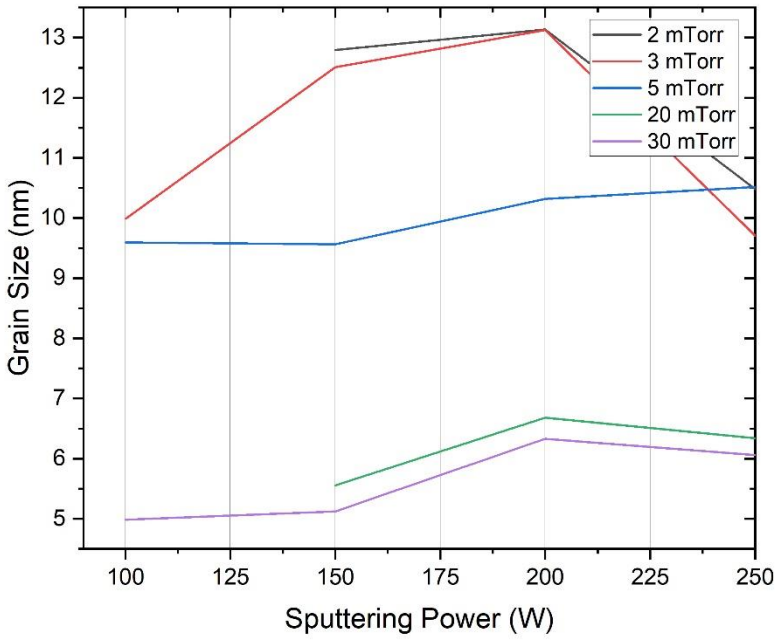

Figure 3.12: Variation of grain size with variation of sputtering power at different working pressures.

As the grain size increases with increase in power from 100 W to 200 W, both dislocation density and strain decrease up to 200 W keeping in line with the theory. The lower sputtering power develops the same effect as the higher working gas pressure on the dislocation density and microstrain. The lower kinetic energy- due to lower sputtering power- of the Mo atoms incident onto substrate surface deters reorganization of the sputtered particles at the time of nucleation, causing bigger and more lattice mismatches to take place and subsequently, increasing

dislocation density. Hence, more strain is produced at lower sputtering power. At 100 W, the samples showed the highest dislocation density and strain, and at 200 W, the lowest dislocation density and strain. As already discussed above, sample 8 and sample 18 demonstrated exception to this trend, as these did in case of the grain size, too. Sample 8 showed increased dislocation density from sample 3- both of which are deposited under 5 mTorr, and 150 W and 100 W, respectively. Despite the little increment, dislocation density (10.93×10^{-3} nm^{-2} and 10.86×10^{-3} nm^{-2}) for either samples are very close. On the other hand, both dislocation density and strain continued to decrease from sample 13 to sample 18. As the sample 18 had a very-close-yet-larger grain size compared to sample 13, it had a lower dislocation density and strain. Yet, these remain very close to those of sample 13. Figure 3.13 and Figure 3.14 show the change of dislocation density and strain of the samples deposited under various working pressure with change in sputtering power.

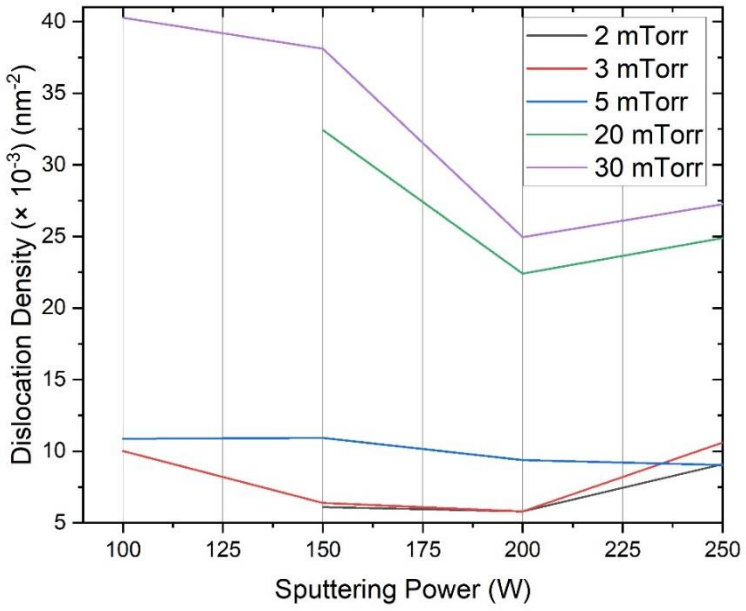

Figure 3.13: Variation of dislocation density with variation of sputtering power at different working pressures.

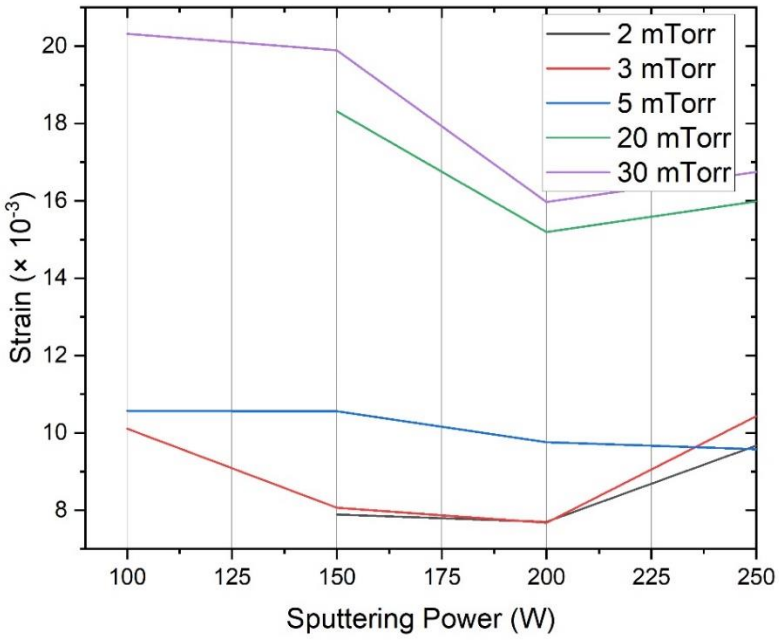

Figure 3.14: Variation of strain with variation of sputtering power at different working pressures.

We can say from the discussion above that the effect of working pressure and sputtering power on grain size, dislocation density and strain of DC-sputtered Mo thin-film well conforms to the theory. Lower working process gas pressure and higher sputtering power were key to larger grain and less dislocation density as well as microstrain. The maximum grain size (13.13 nm) with minimum dislocation density (5.796×10^{-3} nm^{-2}) and strain (7.698×10^{-3}) were obtained from the sample 11 deposited under 2 mTorr and 200 W. In terms of all these film characteristics, sample 12 was very close to sample 11 having a grain size of 13.12 nm, dislocation density of 5.805×10^{-3} nm^{-2}, and strain of 7.679×10^{-3}.

Higher working pressure yielded Mo films with smaller grain size and greater dislocation density as well as strain. Sample 5 deposited under 30 mTorr pressure and 100 W power produced Mo film having smallest grain size (4.98 nm) and maximum dislocation density (40.26×10^{-3} nm^{-2}) and strain (20.32×10^{-3}). At higher sputtering pressures (20 mTorr and 30 mTorr),

the situation only slightly improved with increase of sputtering power as can be observed from Table 3.4 and Figures 3.9, 3.10, and 3.11. That improvement too lasted only up to 200 W; with further rise of power to 250 W, the film characteristics showed a tendency to deteriorate again- however little maybe- due to re-sputtering effect usually encountered at high sputtering power. We can see from Table 3.5 that the Mo film deposited under a high pressure of 20 mTorr and a high power of 200 W showed the best film characteristics (grain size 6.68 nm, dislocation density 22.40×10^{-3} nm^{-2} and strain 15.19×10^{-3}) among those deposited at pressures of 20 mTorr and 30 mTorr. Further increase or decrease of power and increase of pressure produced film with smaller grain and induced much more dislocation density and strain in the films.

3.3.4 Effect of Working Pressure and Sputtering Power on Sheet Resistance of DC Sputtered Mo Thin-films

Table 3.6 below shows the variation of sheet resistance of the DC-sputtered Mo films with change of working pressures at different sputtering powers. The sheet resistance of the films continued to increase with increase in working pressure. This could easily be attributed to the way the grain size and dislocation density as well as strain of the films changed with change in pressure. The films had larger grain at lower working pressure which ensued in less grain boundaries and consequently, in lesser dislocation density and microstrain. The conduction electrons had a greater mean free flight time and path for they had to face less grain boundary scattering events with reduced boundary potential. As a result, the sheet resistance of the film decreased at lower sputtering pressures. Figure 3.15 illustrates the change of sheet resistance of the films with variation in sputtering pressures at different powers.

Table 3.6: Variation of sheet resistance with change in working gas pressure at different sputtering powers.

Sample No.	Sputtering Pressure (mTorr)	Sputtering Power (W)	Sheet Resistance (Ω/□)
1	2	100	30
3	5	100	68
5	30	100	800
6	2	150	6
7	3	150	6
8	5	150	12
9	20	150	252
10	30	150	483
11	2	200	3
12	3	200	4
13	5	200	6
14	20	200	62
15	30	200	155
16	2	250	4
17	3	250	7
18	5	250	7
20	30	250	144

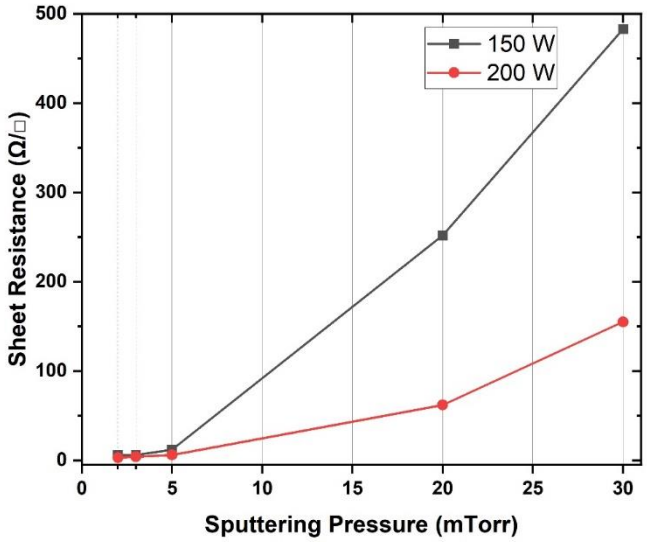

Figure 3.15: Variation of sheet resistance with variation of sputtering pressure at different working power.

It is interesting to note that the variation of sheet resistance of the films deposited at 2, 3 and 5 mTorr at higher deposition powers is very little. If we consider the films deposited at 200 W, the films deposited at 2, 3 and 5 mTorr had sheet resistance of 3, 4 and 6 Ω/□, respectively. Although the resistance increased with increase in pressure, the increment was not that significant as it was when the pressure was increased from 5 mTorr to 20 mTorr and from 20 mTorr to 30 mTorr. If the same batch of the samples were considered, when the pressure was changed to 20 mTorr, the film resistance increased from 6 Ω/□ (sample 13) to 62 Ω/□ (sample 14). Further increase of pressure to 30 mTorr caused the sheet resistance to increase more- from 62 Ω/□ to 155 Ω/□ (sample 15)- owing to smaller grain size and corresponding grater dislocation density as well as strain. Figure 3.16 depicts this little to no-change in sheet resistance of the deposited Mo films at lower working pressures.

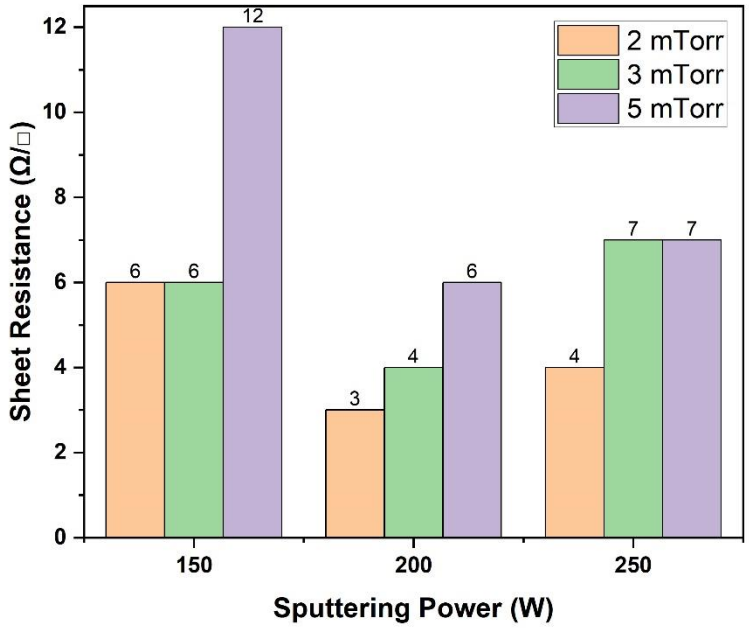

Figure 3.16: Variation of sheet resistance at pressures of 2, 3, and 5 mTorr at higher sputtering powers.

Sputtering power had a pronounced effect the change of sheet resistance of the Mo films as can be observed from the Table 3.7. The sheet resistance decreased with increase in sputtering power. Increasing sputtering power rendered the sputtered Mo atoms with higher kinetic energy which helped form larger grain with increased grain nucleation and mobility. The grain boundary thus got reduced and resulted in less dislocation density which, in turn, produced less strain in the film. As a result, the resistivity linearly proportional to average microstrain caused the sheet resistance to go down with increasing sputtering power. If we consider, for instance, the samples deposited under 30 mTorr at different sputtering powers, the distinctive effect of power could easily be recognized. The sheet resistance went from 800 Ω/□ at 100 W (sample 5) down to 144 Ω/□ at 250 W (sample 20). It is obvious from Table 3.7 that at 100 W, the sheet resistances of the films deposited at different pressures were much larger compared to those deposited at the same pressures but increased powers. Figure 3.17 demonstrates the change in sheet resistance of Mo films with change in sputtering powers at different pressures.

Table 3.7: Variation of sheet resistance with change in sputtering power at different working gas pressures.

Sample No.	Sputtering Pressure (mTorr)	Sputtering Power (W)	Sheet Resistance (Ω/□)
1	2	100	30
6	2	150	6
11	2	200	3
16	2	250	4
7	3	150	6
12	3	200	4
17	3	250	7
3	5	100	68
8	5	150	12
13	5	200	6
18	5	250	7
9	20	150	252
14	20	200	62
5	30	100	800
10	30	150	483
15	30	200	155
20	30	250	144

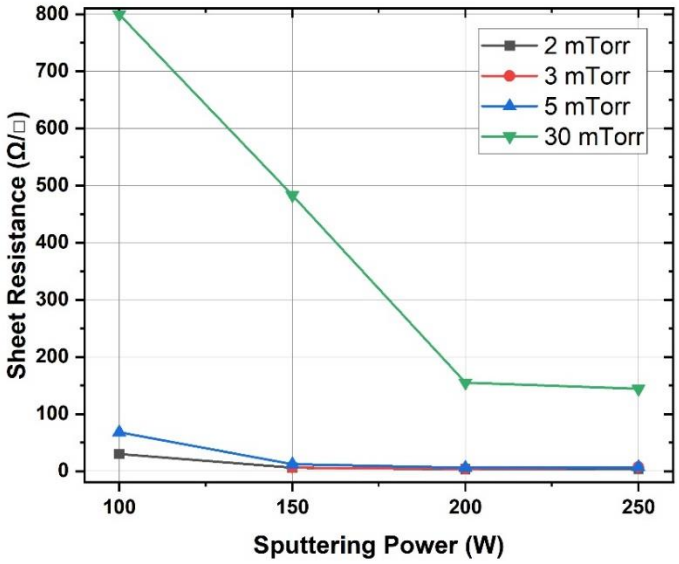

Figure 3.17: Variation of sheet resistance with variation of sputtering power at different working pressures.

So, from the data and discussion above, it is obvious that the sheet resistance decreased with lowering of working pressure and rise of sputtering power. The least sheet resistance was found from sample 11 (sputtered under a pressure of 2 mTorr and power of 200 W) which is 3 Ω/□ only. Both sample 12 (3 mTorr, 200 W) and sample 16 (2 mTorr, 250 W) had a sheet resistance of 4 Ω/□, almost equal to that of sample 11. Among the samples deposited at higher working pressures (20 mTorr and 3m mTorr), the least sheet resistance was obtained from sample 14 (62 Ω/□) which was deposited under 20 mTorr and 200 W.

3.3.5 Adhesion of DC Sputtered Mo thin-Films

Table 3.8 below listed the degree of adhesion of the DC-sputtered Mo thin-films. The degree of adhesion of the films to the substrate was indicated mainly by pass/fail. Adhesion of some of the samples was also attributed with 'Better' to indicate their comparatively better adhesion than other having rather a 'pass' status.

Table 3.8: Degree of adhesion of the DC sputtered Mo samples.

	Sample #1	Sample #2	Sample #3	Sample #4	Sample #5
Pressure (mTorr)	2	3	5	20	30
Power (W)	100	100	100	100	100
Adhesion	Fail	Fail	Fail	Fail	Fail
	Sample #5	Sample #6	Sample #7	Sample #8	Sample #9
Pressure (mTorr)	2	3	5	20	30
Power (W)	150	150	150	150	150
Adhesion	**Pass**	**Pass**	**Pass**	**Pass**	**Pass**
	Sample #11	Sample #12	Sample #13	Sample #14	Sample #15
Pressure (mTorr)	2	3	5	20	30
Power (W)	200	200	200	200	200
Adhesion	**Pass/Better**	**Pass/Better**	**Pass/Better**	**Pass/Better**	**Pass/Better**
	Sample #16	Sample #17	Sample #18	Sample #19	Sample #20
Pressure (mTorr)	2	3	5	20	30
Power (W)	250	250	250	250	250
Adhesion	**Pass/Better**	**Pass/Better**	**Pass/Better**	**Pass/Better**	**Pass/Better**

Figure 3.18 showed the result of scotch tape test for sample 12 and sample 14.

(a) (b)

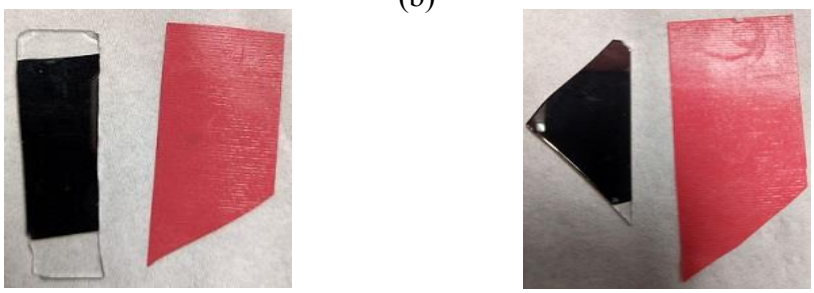

Figure 3.18: Scotch tape test of (a) sample 12 and (b) sample 14.

3.3.6 DC Sputtered Samples Selected to be Used for Bilayer and Tri-layer Mo Thin-films

Two DC-sputtered samples- sample 12 and sample 14- were selected to be used to fabricate bilayer and tri-layer Mo thin-films. The selection was done based on the properties discussed above. Table 3.9 and Table 3.10 below summarized the properties for the two samples.

Table 3.9: Summary of properties of DC sputtered sample 12 and sample 14.

	Peak Intensity (a.u.)	**FWH (°)**	**Grain Size (nm)**	**Dislocation Density ($\times 10^{-3}$) (nm^{-2})**	**Strain ($\times 10^{-3}$)**	**Sheet Resistance (Ω/□)**	**Adhesion**
Sample 12 (2 mTorr, 200 W)	779.83267	0.64463	13.1244971	5.80543358	7.67905973	4	Pass
Sample 14 (20 mTorr, 200 W)	1641.7064	1.2652	6.68086244	22.4044837	15.1905729	62	Pass/Better

Table 3.10: Use of DC Sputtered sample 12 and sample 14 in bilayer and tri-layer Mo thin-films.

	Position in BiLayer	**Position in Tri-layer**
Sample 12 (2 mTorr, 200 W)	Top	Middle
Sample 14 (20 mTorr, 200 W)	Bottom	Bottom/Top

3.4 Effect of Sputtering Parameters on Properties of RF Sputtered Mo Thin-films

3.4.1 Effect of Pressure on Grain Size, Dislocation Density and Strain of RF Sputtered Mo Samples

Table 3.11 listed the grain sizes, dislocation densities and strains for different RF-sputtered samples. The variation of the parameters with variation in working pressure is evident from the table. At all powers, with increase in pressure up to 5 mTorr, the grain size increased. It is interesting to note that both at lower pressures (2-5 mTorr) and higher pressures (20-30 mTorr), grain sizes of different samples were very close.

Table 3.11: Variation of grain size, dislocation density and strain with change in working pressure at different powers.

Sample No.	Pressure (mTorr)	Power (W)	Grain Size (nm)	Dislocation Density ($\times 10^{-3}$) (nm^{-2})	Strain ($\times 10^{-3}$)
6	2	150	10.3373535	9.357961807	9.889029
7	3	150	10.1512211	9.70428231	10.042406
8	5	150	10.7227848	8.69730744	9.4084246
9	20	150	5.8550746	29.1699128	17.310455
10	30	150	6.05318462	27.2917987	16.766961
11	2	200	11.1384855	8.06023518	9.1726188
12	3	200	11.1344222	8.06611914	9.1286443
13	5	200	12.3777114	6.52708536	8.102957
14	20	200	6.347431	24.82013	15.975922
15	30	200	6.25406906	25.5666988	16.174816
16	2	250	11.3719483	7.73268368	8.948684
17	3	250	11.915057	7.04381195	8.5135807
18	5	250	12.3710061	6.53416286	8.1372931
19	20	250	6.69013927	22.342393	15.104138
20	30	250	6.42367667	24.2344213	15.758482

As expected from the theory, both dislocation density and strain followed the trend opposite to that of grain size with increase of working pressure. Figures 3.19, 3.20 and 3.21 illustrated the change in grain size, dislocation density and strain of RF sputtered samples with variation in working pressure at different powers.

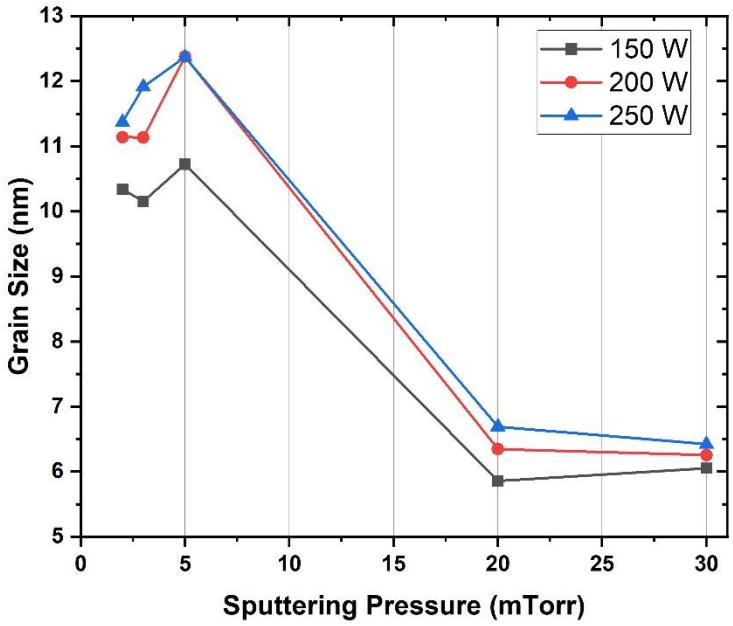

Figure 3.19: Variation of grain size of RF sputtered samples with variation in working pressure at different powers.

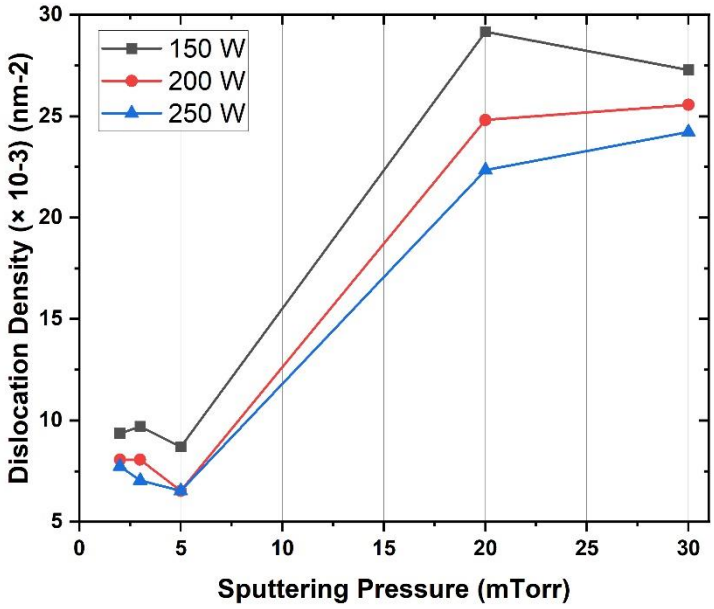

Figure 3.20: Variation of dislocation density of RF sputtered samples with variation in working pressure at different powers.

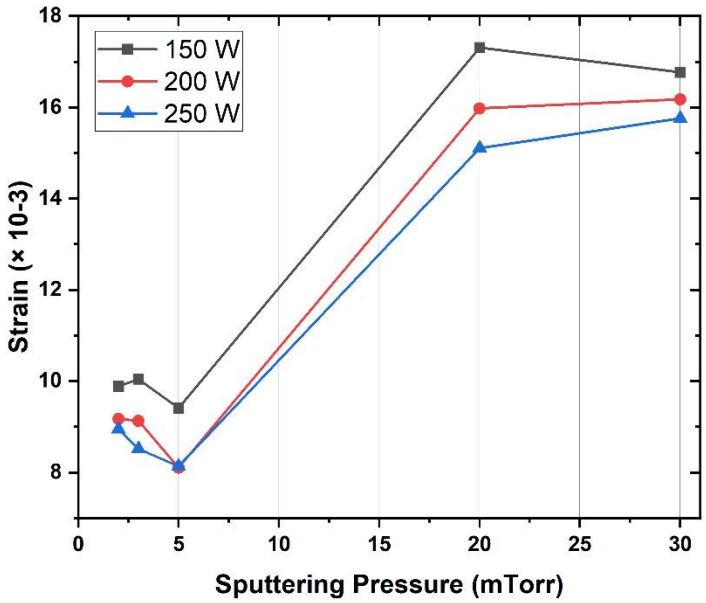

Figure 3.21: Variation of strain of RF sputtered samples with variation in working pressure at different powers.

3.4.2 Effect of Power on Grain Size, Dislocation Density and Strain of RF Sputtered Mo Samples

Sputtering power has a more pronounced effect on the grain sizes of RF sputtered films compared to the effect the working pressure has had. Table 3.12 below listed the variation of grain size along with dislocation density and strain with change in sputtering power at different working pressures. The grain size increased with increase of power at all working pressures. Conforming to the theory, dislocation density and strain decreased with increase of power and consequently, with increase of grain size. At 200 W and 250 W (at all pressures), the grain sizes were almost same, and the dislocation densities and strains were very close.

Table 3.12: Variation of grain size, dislocation density and strain of RF sputtered Mo thin-films with change in sputtering power at different pressures.

Sample No.	Pressure (mTorr)	Power (W)	Grain Size (nm)	Dislocation Density ($\times 10^{-3}$) (nm^{-2})	Strain ($\times 10^{-3}$)
6	2	150	10.33735345	9.357961807	9.889029
11	2	200	11.1384855	8.06023518	9.17261878
16	2	250	11.3719483	7.73268368	8.94868402
7	3	150	10.1512211	9.70428231	10.0424058
12	3	200	11.1344222	8.06611914	9.12864431
17	3	250	11.915057	7.04381195	8.51358072
8	5	150	10.7227848	8.69730744	9.40842459
13	5	200	12.3777114	6.52708536	8.10295697
18	5	250	12.3710061	6.53416286	8.13729307
4	20	100	4.13313491	58.5383985	24.6474737
9	20	150	5.8550746	29.1699128	17.3104554
14	20	200	6.347431	24.82013	15.9759221
19	20	250	6.69013927	22.342393	15.1041376
5	30	100	5.29030044	35.7305191	19.2317657
10	30	150	6.05318462	27.2917987	16.7669614
15	30	200	6.25406906	25.5666988	16.174816
20	30	250	6.42367667	24.2344213	15.758482

At 2 to 3 mTorrs, the grain sizes were almost identical at 200-250 W sputtering powers. Similar effect could be observed at the pressures 20 to 30 mTorrs for powers 200-250 W. Figures 3.22, 3.23 and 3.24 depict the change in grain size, dislocation density and strain with change in sputtering power at different working pressures.

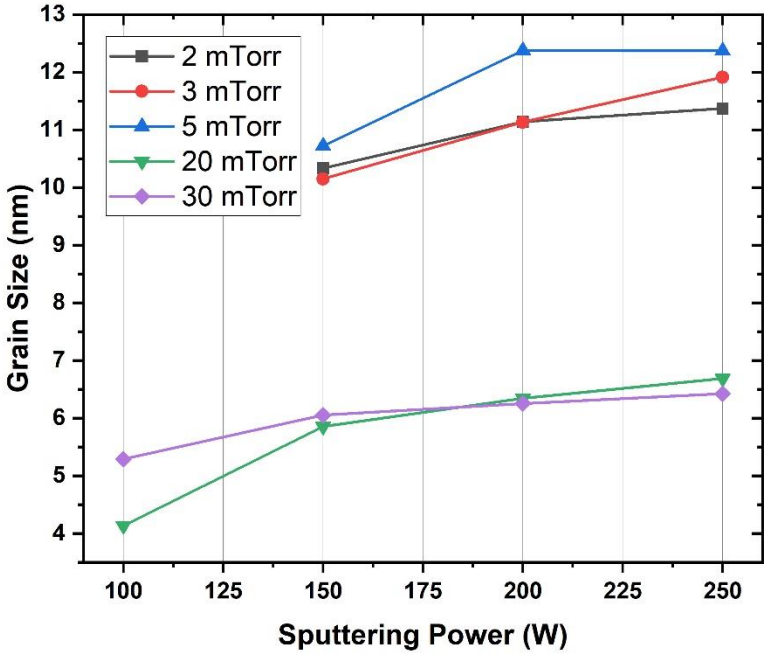

Figure 3.22: Variation of grain size of RF sputtered samples with variation in sputtering power at different pressures.

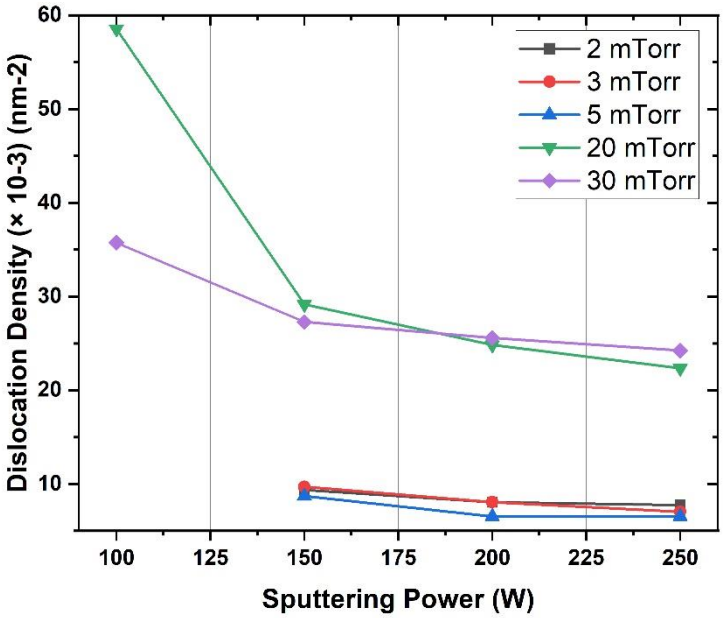

Figure 3.23: Variation of dislocation density of RF sputtered samples with variation in sputtering power at different pressures.

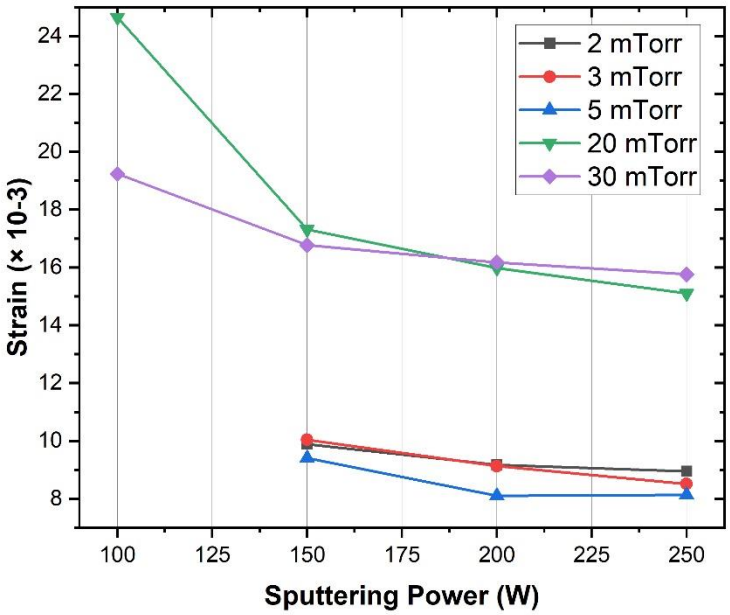

Figure 3.24: Variation of strain of RF sputtered samples with variation in sputtering power at different pressures.

From the effect of working pressure and sputtering power, it can be observed that lower pressure and higher power yielded larger grain and lower dislocation density and strain. Sample 13 which was deposited under 5 mTorr and 200 W possessed the largest grain (12.38 nm) and lowest dislocation density (6.527×10^{-3} nm^{-2}) and strain (8.10×10^{-3}). The second highest grain size was of sample 18 (deposited under 5 mTorr and 250 W)- 12.37 nm. This sample had a dislocation density of 6.534×10^{-3} nm^{-2} and strain of 8.14×10^{-3}.

3.4.3 Effect of Working Pressure and Sputtering Power on Sheet Resistance of RF Sputtered Mo Thin-films

Increase of working pressure caused, in general, the sheet resistance of RF sputtered Mo thin-films to increase. The sheet resistances of the films deposited under different sputtering pressures at all powers have been tabulated in Table 3.13. At all powers, the sheet resistances remained very close to each other for the change of pressure from 2 to 5 mTorr. Figure 3.25 depicts the change in sheet resistance with change in working pressure.

Table 3.13: Variation of sheet resistance of RF sputtered Mo thin-films with change in working pressure at different powers.

Sample No.	Pressure (mTorr)	Power (W)	Sheet Resistance (Ω/□)
1	2	100	107
2	3	100	72
3	5	100	93
4	20	100	447
5	30	100	146
6	2	150	26
7	3	150	17
8	5	150	20
9	20	150	84
10	30	150	41
11	2	200	8
12	3	200	9
13	5	200	13
14	20	200	47
15	30	200	39
16	2	250	7
17	3	250	8
18	5	250	5
19	20	250	31
20	30	250	27

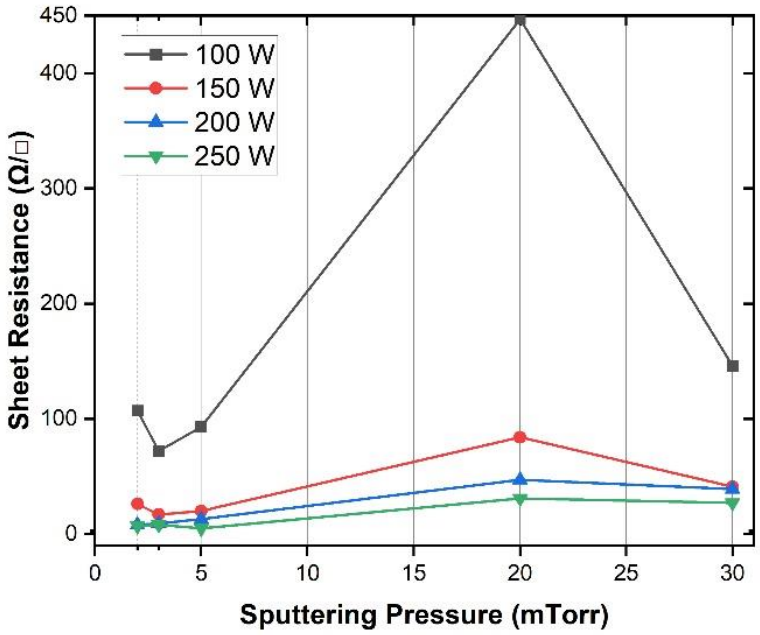

Figure 3.25: Variation of sheet resistance of RF sputtered Mo thin-films with variation in working pressure at different powers.

The sheet resistance got lowered when the power increased from 100 W to 250 W, as can be observed from the Table 3.14. At all pressures, the highest sheet resistance for the RF sputtered Mo thin-films occurred when the power was lowest- 100 W. At pressures 2 to 5 mTorrs, sheet resistances of the films deposited under 200 W and 250 W remained quite close to each other. Figure 3.26 shows the variation of sheet resistance with change in sputtering power.

Table 3.14: Variation of sheet resistance of RF sputtered Mo thin-films with change in sputtering power at different pressures.

Sample No.	Pressure (mTorr)	Power (W)	Sheet Resistance (Ω/□)
1	2	100	107
6	2	150	26
11	2	200	8
16	2	250	7
2	3	100	72
7	3	150	17
12	3	200	9
17	3	250	8
3	5	100	93
8	5	150	20
13	5	200	13
18	5	250	5
4	20	100	447
9	20	150	84
14	20	200	47
19	20	250	31
5	30	100	146
10	30	150	41
15	30	200	39
20	30	250	27

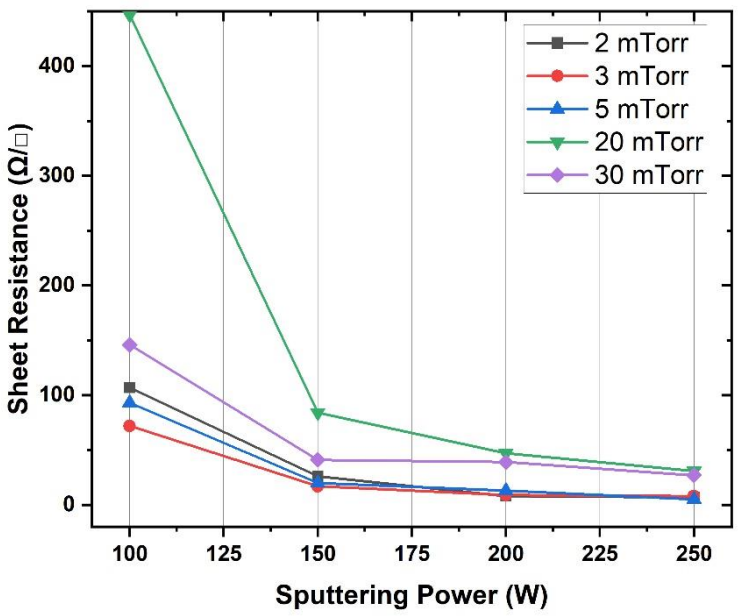

Figure 3.26: Variation of sheet resistance of RF sputtered Mo thin-films with variation in sputtering power at different pressures.

So, according to the analysis presented above, lower pressure and higher power contributed to lower the sheet resistance of the RF sputtered Mo thin-films, as expected from the theory. Sample 18 (sputtered under 5 mTorr and 250 W) had the least sheet resistance of 5 Ω/□. Sample 16 had the second lowest sheet resistance (7 Ω/□). This sample was deposited under 2 mTorr and 250 W. Among the samples sputtered under 20 mTorr and 30 mTorr, the lowest sheet resistance was possessed by sample 20- 27 Ω/□. This sample was prepared at 30 mTorr and 250 W. Sample 19 (prepared at 20 mTorr and 250 W) had a sheet resistance very close to that of sample 20- 31 Ω/□.

3.4.4 Adhesion of RF Sputtered Mo thin-Films

The degree of adhesion of the RF sputtered Mo thin-films are listed in Table 3.15 below. Similar to DC sputtered Mo thin-film samples, pass/fail indicator was used for the case of RF sputtered samples, too. Some samples which showed improved scotch tape test performance were labeled with an additional 'Better' indicator.

Table 3.15: Degree of adhesion of the RF sputtered Mo samples.

	Sample #1	Sample #2	Sample #3	Sample #4	Sample #5
Pressure (mTorr)	2	3	5	20	30
Power (W)	100	100	100	100	100
Adhesion	Fail	Fail	Fail	Fail	Fail
	Sample #5	Sample #6	Sample #7	Sample #8	Sample #9
Pressure (mTorr)	2	3	5	20	30
Power (W)	150	150	150	150	150
Adhesion	Fail	Fail	Fail	**Pass**	**Pass**
	Sample #11	Sample #12	Sample #13	Sample #14	Sample #15
Pressure (mTorr)	2	3	5	20	30
Power (W)	200	200	200	200	200
Adhesion	**Pass**	**Pass**	**Pass/Better**	**Pass/Better**	**Pass/Better**
	Sample #16	Sample #17	Sample #18	Sample #19	Sample #20
Pressure (mTorr)	2	3	5	20	30
Power (W)	250	250	250	250	250
Adhesion	**Pass**	**Pass**	**Pass/Better**	**Pass/Better**	**Pass/Better**

Figure 3.27 shows the scotch tape test result for RF sputtered Mo thin-film sample 18 and sample 19.

(a) (b)

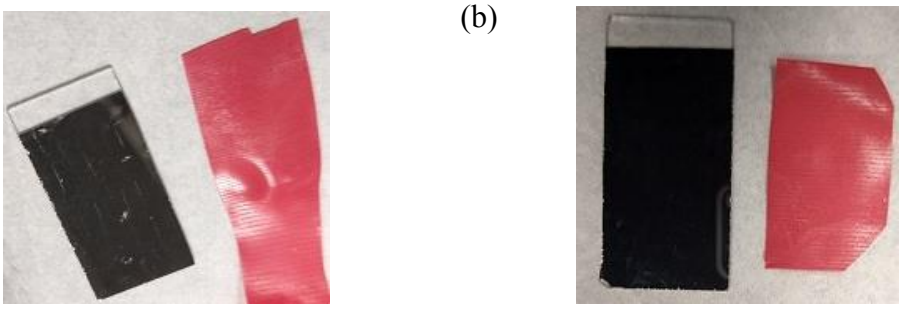

Figure 3.27: Scotch tape test of (a) sample 18 and (b) sample 19.

3.4.5 RF Sputtered Samples Selected to be Used for Bilayer and Tri-layer Mo Thin-films

Two RF sputtered samples- sample 18 and sample 19- were selected to be used to fabricate bilayer and tri-layer Mo thin-films. The selection was done based on the properties discussed above. Table 3.16 and Table 3.17 below summarized the properties for the two samples.

Table 3.16: Summary of properties of RF sputtered sample 18 and sample 19.

	Peak Intensity (a.u.)	**FWHM (°)**	**Grain Size (nm)**	**Dislocation Density ($\times 10^{-3}$) (nm^{-2})**	**Strain ($\times 10^{-3}$)**	**Sheet Resistance (Ω/□)**	**Adhesion**
Sample 18 (5 mTorr, 250 W)	517.48262	0.684	12.3710061	6.53416286	8.1372931	5	Pass/Better
Sample 19 (20 mTorr, 250 W)	1657.3921	1.26417	6.69013927	22.342393	15.104138	31	Pass/Better

Table 3.17: Use of RF sputterd sample 18 and sample 19 in bilayer and tri-layer Mo thin-films.

	Position in Bilayer	Position in Tri-layer
Sample 18 (5 mTorr, 250 W)	Top	Middle
Sample 19 (20 mTorr, 250 W)	Bottom	Bottom/Top

3.5 Investigation of Properties of DC and/or RF Sputtered Multilayer Mo Thin-films

3.5.1 Fabrication of Multilayer Mo Thin-film Samples

From our analysis of DC- and RF- sputtered Mo thin-films, some of the layers were selected based on their properties to be used as different layers of the bilayer and tri-layer Mo thin-film samples. Considering DC and RF sputtering modes, four Mo bilayer combinations and four Mo tri-layer combinations of those single layer thin-films were prepared. Table 3.18 listed all the combinations of bilayer and tri-layers with corresponding working pressure and sputtering power for each of the layers. For the bilayer Mo thin-films, bottom layer and top layer were fabricated in a row at the specified layer pressure and power. Likewise, bottom, middle, and top layers were deposited one after another in a row for the Mo tri-layer samples.

Table 3.18: Mo Bilayers and tri-layers with their corresponding pressure and power combinations.

Sample Type	Bottom Layer		Middle Layer		Top Layer	
	Sputtering Pressure (mTorr)	Sputtering Power (W)	Sputtering Pressure (mTorr)	Sputtering Power (W)	Sputtering Pressure (mTorr)	Sputtering Power (W)
DC/DC	20	200			3	200
RF/RF	20	250			5	250
RF/DC	20	250			3	200
DC/RF	20	200			5	250
DC/DC/DC	20	200	3	200	20	200
RF/RF/RF	20	250	5	250	20	250
DC/RF/DC	20	200	5	250	20	200
RF/DC/RF	20	250	3	200	20	250

3.5.2 Variation in Crystallinity and Structure of Bilayer Mo Thin-films

Figure 3.28 below displays the XRD patterns obtained for the bilayer thin-films of Mo. AS expected, all of them showed a intense peak along (110) plane, thus indicating a growth preference along this orientation. The RF(bottom)/DC(top) bilayer had the most intense (110) peak among all of the bilayer structures which indicates a highly crystallized growth of the film. The second highest intensity for the (110) peak was obtained for the DC/DC bilayer film. The peak intensities for these two bilayers (DC/DC and RF/DC) were very close. On the other hand, RF/RF and DC/RF bilayers showed almost same intensity along the (110) XRD peak.

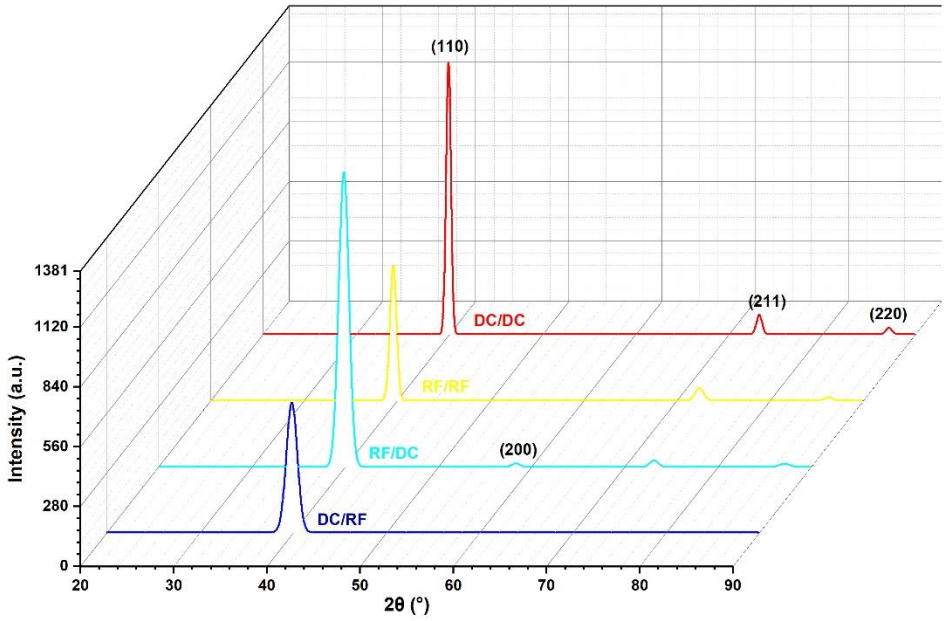

Figure 3.28: XRD Patterns obtained for Mo bilayer thin-films.

The variation of full width at half maximum (FWHM) for the XRD peak along the (110) preferred orientation for different bilayer structures are shown in Figure 3.29 below. The DC/DC bilayer had the lowest FWHM. While the RF/DC bilayer possessed the most intense (110) peak, its FWHM was quite large- even greater than that of RF/RF bilayer. The highest FWHM belonged to the DC/RF bilayer.

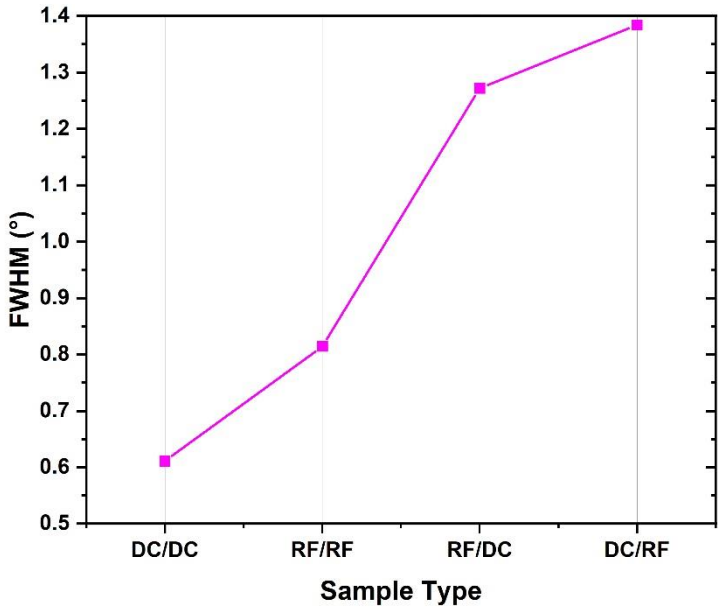

Figure 3.29: Variation of FWHM for Mo bilayer thin-films.

Since the DC/DC bilayer has got a (110) peak intensity quite close to that of RF/DC bilayer but a much greater FWHM compared to that of RF/DC structure, the DC/DC Mo bilayer thin-film is the sample possessing the maximum crystallinity among all the bilayer structures. With the lowest peak and the highest FWHM, DC/RF bilayer possessed the worst crystallinity.

3.5.3 Variation in Crystallinity and Structure of Tri-layer Mo Thin-films

Figure 3.30 illustrates the XRD patterns for the Mo tri-layer samples. The RF/RF/RF tri-layer displayed the most intense peak along the (110) preferred plane of growth of Mo. The second highest intensity along preferred orientation could be observed for the all-DC tri-layer structure. Although DC/DC/DC sample exhibited the least FWHM, both structures had very close FWHM as can be seen from Figure 3.31. Therefore, the all-RF sputtered structure could rightly be concluded to have the maximum crystallinity among the tri-layer structures. The all-DC sputtered tri-layer followed it in terms of crystal growth. With a very large FWHM,

RF/DC/RF tri-layer possessed minimum crystallinity though it had a bit higher intense peak along the (110) growth orientation compared to that of DC/RF/DC structure.

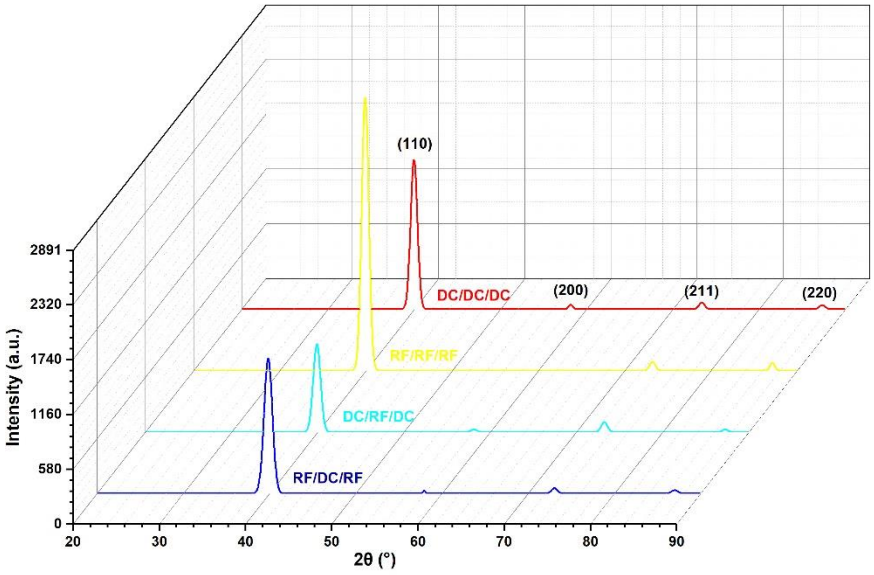

Figure 3.30: XRD Patterns obtained for Mo tri-layer thin-films.

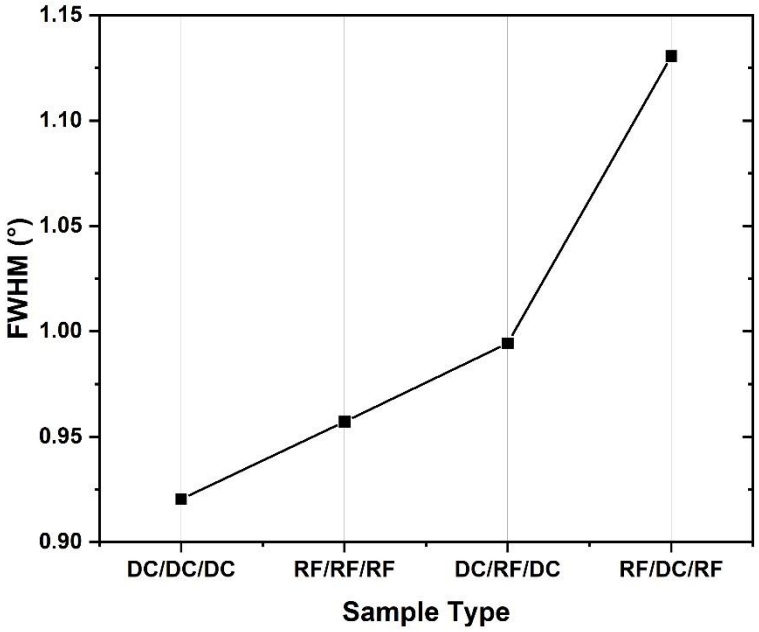

Figure 3.31: Variation of FWHM for Mo tri-layer thin-films.

3.5.4 Variation in Grain Size, Dislocation Density and Strain of Bilayer Mo Thin-films

Table 3.19 lists the grain size, dislocation density and strain for the bilayer Mo thin-films samples.

Table 3.19: Grain size, dislocation density and strain of bilayer Mo thin-films.

Sample Type	Grain Size (nm)	Dislocation Density (× 10-3) (nm-2)	Strain (× 10-3)
DC/DC	13.829355	5.22872916	7.3465691
RF/RF	10.3658099	9.306653	9.8812745
RF/DC	6.64333522	22.658318	15.3098639
DC/RF	6.105998	26.8217226	16.650397

It is evident that the DC/DC bilayer had the highest grain size among all bilayer structures. The grain size of DC/DC bilayer was more than even double of that of RF/DC and DC/RF structures. The grain sizes of RF/DC and DC/RF were almost equal. The second highest grain size was possessed by RF/RF bilayer. Keeping in line with the theory, dislocation density and strain followed the trend opposite to that of grain size. Thus DC/DC bilayer thin-film had the lowest dislocation density and strain. Figures 3.32, 3.33 and 3.34 show the variation of grain size, dislocation density and strain of different bilayer Mo thin-films.

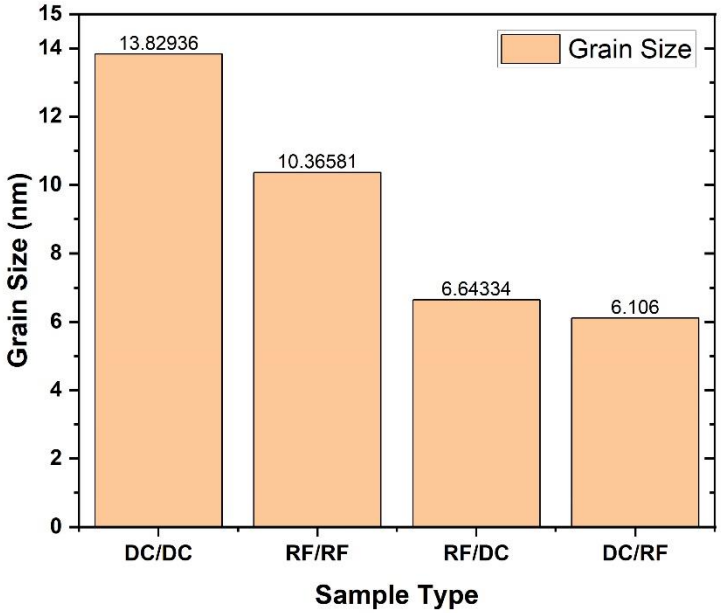

Figure 3.32: Variation of grain size of Mo bilayer thin-films.

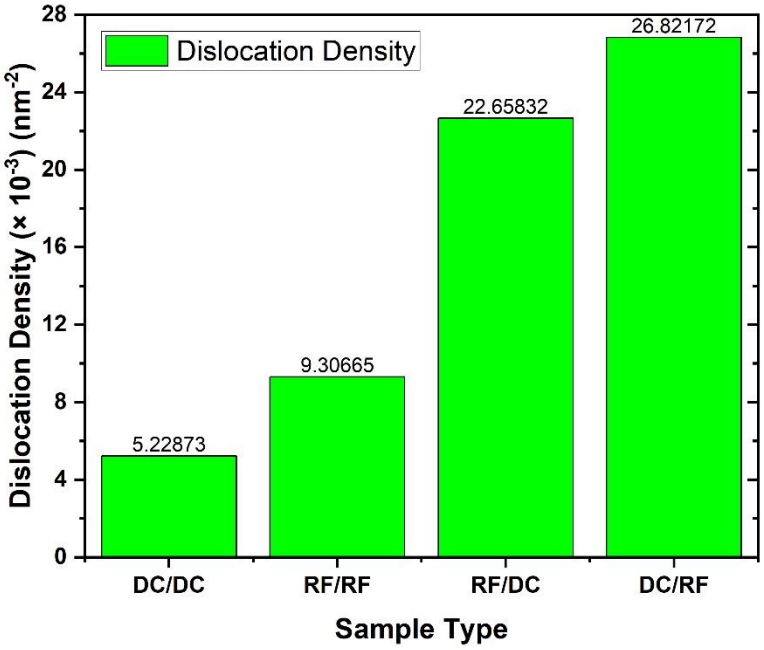

Figure 3.33: Variation of dislocation density of Mo bilayer thin-films.

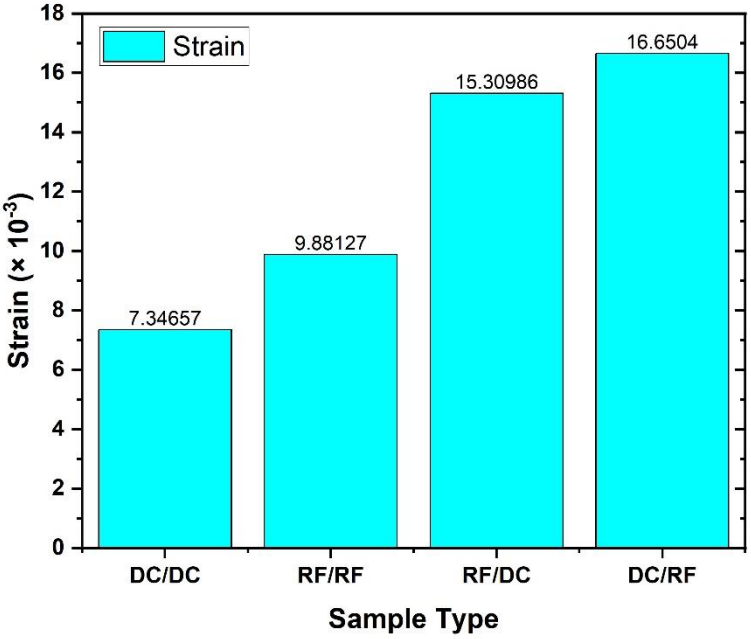

Figure 3.34: Variation of strain of Mo bilayer thin-films.

3.5.5 Variation in Grain Size, Dislocation Density and Strain of tri-layer Mo Thin-films

Table 3.20 lists the grain size, dislocation density and strain for the tri-layer Mo thin-films samples.

Table 3.20: Grain size, dislocation density and strain of tri-layer Mo thin-films.

Sample Type	Grain Size (nm)	Dislocation Density (× 10-3) (nm-2)	Strain (× 10-3)
DC/DC/DC	9.18449457	11.8546702	11.047442
RF/RF/RF	8.82928616	12.8277006	11.5088219
DC/RF/DC	8.49802356	13.8472693	11.9603681
RF/DC/RF	7.47356705	17.9037552	13.6170707

We can see that all-DC sputtered Mo thin-film had the highest grain size among all four tri-layers structures. While there was not much difference of parameters among the four

structures, the all-RF sputtered structure and DC/RF/DC structure had very close grain size, hence quite close dislocation density and strain as well. The RF/DC/RF tri-layer had the least grain size and the highest dislocation density as well as strain among all four tri-layer samples. The DC/DC/DC structure had the lowest dislocation density and strain as expected. Figures 3.35, 3.36 and 3.37 exhibited the variation of grain size, dislocation density and strain among the four tri-layer samples.

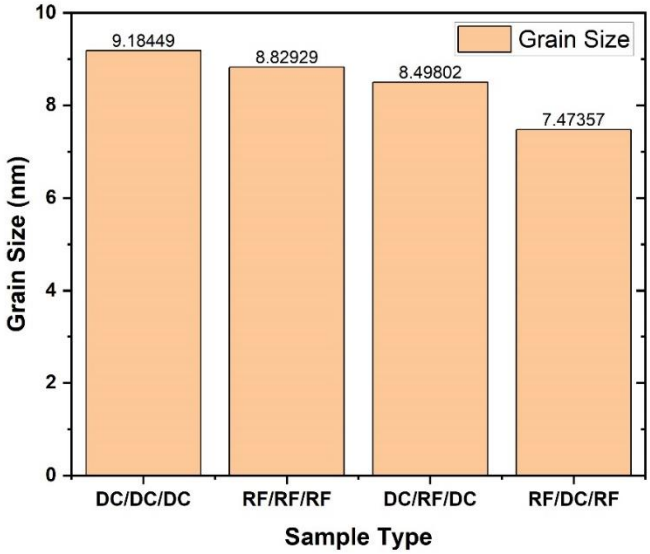

Figure 3.35: Variation of grain size of Mo tri-layer thin-films.

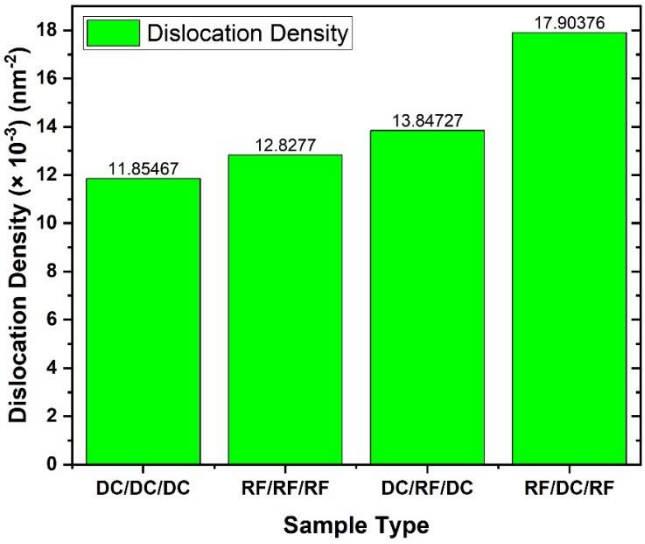

Figure 3.36: Variation of dislocation density of Mo tri-layer thin-films.

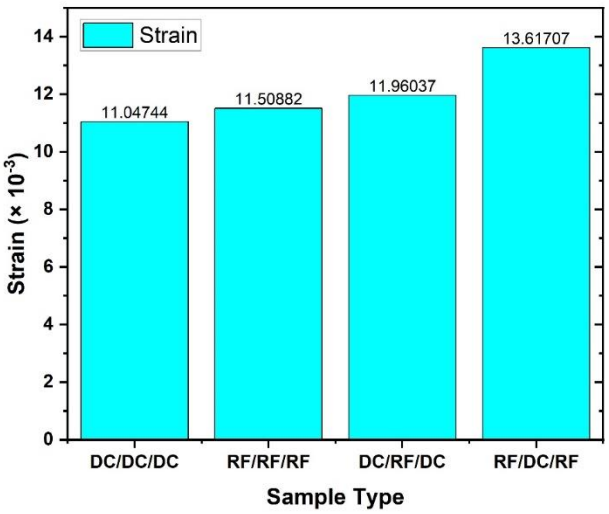

Figure 3.37: Variation of strain of Mo tri-layer thin-films.

3.5.6 Suitability of Bilayer and Tri-layer Mo Thin-films as the Back Contact of CIGS Solar Cell

The properties of Mo bilayer and tri-layer thin-film samples have been summarized in Table 3.21 below. The DC/DC bilayer structure had the highest grain size and the lowest dislocation density as well as strain among all multi-layer Mo thin-films. The RF/RF bilayer occupied the second place among the multi-layers in terms of above parameters. Although the all-DC sputtered tri-layer sample was the third in terms of grain size, dislocation density and strain, RF/RF/RF structure would be better than that in terms of crystallinity as decided in section 3.5.3.

Table 3.21: Summary of properties of Mo bilayer and tri-layer samples.

Sample type	Grain Size (nm)	Dislocation Density (× 10-3) (nm-2)	Strain (× 10-3)	Sheet Resistance (Ω/□)	Adhesion
DC/DC	13.829355 (Highest)	5.22872916 (Lowest)	7.3465691 (Lowest)	2 - 8	Pass/better
RF/RF	10.3658099 (Second Highest)	9.306653 (Second Lowest)	9.8812745 (Second Lowest)	2 - 6	Pass/Better
RF/DC	6.64333522	22.658318	15.3098639	2 - 6	Pass
DC/RF	6.105998	26.8217226	16.650397	2 - 6	Pass
DC/DC/DC	9.18449457 (Third Highest)	11.8546702 (Third Lowest)	11.047442 (Third Lowest)	2 - 6	Pass/Better
RF/RF/RF	8.82928616	12.8277006	11.5088219	2 - 6	Pass/Better
DC/RF/DC	8.49802356	13.8472693	11.9603681	2 - 6	Pass/Better
RF/DC/RF	7.47356705	17.9037552	13.6170707	2 - 6	Pass

Both all-DC and all-RF sputtered structures were very close to each other in terms of every structural parameters (i.e. grain size, dislocation density and strain). Consequently, more intense growth along the (110) preferred orientation compared to that of all-DC sputtered structure would make RF/RF/RF thin-film more suitable among all tri-layer samples, effectively making it more suitable just after the RF/RF bilayer Mo thin-film. The other two tri-layers, DC/RF/DC and RF/DC/RF exhibited better performance than the remaining bilayer structures- RF/DC and DC/RF bilayer samples. The sheet resistance and adhesion of the samples were quite close.

3.6 Comparison and Conclusion

Table 3.22 presents a comparison among those single layer, bilayer and tri-layer Mo thin-films which exhibited the best of the properties required to having them function as back electrode of CIGS solar cell.

Table 3.22: Comparison of single layer, bilayer and tri-layer Mo thin-film samples.

	Peak Intensity (a.u.)	**FWHM (°)**	**Grain Size (nm)**	**Dislocation Density ($\times 10^{-3}$) (nm^{-2})**	**Strain ($\times 10^{-3}$)**	**Sheet Resistance (Ω/□)**	**Adhesion**
Sample 12 (2 mTorr, DC 200 W)	779.83267	0.64463	13.1244971	5.80543358	7.67905973	4	Pass
Sample 14 (20 mTorr, DC 200 W)	1641.7064	1.2652	6.68086244	22.4044837	15.1905729	62	Pass/Better
Sample 18 (5 mTorr, RF 250 W)	517.48262	0.684	12.3710061	6.53416286	8.1372931	5	Pass/Better
Sample 19 (20 mTorr, RF 250 W)	1657.3921	1.26417	6.69013927	22.342393	15.104138	31	Pass/Better
DC/DC	1272.28697	0.61112	13.829355	5.22872916	7.3465691	2 - 8	Pass/Better
RF/RF	635.43599	0.81445	10.3658099	9.306653	9.8812745	2 - 8	Pass/Better
RF/RF/RF	2892.0488	0.95718	8.82928616	12.8277006	11.5088219	2 - 6	Pass/Better
DC/DC/DC	1580.8186	0.92034	9.18449457	11.8546702	11.047442	2 - 6	Pass/Better

It can be seen from Table 3.22 that the DC/DC bilayer possessed the desired characteristics of Mo thin-film the most- good crystallinity, maximum grain size, minimum dislocation density, strain and sheet resistance, and better adhesion. DC sputtered single layer Mo thin-film- sample 12- had almost similar characteristics- except a bit lower crystallinity and

adhesion. Sample 18, which is a RF sputtered single layer film, was close enough to the DC/DC bilayer and DC sputtered single layer in terms of the film properties as observed from the table. These are the most suitable three Mo thin-films to be employed as the back electrode for the CIGS solar cell. Next, RF/RF bilayer and RF/RF/RF tri-layer thin-films could be considered for the back contact. Although the all-RF sputtered and all-DC sputtered structures exhibited intense crystallization peak, the films' grain size and dislocation density as well as strain did not seem to closing on those of the first three structures as discussed above.

CHAPTER IV

CIGS PERFORMANCE OPTIMIZATION AND ANALYSIS THROUGH NUMERICAL SIMULATION

4.1 Introduction

The CIGS solar cell has a device structure of the substrate/back contact/p-type absorber layer/n-type buffer layer/window layer as displayed in Figure 4.1. Besides applying different fabrication techniques, a range of materials has been employed for every individual layer to maximize the output of the solar cell.

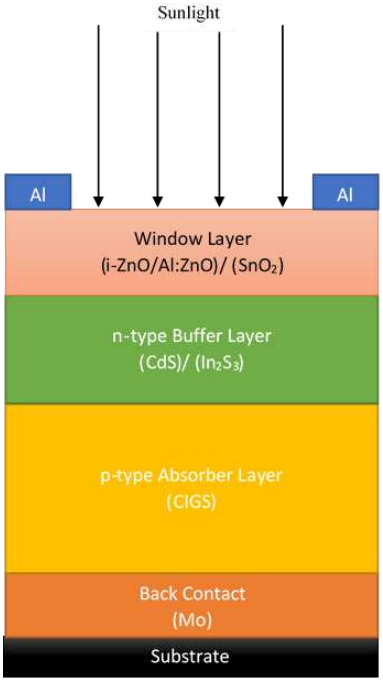

Figure 4.1: Structure of CIGS solar cell.

Molybdenum (Mo) is extensively used for the back contact as it possesses better chemical steadiness, mechanical stability, conductivity, and adhesion to the substrates compared to other materials. As the p-type absorber material, CIGS possesses a good absorption coefficient of 10^5 cm^{-1} [13] and a wide as well as variable bandgap. Contingent upon the Ga/In ratio, the CIGS bandgap can be tuned between 1.10 – 1.69 eV [14]. As a result, it can absorb maximum incident photons at longer wavelengths rendering it much thinner compared to the conventional crystalline Si solar cell.

For the buffer layer, cadmium sulfide (CdS) has traditionally been employed as it has resulted in the highest conversion efficiency despite the complexities of its fabrication. However, the toxicity of CdS has led the researchers to search of non-toxic and wide-bandgap alternatives. A good number of materials have been tested so far including indium sulfide (In2S3), zinc sulfide (ZnS), zinc selenide (ZnSe), Zn1-xMgxO etc. As the buffer layer plays a critical role in allowing the maximum amount of incident light pass through the absorber layer and creating a p-n junction with it, the In2S3 with its higher bandgap and lower absorption may well replace the conventional CdS [73]. ZnO is mostly used for the window layer. Since the window layer must transmit across the solar spectrum and act as the front electrode, high conductivity and optical transmittance are desired for the employed material. In this work, another promising optoelectronic material, fluorine-doped tin-oxide (SnO:F or SnO2 only) has been employed besides the ZnO.

The objective of the present research is to maximize CIGS solar cell performance by optimizing different material characteristics. The conventional structure of the CIGS solar cell was first considered for this purpose. Then the buffer layer and the window layer were changed, and their important material parameters were optimized to extract the highest solar cell output.

So different CIGS structures emerged and performances of those were then compared to each other. Finally, the output of the optimized structures was compared to that of some reported laboratory research cells.

4.2 Materials and Methods

4.2.1 Structures of CIGS Solar Cell Device

The conventional structure of CIGS solar cell includes CdS as a buffer layer and a bilayer of ZnO as a window layer. As shown in Figure 4.1 above, the back contact, primarily Mo, is deposited or grown on a substrate. Glass substrate is mostly used for this purpose. The p-type CIGS absorber layer can be deposited on the back contact in several ways such as sputtering, CVD, spray pyrolysis etc. The bilayer of the ZnO consists of an intrinsic ZnO layer (i-ZnO) and another Al-doped ZnO layer (Al:ZnO) layer. Not only ZnO, most of the transparent conducting oxide that are employed as the window layers are n-type. After optimizing this conventional CIGS structure for the highest efficiency, the ZnO window layer was then replaced by the fluorine-doped tin oxide (SnO_2). This structure differed from the previous one in the thickness of the window layer. The solar cell parameters were optimized. Next, the cell structure was modified by inserting In_2S_3 instead of the CdS buffer layer. With In_2S_3 as the buffer layer and ZnO bilayer as the window, the parameters were varied, and the structure was optimized to realize maximum solar cell efficiency. For the last structure, SnO_2 was combined with the In_2S_3 buffer layer.

4.2.2 Modeling and Cell Parameters of the CIGS Solar Cell

For numerical modeling and simulation, the One-Dimensional Solar Cell Capacitance Simulator or, in brief, SCAPS-1D software was employed. This is an open-source software

developed for thin film heterojunction solar cells especially for the two chalcogenides viz. CIGS and CdTe solar cells [74]. Nearly all types of dc and ac electrical characteristics of the heterojunction thin film solar cell such as open-circuit voltage (VOC), short-circuit current density (JSC), fill factor (FF), efficiency (η), internal quantum efficiency (IQE), the energy band structure of the heterojunctions, capacitance-voltage spectroscopy etc. can be simulated using this 1D simulator. The SCAPS-1D, compared to other simulation programs, facilitates the highest number of DC and AC electrical measurements under dark and light conditions. Almost all the material properties- both physical and electronic-, starting from the layer thickness to even the defect level of the interfaces, can be quantified and modified as required. Different spectrum profile for illumination, generation and recombination profile, temperature variation etc. are available for the desired test conditions.

The properties of the different materials for different layers of the CIGS solar cell were first input to the software. The parameters input to the software are displayed in Table 4.1. Four different CIGS structures were modeled and simulated in this work:

- CIGS Solar Cell Structure I: p-CIGS/n-CdS/i-ZnO/Al:ZnO
- CIGS Solar Cell Structure II: p-CIGS/n-CdS/SnO_2
- CIGS Solar Cell Structure III: p-CIGS/n-In_2S_3/i-ZnO/Al:ZnO
- CIGS Solar Cell Structure IV: p-CIGS/n-In_2S_3/SnO_2

The metallic work function and the reflectivity of the Mo back contact were set to 4.95 eV and 80%, respectively. The front contact transmittivity was set from 90% - 95%. The work function of Al front grid contact was fixed at 4.06 eV. The thermal velocity of electrons and holes was kept constant at 1×10^7 cm/s. The numerical simulations were performed under global air mass AM 1.5G and power density of 1000 W/m^2, the standard test condition for illumination.

The temperature was 300 K for most of the simulations except the cases where the temperature was varied to determine its impact on the solar cell performances. The J-V characteristic curves were numerically constructed and analyzed to obtain the essential solar cell parameters: open-circuit voltage, short-circuit current, fill factor and efficiency. The internal quantum efficiency (QE) was also determined. The batch setting of the software was used to initiate the change of the input parameters and the recorder setting of the software to obtain the desired output parameters.

Table 4.1: Material parameters employed in simulation for different layers of the CIGS solar cell.

Parameters (unit)	p-type Absorber (CIGS)	n-type Buffer (CdS)	n-type Buffer (In_2S_3)	n-type Window (i-ZnO)	n^+-type window (ZnO:Al)	n^+-type Window (SnO_2)
Thickness (μm)	0.5 – 4.0	0.04 – 0.2	0.04 – 0.2	0.04 –0.2	0.1	0.04 – 0.2
Bandgap (eV)	1.0 – 1.6	2.4	2.1 – 2.75	3.3	3.3	3.6
Electron Affinity (eV)	4.2 - 4.35	4.2	4.65	4.45	4.45	4.41
Relative Dielectric Permittivity	13.6	10	13.5	9	9	9
CB Effective Density of States (cm^{-3})	2.2×10^{18}	2.2×10^{18}	1.8×10^{19}	2.2×10^{18}	2.2×10^{18}	2.2×10^{18}
VB Effective Density of States (cm^{-3})	1.8×10^{19}	1.8×10^{19}	4×10^{13}	1.8×10^{19}	1.8×10^{19}	1.8×10^{19}
Electron Mobility (cm^2/V-s)	100	100	400	100	100	100
Hole Mobility (cm^2/V-s)	25	25	210	25	25	25
Donor Density (cm^{-3})	10	1×10^{15} – 1×10^{18}	1×10^{15} – 1×10^{18}	1×10^{18}	1×10^{20}	1×10^{19}
Acceptor Density (cm^{-3})	1×10^{15} – 2×10^{18}	10	10	10	10	10
Defect Density (cm^{-3})	1×10^{14}	1×10^{15}	1×10^{15}	1×10^{15}	1×10^{15}	1×10^{15}

4.3 Results and Discussion

4.3.1 Optimization of Solar Cell Structure I: p-CIGS/n-CdS/i-ZnO/ZnO:Al

The structure p-CIGS/n-CdS/i-ZnO/ZnO:Al was first considered. The thicknesses of the p-type CIGS absorber layer, n-type CdS buffer layer and i-ZnO window layer were varied to achieve the least thin film with optimum solar cell performance. The bandgap and impurity atom concentration of CIGS, and the impurity concentration of CdS were also changed to observe their effect on the performance. After optimizing these parameters, the impact of temperature on solar cell performance was investigated.

In the beginning, the bandgap of the CIGS absorber layer was varied from 1.0 eV to 1.6 eV. The variation of the solar cell performance indicators- open-circuit voltage, short-circuit current density, fill factor, and efficiency- with the change in CIGS bandgap are shown in Figure 4.2 and Figure 4.3. The open-circuit voltage (V_{OC}) increased with the increase of the CIGS bandgap. Starting from the 0.6411 V, it had increased linearly before the curve flattened at around 1.4 eV bandgap with an open-circuit voltage of 0.9207 V. The short-circuit current density (J_{SC}) gradually decreased from 40.02 mA/cm^2 to 20.25 mA/cm^2 with the bandgap. Like V_{OC}, an almost similar increasing and flattening trend was observed in the fill factor (FF) variation. The efficiency (η) of the CIGS solar cell peaked around 23.3% at the CIGS bandgap of 1.15 eV. As only photons with energy greater than the bandgap value contribute to the generation of electron-hole pair, with the increase of CIGS bandgap, the efficiency sharply declined, only around 16% when the bandgap was 1.6 eV.

Keeping the CIGS bandgap fixed at 1.15 eV, its acceptor impurity concentration was then varied from 1×10^{15} to 2×10^{18} atoms/cm^3. The highest efficiency was achieved when the

concentration was 2×10^{18} cm^3. Both the fill factor and open-circuit voltage showed an increasing trend with the increase in acceptor concentration, from 80.3% to around 85.5% for fill factor and from 0.56 V to 0.78 V for open-circuit voltage. The short-circuit current density dropped from 37.5 mA/cm^2 to almost 34.8 mA/cm^2. Consequently, the efficiency increased from 17% at 1×10^{18} cm^{-3} to 23.4% at a concentration of 2×10^{18} cm^{-3}. The effect of thickness variation on the performance of the CIGS solar cell was then investigated. The thickness was varied from 0.5 μm to 4 μm. The cell reached an efficiency of 25% when CIGS layer was 4 μm thick. The efficiency was only 17% with only 0.5 μm thick absorber layer. With increasing thickness, the absorber layer could absorb more incident photons at a higher wavelength and the recombination of photo-generated carriers at the back contact would decrease. Hence, higher efficiency was achieved with the increase of the absorber layer. For the optimal CIGS absorber layer, a thickness of 2 μm was chosen with an efficiency of 23.4%. Since both indium and gallium are hardly abundant in nature and cost high, a thin CIGS film tends to be cost-effective and, in turn, desirable. All other solar cell parameters showed an increasing trend with the increase in CIGS thickness. The optimum bandgap for CIGS was found to be 1.15 eV, acceptor concentration 2×10^{18} cm^{-3} and the thickness was chosen to be 2 μm.

Next, the n-type CdS buffer layer was considered for the optimization of its parameters. Its donor ion concentration was increased from 1×10^{15} to 1×10^{18} cm^{-3}. Although the open-circuit voltage barely showed change, the short-circuit current density showed a change from 34.6 mA/cm^2 to 34.76 mA/cm^2. The fill factor peaked at 6.67×10^{17} cm^{-3} with a value of 85.61%. Starting from almost 23.23%, the efficiency gradually increased to be around 23.4% at the donor concentration of 6.67×10^{17} cm^{-3}. Then the CdS thickness was varied from 0.04 μm to 0.2 μm. The open-circuit voltage showed almost no change with the increasing buffer layer thickness.

The short-circuit current density reached a peak of around 0.045 µm with a density of 34.7 mA/cm^2. Both the fill factor and efficiency decreased with increasing buffer layer thickness. This is because the thicker the buffer layer, the fewer the number of photons would be to reach the absorber layer. That is why the efficiency of the cell was lowered with increasing CdS thickness. The donor concentration of 6.67×10^{17} cm^{-3} and the CdS thickness of 0.045 µm were chosen as the optimum values.

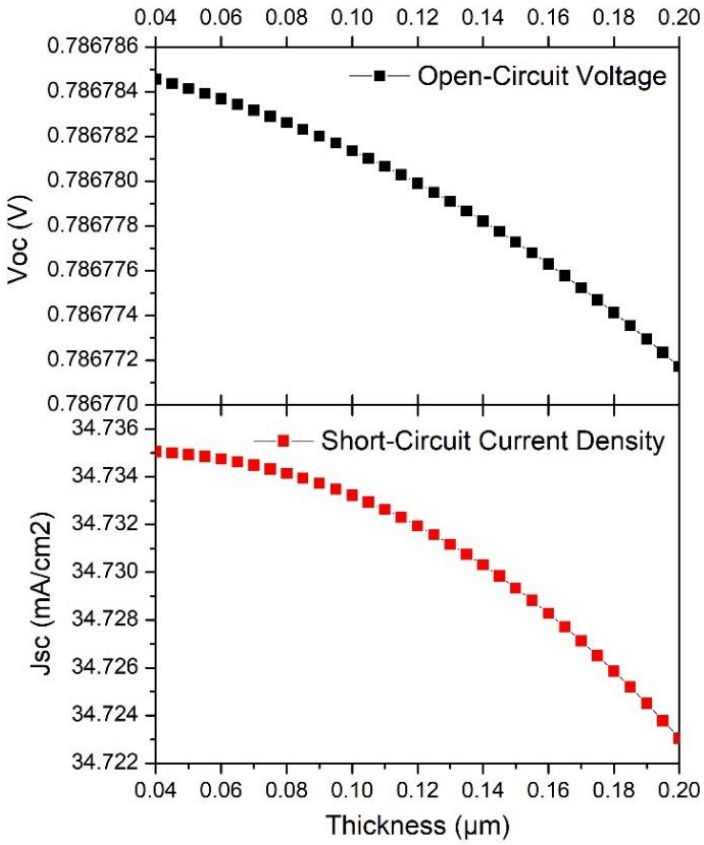

Figure 4.2: Change of V_{OC} and J_{SC} with change in CIGS bandgap of p-CIGS/n-CdS/i-ZnO/ZnO:Al structure.

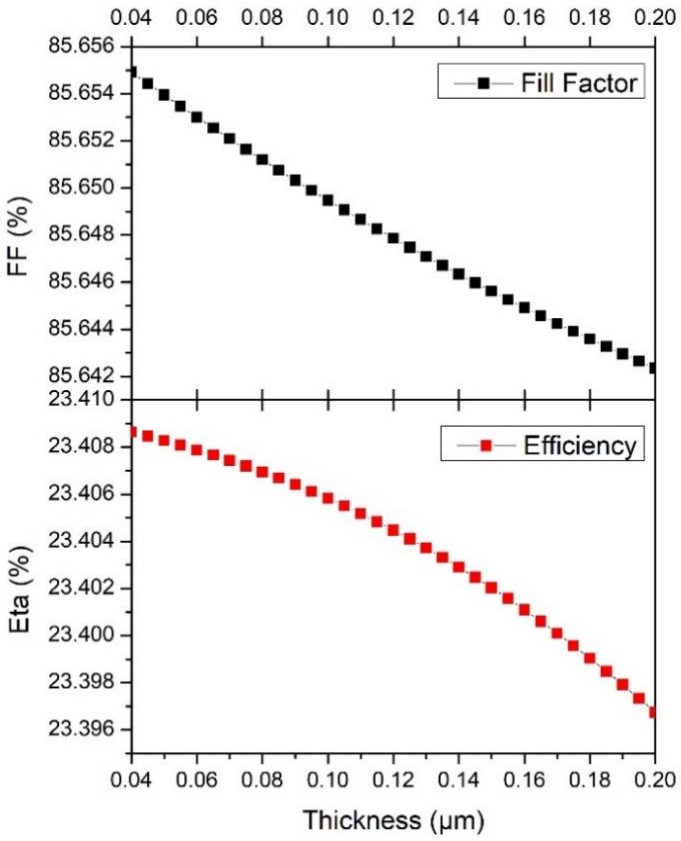

Figure 4.3: Change of fill factor and efficiency with change in CIGS bandgap of p-CIGS/n-CdS/i-ZnO/ZnO:Al structure.

Then the thickness of the intrinsic ZnO layer was varied from 0.04 µm to 0.2 µm. The CIGS bandgap, its acceptor concentration and thickness were set at their optimal values. The thickness and the donor concentration of the CdS layer were also set at the values obtained above. Having all other parameters set at their optimum values, the efficiency dropped to 23.39% when the i-ZnO layer was 0.2 µm thick. Therefore, the optimum thickness for the i-ZnO layer was chosen to be 0.04 µm. Although the resulting difference between the efficiencies for the i-ZnO thicknesses of 0.04 µm and 0.2 µm might be perceived as insignificant at first, it could play a crucial role in reducing the cost of the solar module [75]- as put by Solibro, one of the formerly leading manufacturers of CIGS thin-film modules. The less thickness and, in turn, reduced quantity of the window materials allow to compensate for the higher cost associated with the

metal grid used for the front contact of the solar module. The metal grid improves the collection of the charge carriers and thereby, increases the module's fill factor as well as efficiency. An efficiency of 23.4086% was achieved from the optimized cell. The corresponding open-circuit voltage and the short-circuit current density were 0.7868 V and 34.7351 mA/cm^2, respectively. The fill factor associated was 85.6549%.

The effect of temperature on the solar cell performance was then examined. The temperature was varied from 273 K to 375 K. As can be seen from the Figure 4.4, the cell performance decreased with increasing temperature. The efficiency saw a decline from 23.4086% at 300 K to 18.67% at 375 K. Though short-circuit current density remains nearly constant, the open-circuit voltage fell conspicuously due to its dependence on saturation current which tends to fall fast with increase in temperature. The fill factor dropped off at higher temperature as well.

Both dark and light simulation were performed for the p-CIGS/n-CdS/i-ZnO/ZnO:Al solar cell structure. The structure comprised of the layers having the optimized parameters as obtained above. The Figure 4.5 showed the J-V characteristics for both dark and illuminated simulation and the Figure 4.6 displayed the quantum efficiency of the cell. The energy band diagram of the optimized structure is shown in Figure 4.7. The energy level of each layer of the structure is duly indicated in the diagram.

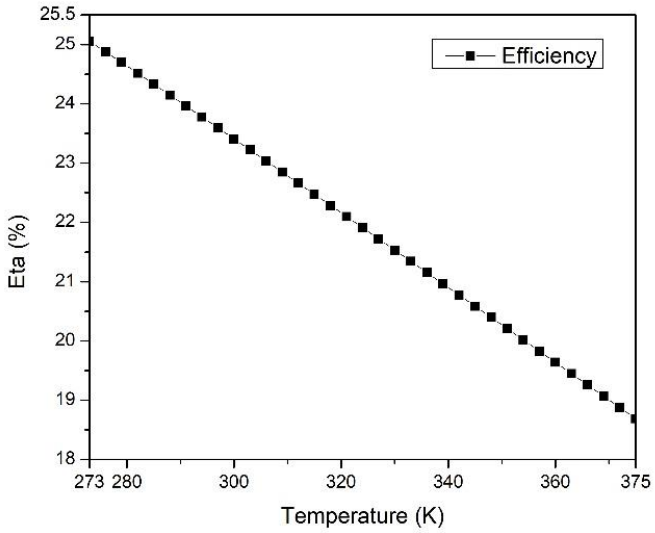

Figure 4.4: Change of efficiency with change in temperature of p-CIGS/n-CdS/i-ZnO/ZnO:Al structure.

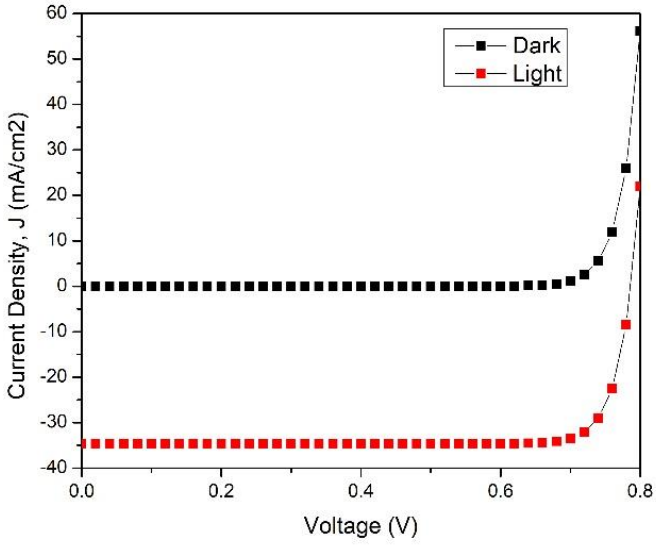

Figure 4.5: J-V characteristics of p-CIGS/n-CdS/i-ZnO/ZnO:Al structure under dark and light conditions.

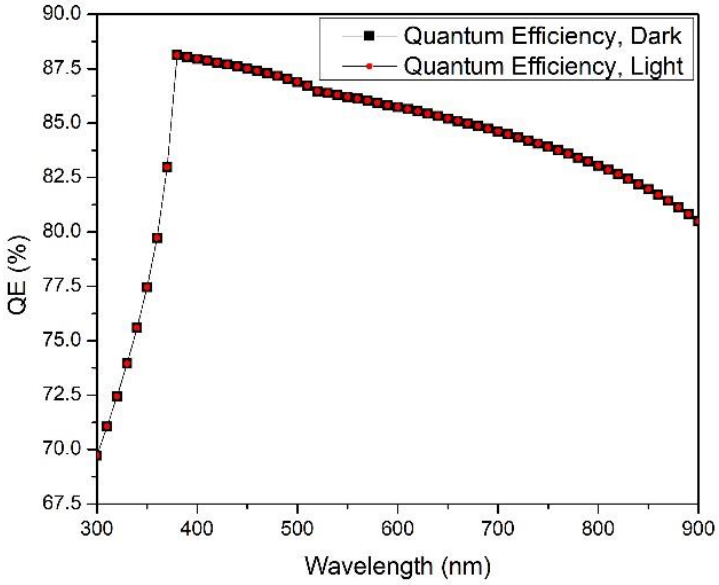

Figure 4.6: Quantum efficiency variation for p-CIGS/n-CdS/i-ZnO/ZnO:Al structure. both dark and light curves overlapped.

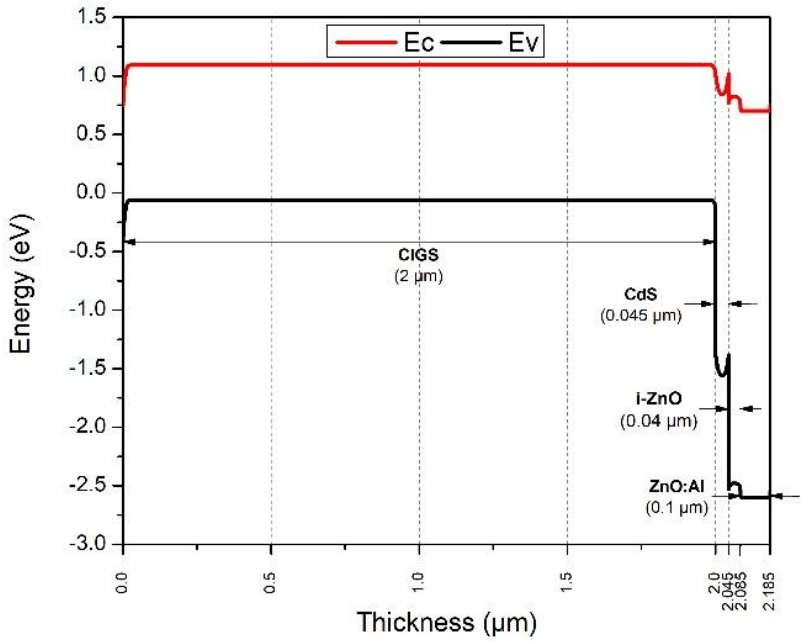

Figure 4.7: Energy band diagram for the optimized p-CIGS/n-CdS/i-ZnO/ZnO:Al structure.

4.3.2 Optimization of Solar Cell Structure II: p-CIGS/n-CdS/SnO_2

In this section, the solar cell structure p-CIGS/n-CdS/SnO_2 was considered to investigate the effects of the SnO_2 window layer instead of the ZnO. The associated parameters with the SnO_2 layer are provided in the Table 4.1. The optimized parameters for the CIGS and CdS layers obtained from the section 4.3.1 are included in this structure. Other parameters of these two layers are as listed in the Table 4.1.

The thickness of the SnO_2 layer was varied from 0.04 μm to 0.2 μm to explore its effect on the cell performance. The open-circuit voltage, short-circuit current density, fill factor and efficiency are plotted in Figure 4.8 and Figure 4.9. While the decrease in the cell parameters with the SnO_2 thickness is very slight, it is quite interesting to see that the cell has an efficiency of 23.4777% with a window layer thickness of 0.05 μm only whereas the ZnO layer took a total of 0.14 μm to produce an efficiency of 23.4086%. The optimum thickness for the SnO_2 layer was determined to be 0.05 μm. The corresponding fill factor of the cell at this window layer thickness was 85.6958%. The open-circuit voltage and the short-circuit current density were found 0.7869 V and 34.8176 mA/cm^2, respectively.

The cell was then simulated with varying temperature in the range of 273 K to 375 K. As expected, the efficiency of the cell dropped to around 18% at 375 K from 23.4777% efficiency at 300 K (Figure 4.10), since all the cell parameters considered here, including the efficiency, are strongly temperature dependent. As the reverse-saturation current increases with temperature, V_{OC} tends to decrease due to reduction in saturation current. The J-V characteristics from the dark and light simulation of the p-CIGS/n-CdS/SnO_2 cell structure are shown in Figure 4.11. The structure included all the optimized parameters both from this section and section 3.1 for

different cell layers. The quantum efficiency and the energy band diagram of this cell structure are also illustrated in the Figure 4.12 and Figure 4.13.

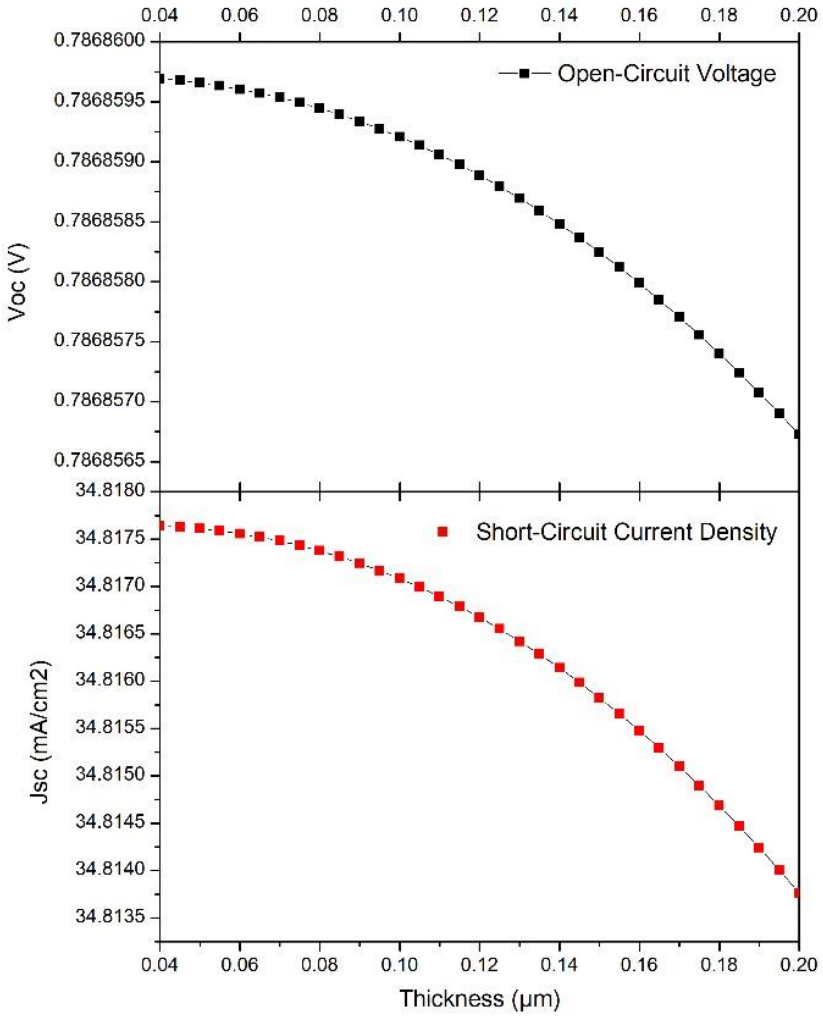

Figure 4.8: Change of V_{OC} and J_{SC} with change in SnO_2 thickness of p-CIGS/n-CdS/SnO_2 structure.

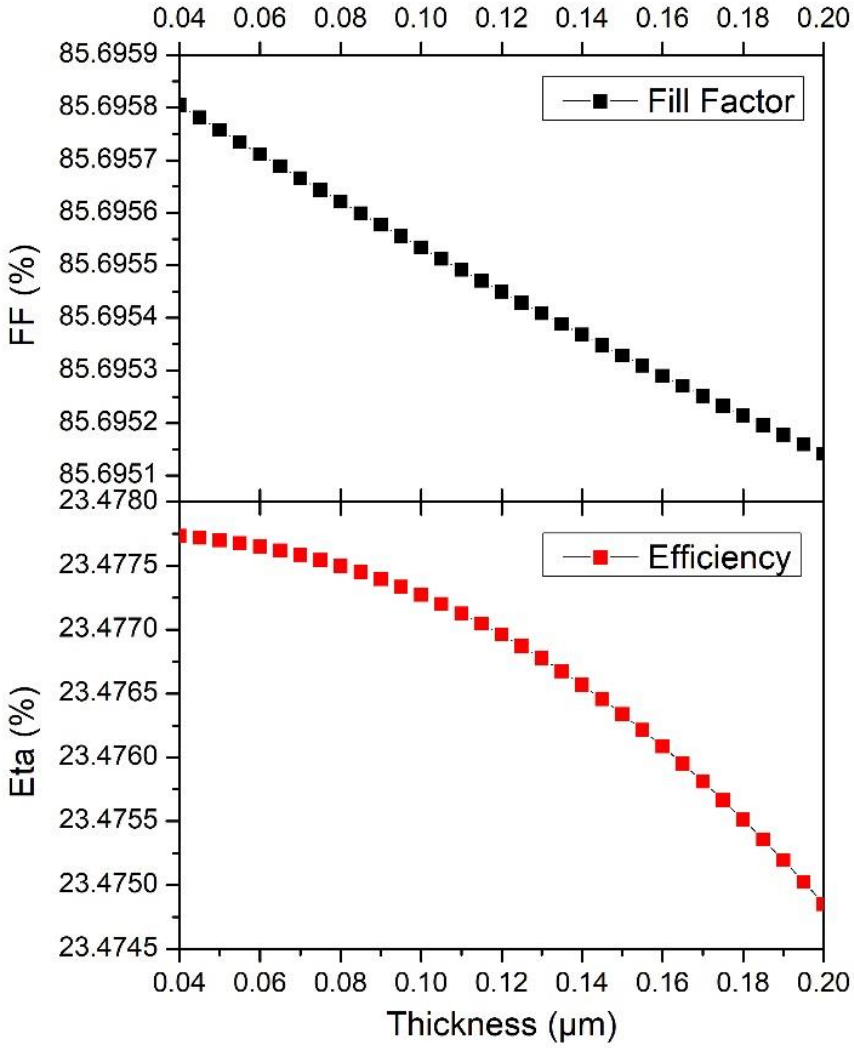

Figure 4.9: Change of fill factor and efficiency with change in SnO_2 thickness of p-CIGS/n-CdS/SnO_2 structure.

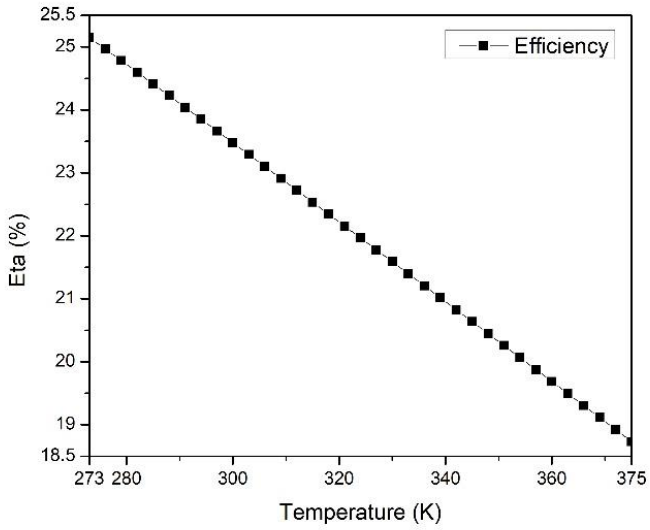

Figure 4.10: Change of efficiency with change in temperature of p-CIGS/n-CdS/SnO_2 structure.

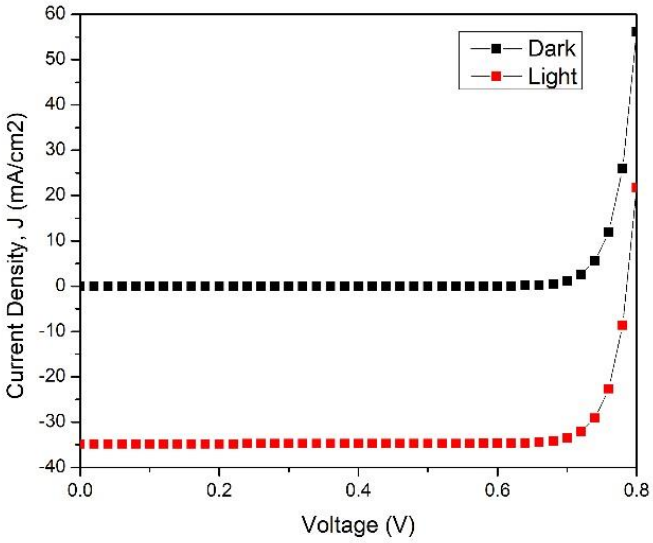

Figure 4.11: J-V characteristics of p-CIGS/n-CdS/SnO_2 structure under dark and light conditions.

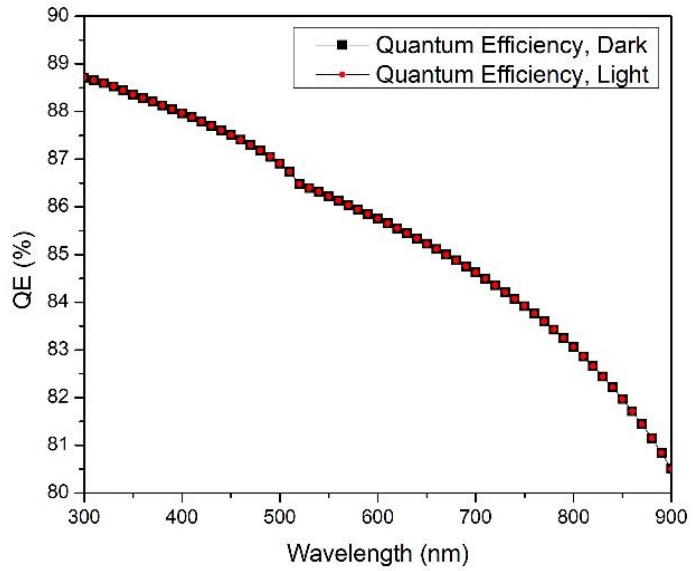

Figure 4.12: Quantum efficiency variation for p-CIGS/n-CdS/SnO_2 structure. Both dark and light curves overlapped.

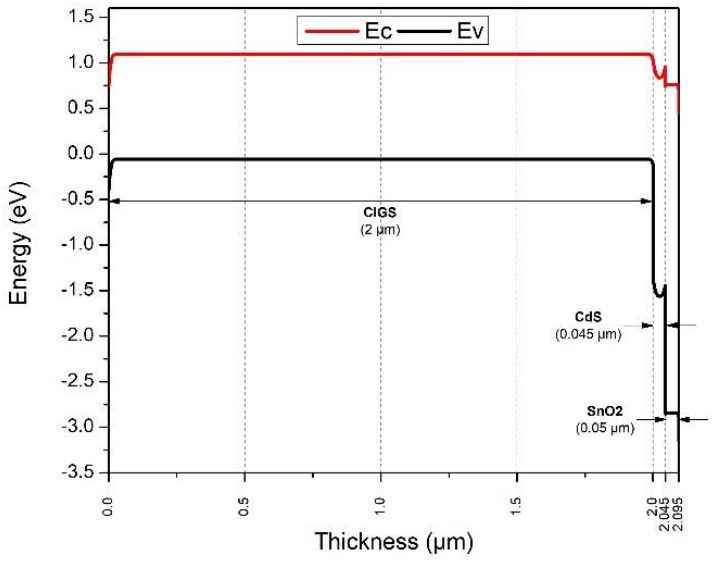

Figure 4.13: Energy band diagram for the optimized p-CIGS/n-CdS/SnO_2 structure.

4.3.3 Optimization of Solar Cell Structure III: p-CIGS/n-In_2S_3/i-ZnO/ZnO:Al

In the next cell structure considered, In_2S_3 was used to supplant CdS as the buffer layer. The bilayer of i-Zno and ZnO:Al was used as the window layer. The effect of changing the bandgap, impurity concentration and thickness of the In_2S_3 buffer layer on the solar cell characteristics was explored. Then the impact of temperature on the cell parameters was examined.

The bandgap of In_2S_3 was varied in a range of 2.1 – 2. 75 eV. Since the recombination that takes place inside the bulk CIGS would lead to little raise in efficiency if the CIGS thickness were made larger than 3 μm, the cell efficiency will not be in par with the associated cost of material and manufacturing. That is why the thickness of the CIGS layer was set to 3 μm. The donor ion concentration of the In_2S_3 layer was kept fixed at 1×10^{17} cm^{-3} and its thickness at 0.04 μm. An efficiency of around 23.58% was achieved when In_2S_3 bandgap was at 2.6 eV. Further increase in the bandgap reduced the efficiency. The same trend was observed for the fill factor, it decreased from 85.3% at 2.6 eV with further increment in the bandgap. The open-circuit voltage and the short-circuit current density also decreased when the bandgap was made higher than 2.6 eV. Keeping the In_2S_3 bandgap fixed at 2.6 eV, its impurity atom concentration was then varied from 1×10^{15} cm^{-3} to 1×10^{18} cm^{-3}. Although the open-circuit voltage showed from no- to quite insignificant changes, the short-circuit current density saw an increase from 35.81 mA/cm^2 to 35.87 mA/cm^2. The fill factor dropped to a value of around 85.30% while the efficiency increased and peaked around 23.58% at a donor concentration of 1×10^{18} cm^{-3}. All the solar cell characteristic parameters- the open-circuit voltage, short-circuit current density, fill factor and efficiency- with change in donor density of In_2S_3 are plotted in Figure 4.14 and Figure 4.15. With its bandgap at 2.6 eV and donor concentration at 1×10^{18} cm^{-3}, the In_2S_3 layer thickness was

varied from 0.04 µm to 0.2 µm. The optimum thickness for the layer was identified as the 0.04 µm since further increase in thickness caused little increment in the cell efficiency from around 23.58% compared to required larger layer thicknesses.

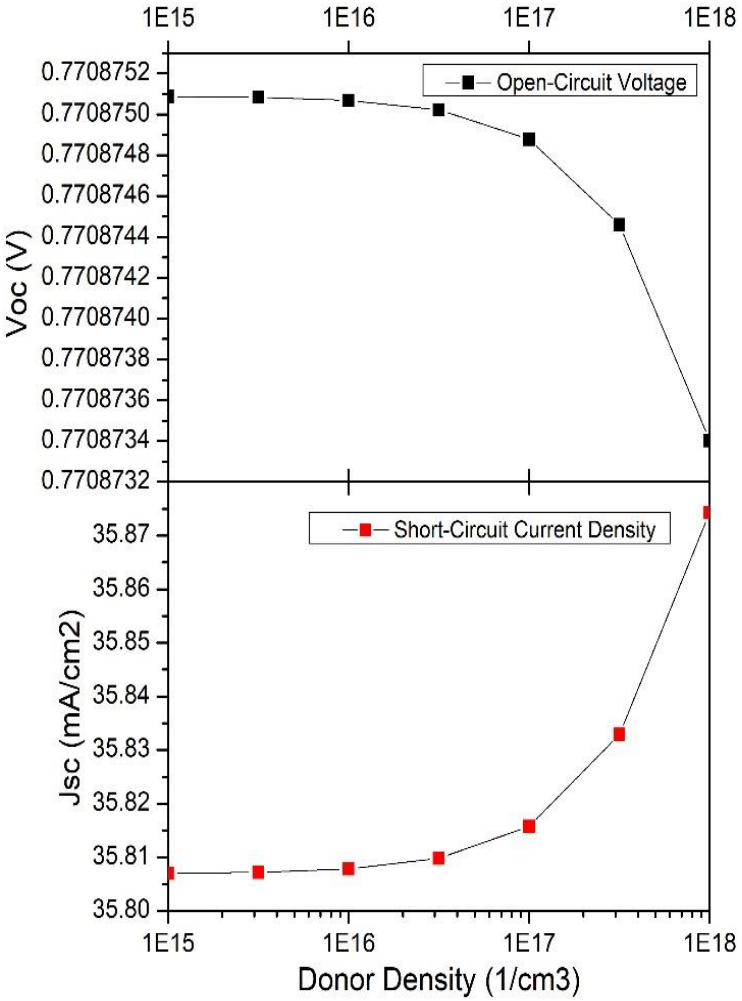

Figure 4.14: Change of V_{OC} and J_{SC} with change in donor density of In_2S_3 layer of p-CIGS/n- In_2S_3/i-ZnO/ZnO:Al structure.

The cell performance under different temperatures (280 K – 375 K) was then examined. The optimized values for In_2S_3 bandgap, its donor ion concentration and thickness were used for the simulation. At higher temperatures, bandgap values get unstable. The resulting recombination of electron and hole decreases the efficiency of the cell. The efficiency declined to a value of

around 19.7% at a temperature of 375 K (Figure 4.16). The J-V characteristics from the dark and light simulation of the p-CIGS/n- In_2S_3/i-ZnO/ZnO:Al structure are shown in Figure 4.17. The quantum efficiency of the cell is displayed in Figure 4.18. Figure 4.19 depicts the band diagram of the structure. From this section and the section 4.3.1, all the optimized parameters of the CIGS, In_2S_3 and i-ZnO layers were used to simulate the J-V characteristics, quantum efficiency and energy band diagram.

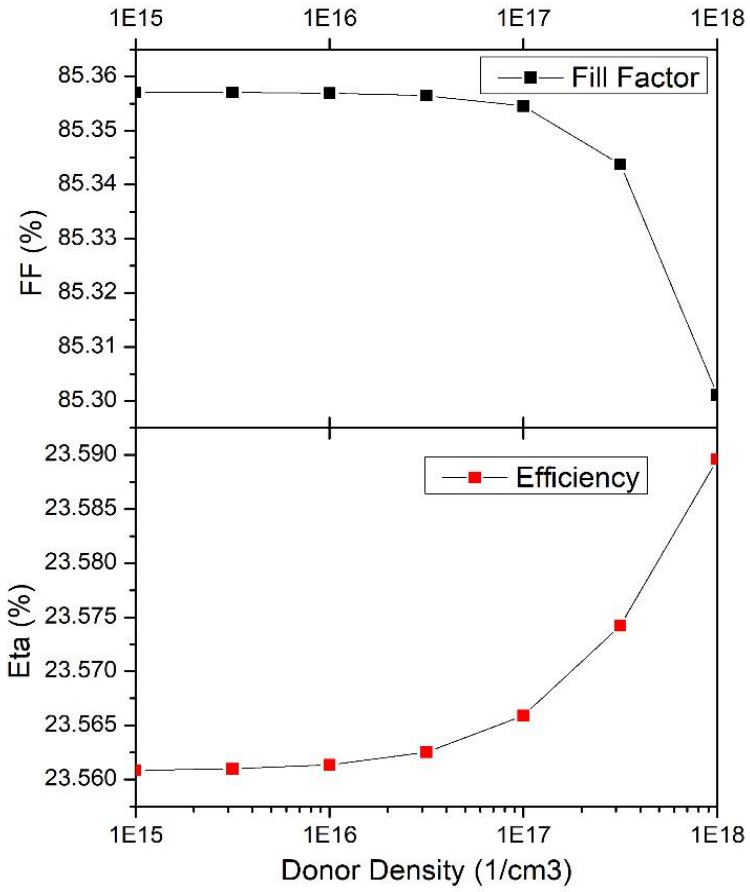

Figure 4.15: Change of fill factor and efficiency with change in donor density of In_2S_3 layer of p-CIGS/n- In_2S_3/i-ZnO/ZnO:Al structure.

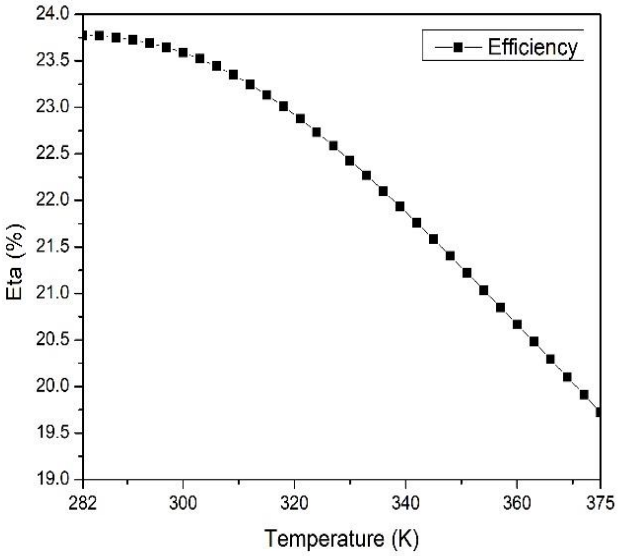

Figure 4.16: Change of efficiency with change in temperature of p-CIGS/n- In_2S_3/i-ZnO/ZnO:Al structure.

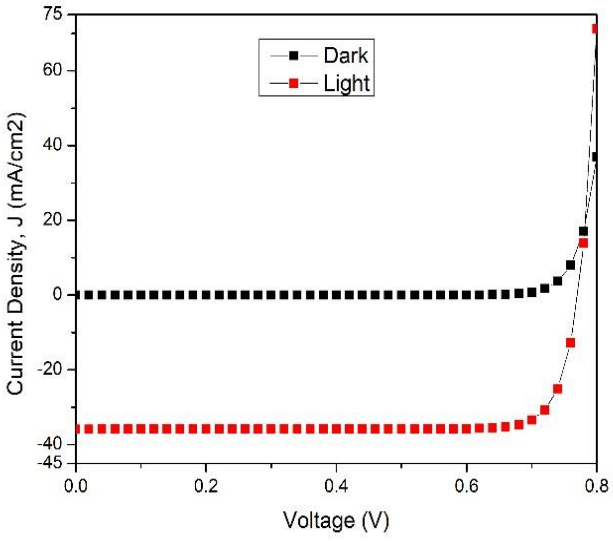

Figure 4.17: J-V characteristics of p-CIGS/n- In_2S_3/i-ZnO/ZnO:Al structure under dark and light conditions.

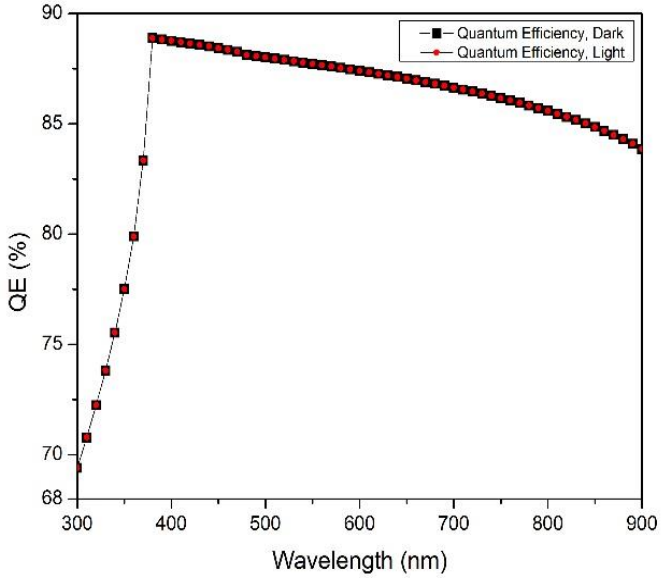

Figure 4.18: Quantum efficiency variation for p-CIGS/n- In_2S_3/i-ZnO/ZnO:Al structure. Both dark and light curves overlapped.

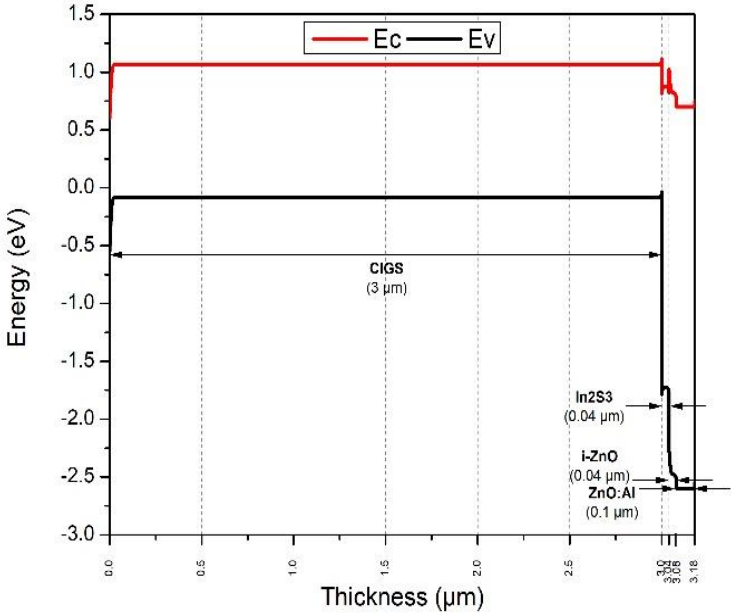

Figure 4.19: Energy band diagram for the optimized p-CIGS/n-In_2S_3/i-ZnO/ZnO:Al structure.

4.3.4 Optimization of Solar Cell Structure IV: p-CIGS/n-In_2S_3/SnO_2

The SnO_2 window layer was incorporated into the p-CIGS/n-In_2S_3 solar cell structure replacing the ZnO window layer. In this section, the effect of SnO_2 thickness variation on this cell performance is examined. The SnO_2 layer characteristic parameters are listed in Table 4.1. The optimized parameters for the CIGS and In_2S_3 layers from the section 4.3.1 and section 4.3.3 were used during the simulation of the structure. After finding the suitable window layer thickness, the cell was simulated under different temperature conditions, too.

The SnO_2 thickness was varied from 0.04 μm to 0.2 μm. The optimum thickness for the layer was chosen as 0.05 μm which accounted for an efficiency of 23.65%. Any further increase of the SnO_2 thickness caused to decrease the efficiency of the cell. All the solar cell performance parameters including the efficiency are plotted in Figure 4.20 and Figure 4.21. The fill factor showed negligible increment with increasing SnO_2 thickness. The cell was then tested for different temperatures ranging from 280 K to 375 K. While the short-circuit current density remained almost same with increasing temperature, the open circuit-voltage varied inversely. The efficiency fell to 19.79 V at 375 K (Figure 4.22). The dark and light simulation of the cell was performed. The corresponding J-V characteristics, quantum efficiency and energy band diagram of the cell are illustrated in the Figure 4.23, Figure 4.24 and Figure 4.25, respectively.

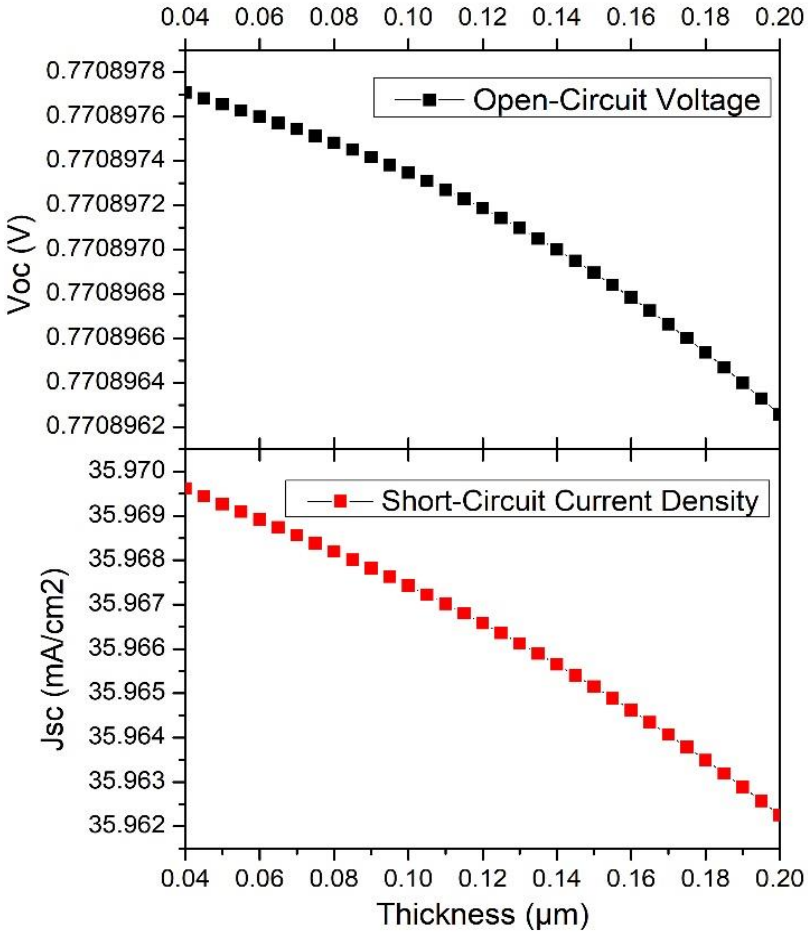

Figure 4.20: Change of V_{OC} and J_{SC} with change in SnO_2 thickness of p-CIGS/n-In_2S_3/SnO_2 structure.

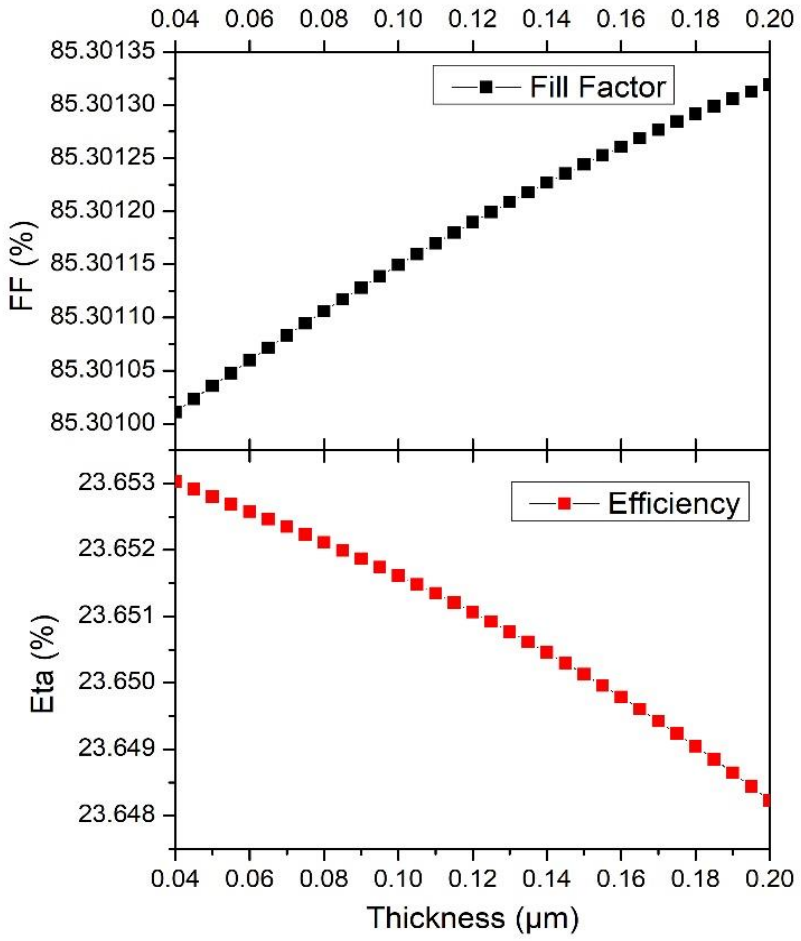

Figure 4.21: Change of fill factor and efficiency with change in SnO_2 thickness of p-CIGS/n-In_2S_3/SnO_2 structure.

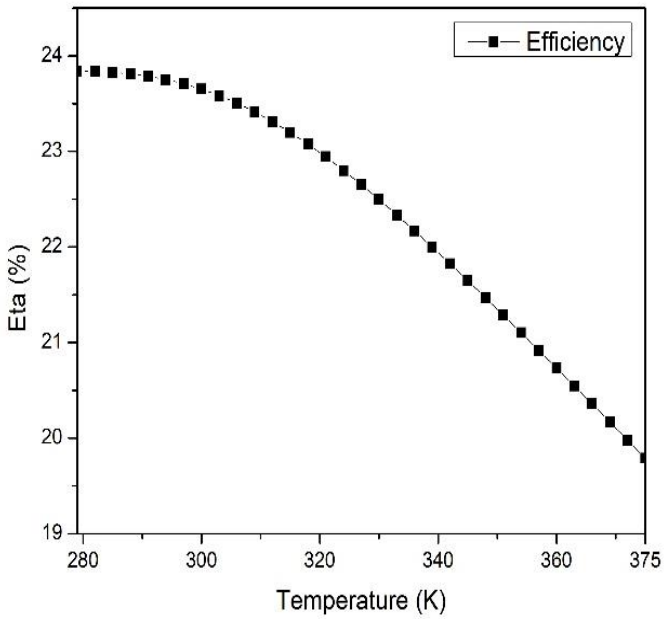

Figure 4.22: Change of efficiency with change in temperature of p-CIGS/n-In_2S_3/SnO_2 structure.

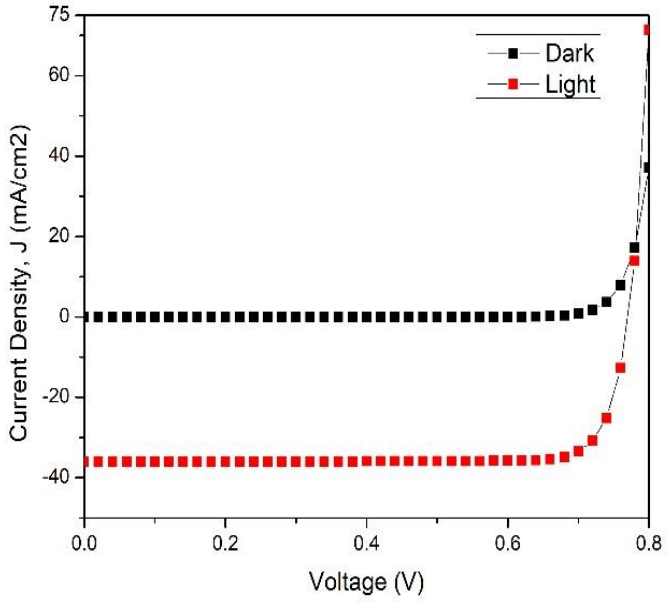

Figure 4.23: J-V characteristics of p-CIGS/n-In_2S_3/SnO_2 structure under dark and light conditions.

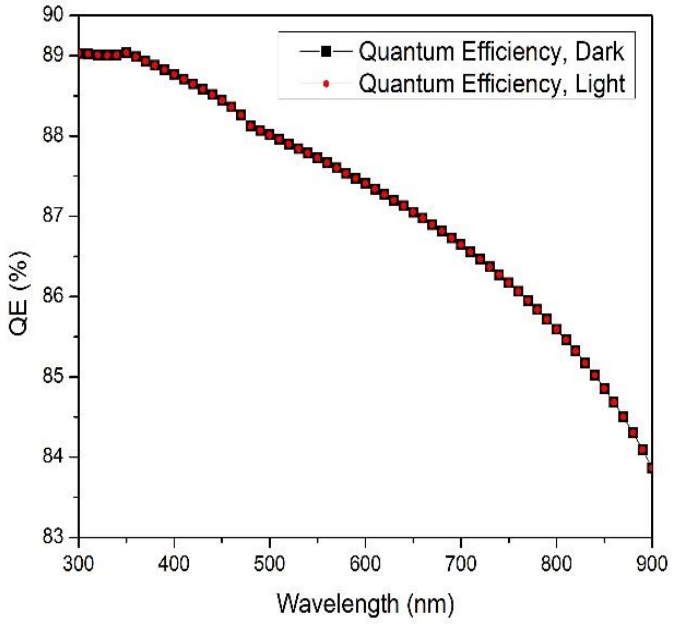

Figure 4.24: Quantum efficiency variation for p-CIGS/n-In_2S_3/SnO_2 structure. Both dark and light curves overlapped.

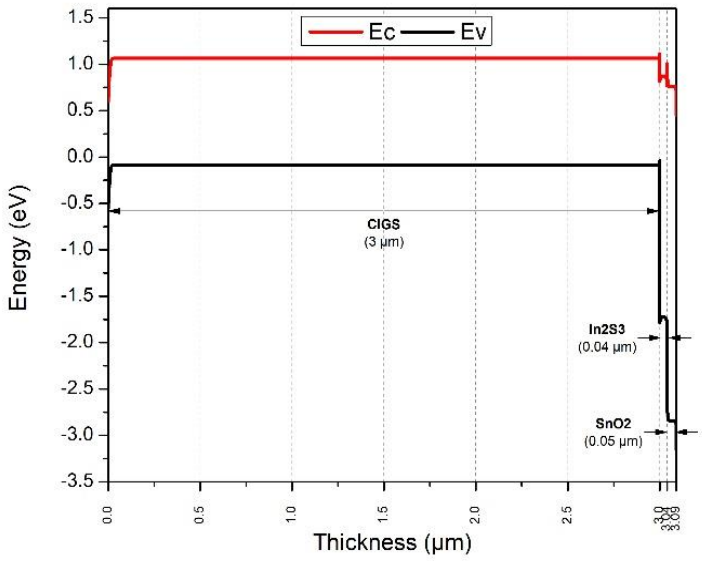

Figure 4.25: Energy band diagram for the optimized p-CIGS/n-In_2S_3/SnO_2 structure.

4.3.5 Summary of the Solar Cell Parameters of the Optimized Structures and Comparison with Other Reported Solar Cells

The solar cell characteristic parameters for the optimized structures, as discussed in the section 4.3.1 – 4.3.4, have been summarized in Table 4.2. The Cd-free structures i.e. the structures employing indium sulfide as the buffer layer (Optimized Structures III and IV) achieved higher efficiency compared to those of Cd-containing structures. However, the Cd-containing structures (Optimized Structures I and II) had thinner CIGS absorber layer (2 μm). The disadvantage of thicker CIGS absorber layer in the Structures III and IV could be somewhat compensated using SnO_2 window layer instead of the ZnO (Structure IV). By comparing the ZnO and SnO_2 containing cell structures (Structures I and II, and Structures III and IV), it could be observed that not only SnO_2 containing cell showed better performance in terms of the cell parameters, but it is thinner (0.05 μm) with respect to the ZnO window layer (0.14 μm in total).

Besides the structures optimized in the current work, some other reported CIGS solar research cell parameters have also been listed in Table 4.2. Most of those research cells beat the optimized structures in terms of short-circuit current density. Yet the optimized structures surpass all of those in terms of efficiency, open-circuit voltage, and fill factor.

Table 4.2: Solar cell parameters from laboratory research cells and the simulation of the optimized solar cell structures.

Sl.	Solar Cell Structure	V_{OC} (V)	J_{SC} (mA/cm^2)	FF (%)	H (%)	References
1.	**Laboratory Research CIGS Cell I p-CIGSSe/n-CdS/Zn(O,S,OH)$_x$/ Zn$_{0.8}$Mg$_{0.2}$O (ZMO)/ZnO:B (BZO)**	0.734	39.58	80.4	23.35 ± 0.5	[7]
2.	**Laboratory Research CIGS Cell II p-CIGS/n-CdS/(Zn,Mg)O/ZnO/ ZnO:Al**	0.741	37.80	80.60	22.60	[35]
3.	**Laboratory Research CIGS Cell III p-CIGS/n-CdS/i-ZnO/ZnO:Al**	0.746	36.60	79.30	21.7	[76]
4.	**Laboratory Research CIGS Cell IV p-CIGS/n-CdS/i-ZnO/ZnO:Al**	0.757	35.70	77.60	21	[75]
5.	**Optimized Structure I: p-CIGS/n-CdS/i-ZnO/ZnO:Al**	0.7868	34.7351	85.6549	23.4086	Proposed
6.	**Optimized Structure II: p-CIGS/n-CdS/SnO$_2$**	0.7869	34.8176	85.6958	23.4777	Proposed
7.	**Optimized Structure III: p-CIGS/n-In$_2$S$_3$/i-ZnO/ZnO:Al**	0.7709	35.8743	85.3011	23.5896	Proposed
8.	**Optimized Structure IV: p-CIGS/n-In$_2$S$_3$/ SnO$_2$**	0.7709	35.9693	85.3010	23.6528	Proposed

One of the reasons for the reported CIGS research cells having higher short-circuit current density might be a graded CIGS absorber with lower Ga/(Ga + In) (GGI) minimum and steeper GGI gradient compared to those without grading, which in turn, caused Jsc to increase in the IR region [35]. Post-deposition treatment of CIGS absorber layer with alkali fluoride, especially using heavier alkali elements such as rubidium or cesium, might have played another important role in increasing short-circuit current density [75]. The diode quality improved as the ideality factor was revealed to decrease. That might well be since the heavier alkali elements tend to push out lighter alkalis out of the CIGS absorber layer. As Nakamura et. al. reported in [7], the replacement of the CdS buffer layer by a Zn(O,S,OH)x/ZMO double buffer layer allows more blue light reach the absorber layer, owing to higher bandgap energy of the double buffer

layer compared to that of CdS. Consequently, the short-circuit current density increased. Besides this, the double buffer layer also caused suppression of minority carrier recombination at the depletion region which, too, contributed to the higher Jsc.

Despite the fact that grading of the absorber layer and the effect of the post-deposition treatment were not considered for the proposed cells, the improvement in the open-circuit voltage in combination with high enough Jsc has led to higher efficiencies for all of the proposed CIGS cell structures, including both CdS-containing and CdS-free cell structures. The efficiencies achieved by all the optimized structures either equal or exceed the present highest CIGS research cell efficiency of 23.35±0.5 %, as can be observed from Table 4.2.

Not only has the quality of environment-friendliness, but this research also illustrates that Cd-free CIGS solar cells can have the potential to surpass its counterpart containing Cd in terms of cell efficiency. In_2S_3 might be a good choice in this regard. As reported in [7], a Zn-based double buffer layer showed a superior performance to that of CdS-containing cells. This paves the way for an excellent probability of In_2S_3 being used in a double layer in association with other buffer materials. Besides, a thinner SnO_2 layer can effectively reduce the window layer thickness- replacing the conventional ZnO- which would effectively reduce the module cost. Although a thick CIGS absorber layer remains a challenge, introducing a suitable back surface field layer with CIGS absorber layer can cause the overall absorber layer thickness drastically decrease. Also, the introduction of grading/ double-grading into the CIGS absorber layer and considering post-deposition treatment of the absorber with alkali elements, in combination with the achieved simulated result in this work, are highly likely to result in further improvements in the cell efficiency. Further simulations will be needed in order to investigate these potentials.

4.4 Conclusion

The analysis of the second-generation thin film CIGS solar cell shows an improvement in their performance. For the current research we focused on the absorber, buffer and window layers of the CIGS cell. All four simulated and optimized CIGS cell structures showed better performance than the works reported so far. The In_2S_3 could effectively replace the CdS buffer layer, thereby rendering a non-toxic Cd-free CIGS solar cell. The SnO_2 in association with In_2S_3 produced the highest efficiency although it required the CIGS absorber layer to be thicker. Further modifications of the cell structure are required to reduce the CIGS layer thickness.

CHAPTER V

FUTURE WORK

The investigation of the effects of sputtering mode and parameters on the Mo thin-films that have taken place in this research holds a myriad potential. The following can be undertaken for further research in connection with this:

- Surface morphology and reflectance of the Mo thin-films may be useful to further verify the results obtained here.
- Reflectance of the Mo thin-films can be investigated to further validate the results and analysis.
- CIGS absorber layer deposited on the Mo films investigated here can verify their adhesion to the CIGS layer.
- Effect of film thickness, deposition temperature and annealing temperature may be investigated at the specified pressure and power of the single layer and multi-layer Mo thin-films.
- Film thickness and annealing temperature might further improve the properties of the films obtained here.

In the second part of the research where numerical modeling and simulation were employed to optimize the CIGS solar cell structure performance, the following could be considered for further numerical simulation and performance improvement of the cell:

- In_2S_3 material can be used in a double layer in association with other buffer materials.
- A back surface field layer might be introduced between the absorber and CIGS absorber layer.
- Effect of grading/ double-grading of bandgap of CIGS absorber layer can be considered in the numerical modeling of the cell.
- Introducing effect of post-deposition treatment of CIGS absorber layer with heavy alkali fluorides might further improve and optimize CIGS solar cell performance.

REFERENCES

[1] W. S. Ebhota and T.-C. Jen, "Fossil Fuels Environmental Challenges and the Role of Solar Photovoltaic Technology Advances in Fast Tracking Hybrid Renewable Energy System," *International Journal of Precision Engineering and Manufacturing-Green Technology,* vol. 7, no. 1, pp. 97-117, 2020/01/01 2020, doi: 10.1007/s40684-019-00101-9.

[2] C. Hunt and O. Weber, "Fossil Fuel Divestment Strategies: Financial and Carbon-Related Consequences," *Organization & Environment,* vol. 32, no. 1, pp. 41-61, 2019, doi: 10.1177/1086026618773985.

[3] J. Tsao, N. Lewis, and G. Crabtree. "Solar FAQs." https://www.sandia.gov/~jytsao/Solar FAQs.pdf (accessed August 10 2021).

[4] J. Ramanujam *et al.*, "Inorganic photovoltaics – Planar and nanostructured devices," *Progress in Materials Science,* vol. 82, pp. 294-404, 2016/09/01/ 2016, doi: https://doi.org/10.1016/j.pmatsci.2016.03.005.

[5] A. Jäger-Waldau, "PV Status Report 2016," Luxembourg, 2016.

[6] K. Yoshikawa *et al.*, "Silicon heterojunction solar cell with interdigitated back contacts for a photoconversion efficiency over 26%," *Nature Energy,* vol. 2, no. 5, p. 17032, 2017/03/20 2017, doi: 10.1038/nenergy.2017.32.

[7] M. Nakamura, K. Yamaguchi, Y. Kimoto, Y. Yasaki, T. Kato, and H. Sugimoto, "Cd-Free Cu(In,Ga)(Se,S)$_2$ Thin-Film Solar Cell With Record Efficiency of 23.35%," *IEEE Journal of Photovoltaics,* vol. 9, no. 6, pp. 1863-1867, 2019, doi: 10.1109/JPHOTOV.2019.2937218.

[8] H. Sugimoto, "High efficiency and large volume production of CIS-based modules," in *2014 IEEE 40th Photovoltaic Specialist Conference (PVSC)*, 8-13 June 2014 2014, pp. 2767-2770, doi: 10.1109/PVSC.2014.6925503.

[9] M. A. Green, E. D. Dunlop, D. H. Levi, J. Hohl-Ebinger, M. Yoshita, and A. W. Y. Ho-Baillie, "Solar cell efficiency tables (version 54)," *Progress in Photovoltaics: Research and Applications,* vol. 27, no. 7, pp. 565-575, 2019, doi: 10.1002/pip.3171.

[10] A. V. Shah *et al.*, "Basic efficiency limits, recent experimental results and novel light-

trapping schemes in a-Si:H, μc-Si:H and `micromorph tandem' solar cells," *Journal of Non-Crystalline Solids,* vol. 338-340, pp. 639-645, 2004/06/15/ 2004, doi: https://doi.org/10.1016/j.jnoncrysol.2004.03.074.

[11] A. Richter, M. Hermle, and S. W. Glunz, "Reassessment of the Limiting Efficiency for Crystalline Silicon Solar Cells," *IEEE Journal of Photovoltaics,* vol. 3, no. 4, pp. 1184-1191, 2013, doi: 10.1109/JPHOTOV.2013.2270351.

[12] C. Yan *et al.*, "Cu_2ZnSnS_4 solar cells with over 10% power conversion efficiency enabled by heterojunction heat treatment," *Nature Energy,* vol. 3, no. 9, pp. 764-772, 2018/09/01 2018, doi: 10.1038/s41560-018-0206-0.

[13] R. A and B. RM, *Journal of Applied Physics,* vol. 70, pp. R 81 - 97, 1991.

[14] Y.-C. Wang and H.-P. D. Shieh, "Double-graded bandgap in $Cu(In,Ga)Se_2$ thin film solar cells by low toxicity selenization process," *Appl. Phys. Lett.,* vol. 105, no. 7, p. 073901, 2014/08/18 2014, doi: 10.1063/1.4893713.

[15] G. D. J. Harper. "CIGS solar cell." Encyclopedia Britannica. https://www.britannica.com/technology/CIGS-solar-cell (accessed 10 August, 2021).

[16] P.-c. Huang, C.-h. Huang, M.-y. Lin, C.-y. Chou, C.-y. Hsu, and C.-g. Kuo, "The Effect of Sputtering Parameters on the Film Properties of Molybdenum Back Contact for CIGS Solar Cells," *International Journal of Photoenergy,* vol. 2013, p. 390824, 2013/04/04 2013, doi: 10.1155/2013/390824.

[17] X. Ma, D. Liu, L. Yang, S. Zuo, and M. Zhou, "Molybdenum (Mo) back contacts for CIGS solar cells," presented at the Eighth International Conference on Thin Film Physics and Applications, Osceola, FL, USA, 2013.

[18] P. J. Rostan, J. Mattheis, G. Bilger, U. Rau, and J. H. Werner, "Formation of transparent and ohmic ZnO:Al/$MoSe_2$ contacts for bifacial $Cu(In,Ga)Se_2$ solar cells and tandem structures," *Thin Solid Films,* vol. 480-481, pp. 67-70, 2005/06/01/ 2005, doi: https://doi.org/10.1016/j.tsf.2004.11.001.

[19] W. Wang *et al.*, "Device Characteristics of CZTSSe Thin-Film Solar Cells with 12.6% Efficiency," *Advanced Energy Materials,* https://doi.org/10.1002/aenm.201301465 vol. 4, no. 7, p. 1301465, 2014/05/01 2014, doi: https://doi.org/10.1002/aenm.201301465.

[20] A. C. Badgujar, S. R. Dhage, and S. V. Joshi, "Process parameter impact on properties of sputtered large-area Mo bilayers for CIGS thin film solar cell applications," *Thin Solid Films,* vol. 589, pp. 79-84, 2015/08/31/ 2015, doi: https://doi.org/10.1016/j.tsf.2015.04.046.

[21] M. Theelen *et al.*, "Influence of Mo/$MoSe_2$ microstructure on the damp heat stability of the Cu(In,Ga)Se_2 back contact molybdenum," *Thin Solid Films,* vol. 612, pp. 381-392, 2016/08/01/ 2016, doi: https://doi.org/10.1016/j.tsf.2016.06.028.

[22] N. Akcay, N. Akin Sonmez, E. P. Zaretskaya, and S. Ozcelik, "Influence of deposition pressure and power on characteristics of RF-Sputtered Mo films and investigation of sodium diffusion in the films," *Current Applied Physics,* vol. 18, no. 5, pp. 491-499, 2018/05/01/ 2018, doi: https://doi.org/10.1016/j.cap.2018.02.014.

[23] E. Moons, T. Engelhard, and D. Cahen, "Ohmic contacts to p-$CuInSe_2$ crystals," *Journal of Electronic Materials,* vol. 22, no. 3, pp. 275-280, 1993/03/01 1993, doi: 10.1007/BF02661377.

[24] S. Raud and M. A. Nicolet, "Study of the $CuInSe_2$/Mo thin film contact stability," *Thin Solid Films,* vol. 201, no. 2, pp. 361-371, 1991/06/30/ 1991, doi: https://doi.org/10.1016/0040-6090(91)90124-G.

[25] S. Ashour, S. Alkuhaimi, H. Moutinho, R. Matson, and F. Abou-Elfotouh, "Junction formation and characteristics of CdS/$CuInSe_2$/metal interfaces," *Thin Solid Films,* vol. 226, no. 1, pp. 129-134, 1993/04/15/ 1993, doi: https://doi.org/10.1016/0040-6090(93)90217-D.

[26] H.-M. Wu *et al.*, "Structure and electrical properties of Mo back contact for Cu(In, Ga)Se_2 solar cells," *Vacuum,* vol. 86, no. 12, pp. 1916-1919, 2012/07/20/ 2012, doi: https://doi.org/10.1016/j.vacuum.2012.04.036.

[27] L. Assmann, J. C. Bernède, A. Drici, C. Amory, E. Halgand, and M. Morsli, "Study of the Mo thin films and Mo/CIGS interface properties," *Applied Surface Science,* vol. 246, no. 1, pp. 159-166, 2005/06/15/ 2005, doi: https://doi.org/10.1016/j.apsusc.2004.11.020.

[28] T. Wada, N. Kohara, S. Nishiwaki, and T. Negami, "Characterization of the Cu(In,Ga)Se_2/Mo interface in CIGS solar cells," *Thin Solid Films,* vol. 387, no. 1, pp. 118-122, 2001/05/29/ 2001, doi: https://doi.org/10.1016/S0040-6090(00)01846-0.

[29] T. Wada, N. Kohara, T. Negami, and M. Nishitani, "Chemical and Structural Characterization of Cu(In,Ga)Se_2/Mo Interface in Cu(In,Ga)Se_2 Solar Cells," *Japanese Journal of Applied Physics,* vol. 35, no. Part 2, No. 10A, pp. L1253-L1256, 1996/10/01 1996, doi: 10.1143/jjap.35.l1253.

[30] D. Abou-Ras *et al.*, "Formation and characterisation of MoSe2 for Cu(In,Ga)Se2 based solar cells," *Thin Solid Films,* vol. 480-481, pp. 433-438, 2005/06/01/ 2005, doi: https://doi.org/10.1016/j.tsf.2004.11.098.

[31] Z.-H. Li, E.-S. Cho, and S. J. Kwon, "Molybdenum thin film deposited by in-line DC

magnetron sputtering as a back contact for Cu(In,Ga)Se2 solar cells," *Applied Surface Science,* vol. 257, no. 22, pp. 9682-9688, 2011/09/01/ 2011, doi: https://doi.org/10.1016/j.apsusc.2011.06.101.

[32] J. H. Scofield *et al.*, "Sodium diffusion, selenization, and microstructural effects associated with various molybdenum back contact layers for CIS-based solar cells," in *Proceedings of 1994 IEEE 1st World Conference on Photovoltaic Energy Conversion - WCPEC (A Joint Conference of PVSC, PVSEC and PSEC)*, 5-9 Dec. 1994 1994, vol. 1, pp. 164-167 vol.1, doi: 10.1109/WCPEC.1994.519833.

[33] J. Li *et al.*, "Density profiles in sputtered molybdenum thin films and their effects on sodium diffusion in $Cu(In_xGa_{1-x})Se_2$ photovoltaics," in *2011 37th IEEE Photovoltaic Specialists Conference*, 19-24 June 2011 2011, pp. 002749-002752, doi: 10.1109/PVSC.2011.6186516.

[34] K. H. Ong *et al.*, "Review on Substrate and Molybdenum Back Contact in CIGS Thin Film Solar Cell," *International Journal of Photoenergy,* vol. 2018, p. 9106269, 2018/09/12 2018, doi: 10.1155/2018/9106269.

[35] P. Jackson, R. Wuerz, D. Hariskos, E. Lotter, W. Witte, and M. Powalla, "Effects of heavy alkali elements in $Cu(In,Ga)Se_2$ solar cells with efficiencies up to 22.6%," *physica status solidi (RRL) – Rapid Research Letters,* https://doi.org/10.1002/pssr.201600199 vol. 10, no. 8, pp. 583-586, 2016/08/01 2016, doi: https://doi.org/10.1002/pssr.201600199.

[36] S. Karthikeyan, L. Zhang, S. Hwang, and S. A. Campbell, "Experimental scheme for a stable molybdenum bilayer back contacts for photovoltaic applications," *Applied Surface Science,* vol. 449, pp. 647-653, 2018/08/15/ 2018, doi: https://doi.org/10.1016/j.apsusc.2017.11.277.

[37] P. M. P. Salomé, H. Rodriguez-Alvarez, and S. Sadewasser, "Incorporation of alkali metals in chalcogenide solar cells," *Solar Energy Materials and Solar Cells,* vol. 143, pp. 9-20, 2015/12/01/ 2015, doi: https://doi.org/10.1016/j.solmat.2015.06.011.

[38] W. Li, X. Yan, A. G. Aberle, and S. Venkataraj, "Analysis of Microstructure and Surface Morphology of Sputter Deposited Molybdenum Back Contacts for CIGS Solar Cells," *Procedia Engineering,* vol. 139, pp. 1-6, 2016/01/01/ 2016, doi: https://doi.org/10.1016/j.proeng.2015.09.231.

[39] G. Gordillo, M. Grizález, and L. C. Hernandez, "Structural and electrical properties of DC sputtered molybdenum films," *Solar Energy Materials and Solar Cells,* vol. 51, no. 3, pp. 327-337, 1998/02/27/ 1998, doi: https://doi.org/10.1016/S0927-0248(97)00236-5.

[40] H. Zhu *et al.*, "DC and RF sputtered molybdenum electrodes for Cu(In,Ga)Se_2 thin film solar cells," *Applied Surface Science,* vol. 465, pp. 48-55, 2019/01/28/ 2019, doi: https://doi.org/10.1016/j.apsusc.2018.09.130.

[41] X. Liu, H. Cui, X. Hao, S. Huang, and G. Conibeer, "Effect of vacuum thermal annealing on a molybdenum bilayer back contact deposited by radio-frequency magnetron sputtering for chalcogenide- and kesterite-based solar cells," *J. Korean Phys. Soc.,* vol. 71, no. 12, pp. 968-973, 2017/12/01 2017, doi: 10.3938/jkps.71.968.

[42] F. Jingxue *et al.*, "Preparation and optimization of a molybdenum electrode for CIGS solar cells," *AIP Adv.,* vol. 6, no. 11, p. 115210, 2016, doi: 10.1063/1.4967427.

[43] P. Chelvanathan *et al.*, "Effects of RF magnetron sputtering deposition process parameters on the properties of molybdenum thin films," *Thin Solid Films,* vol. 638, pp. 213-219, 2017/09/30/ 2017, doi: https://doi.org/10.1016/j.tsf.2017.07.057.

[44] J. C. o. P. D. Standards. X.-R.D.D. Cards

[45] F. Y.C., L. D.E., and L. D.N., *Journal of Applied Physics,* vol. 76, 7311-6, 1994.

[46] J. G. Che, C. T. Chan, W. E. Jian, and T. C. Leung, "Surface atomic structures, surface energies, and equilibrium crystal shape of molybdenum," *Physical Review B,* vol. 57, no. 3, pp. 1875-1880, 01/15/ 1998, doi: 10.1103/PhysRevB.57.1875.

[47] A. E, B. F, A. A, C. A, and E. I., *Wear,* vol. 259:814-9, 2005.

[48] X. Liu, X. Hao, M. A. Green, S. Huang, and G. Conibeer, in *COMMAD*, Melbourne, Australia, December 12 - 14 2012, p. 61.

[49] H. Zhao, J. Xie, and A. Mao, "Effects of Bottom Layer Sputtering Pressures and Annealing Temperatures on the Microstructures, Electrical and Optical Properties of Mo Bilayer Films Deposited by RF/DC Magnetron Sputtering," *Applied Sciences,* vol. 9, no. 7, 2019, doi: 10.3390/app9071395.

[50] G. Zoppi, N. S. Beattie, J. D. Major, R. W. Miles, and I. Forbes, "Electrical, morphological and structural properties of RF magnetron sputtered Mo thin films for application in thin film photovoltaic solar cells," *J. Mater. Sci.,* vol. 46, no. 14, pp. 4913-4921, 2011/07/01 2011, doi: 10.1007/s10853-011-5404-0.

[51] V. Teixeira and M. Andritschky, "Influence of Sputter Gas Pressure and Substrate Bias on Intrinsic Stress and Crystallinity of Coatings Produced by Magnetron Sputtering," in *Multicomponent and Multilayered Thin Films for Advanced Microtechnologies: Techniques, Fundamentals and Devices*, O. Auciello and J. Engemann Eds. Dordrecht: Springer Netherlands, 1993, pp. 121-127.

[52] T. Nakano and S. Baba, "A hybrid simulation of high pressure sputtering, combining the Monte Carlo method and the diffusive approach," *Thin Solid Films,* vol. 343-344, pp. 24-26, 1999/04/01/ 1999, doi: https://doi.org/10.1016/S0040-6090(99)80012-1.

[53] M. Andritschky and V. Teixeira, "Residual stress and adhesion of molybdenum coatings produced by magnetron sputtering," *Vacuum,* vol. 43, no. 5, pp. 455-458, 1992/05/01/ 1992, doi: https://doi.org/10.1016/0042-207X(92)90055-2.

[54] A. A. Kadam, N. G. Dhere, P. Holloway, and E. Law, "Study of molybdenum back contact layer to achieve adherent and efficient $CIGS_2$ absorber thin-film solar cells," *Journal of Vacuum Science & Technology A: Vacuum, Surfaces, and Films,* vol. 23, no. 4, pp. 1197-1201, 2005, doi: 10.1116/1.1889440.

[55] H. A. Al-Thani *et al.*, "The effect of Mo back contact on Na out-diffusion and device performance of Mo/Cu(In,Ga)Se_2/CdS/ZnO solar cells," in *Conference Record of the Twenty-Ninth IEEE Photovoltaic Specialists Conference, 2002.*, 19-24 May 2002 2002, pp. 720-723, doi: 10.1109/PVSC.2002.1190666.

[56] J.-H. Yoon *et al.*, "Optical analysis of the microstructure of a Mo back contact for Cu(In,Ga)Se_2 solar cells and its effects on Mo film properties and Na diffusivity," *Solar Energy Materials and Solar Cells,* vol. 95, no. 11, pp. 2959-2964, 2011/11/01/ 2011, doi: https://doi.org/10.1016/j.solmat.2011.02.030.

[57] R. E. Hummel, *Electronic Properties of Materials*, 4th ed. Springer.

[58] B. R. Watts, "Calculation of electrical resistivity produced by dislocations in various metals," *Journal of Physics F: Metal Physics,* vol. 18, no. 6, pp. 1197-1209, 1988/06 1988, doi: 10.1088/0305-4608/18/6/022.

[59] T. Ungár, I. Dragomir, Á. Révész, and A. Borbély, "The contrast factors of dislocations in cubic crystals: the dislocation model of strain anisotropy in practice," *Journal of Applied Crystallography,* https://doi.org/10.1107/S0021889899009334 vol. 32, no. 5, pp. 992-1002, 1999/10/01 1999, doi: https://doi.org/10.1107/S0021889899009334.

[60] M. Wilkens, "The determination of density and distribution of dislocations in deformed single crystals from broadened X-ray diffraction profiles," *physica status solidi (a),* https://doi.org/10.1002/pssa.19700020224 vol. 2, no. 2, pp. 359-370, 1970/06/16 1970, doi: https://doi.org/10.1002/pssa.19700020224.

[61] E. H. Sondheimer, "The mean free path of electrons in metals," *Advances in Physics,* vol. 50, no. 6, pp. 499-537, 2001, doi: 10.1080/00018730110102187.

[62] F. Warkusz, "Grain boundary electron scattering in the total film conduction model,"

Thin Solid Films, vol. 62, no. 2, pp. 247-253, 1979/09/17/ 1979, doi: https://doi.org/10.1016/0040-6090(79)90312-2.

[63] A. F. Mayadas and M. Shatzkes, "Electrical-Resistivity Model for Polycrystalline Films: the Case of Arbitrary Reflection at External Surfaces," *Physical Review B,* vol. 1, no. 4, pp. 1382-1389, 02/15/ 1970, doi: 10.1103/PhysRevB.1.1382.

[64] B. R. Watts, "The contribution of the long-range strain field of dislocations in metals to their electrical resistivity," *Journal of Physics F: Metal Physics,* vol. 18, no. 6, pp. 1183-1195, 1988/06 1988, doi: 10.1088/0305-4608/18/6/021.

[65] D. Rafaja *et al.*, "Effect of the deposition process and substrate temperature on the microstructure defects and electrical conductivity of molybdenum thin films," *Thin Solid Films,* vol. 528, pp. 42-48, 2013/01/15/ 2013, doi: https://doi.org/10.1016/j.tsf.2012.06.087.

[66] S. A. Pethe, E. Takahashi, A. Kaul, and N. G. Dhere, "Effect of sputtering process parameters on film properties of molybdenum back contact," *Solar Energy Materials and Solar Cells,* vol. 100, pp. 1-5, 2012/05/01/ 2012, doi: https://doi.org/10.1016/j.solmat.2011.11.038.

[67] G. Gordillo, F. Mesa, and C. Calderón, "Electrical and Morphological Properties of Low Resistivity Mo thin Films Prepared by Magnetron Sputtering," *Brazilian Journal of Physics,* vol. 36, pp. 982-985, 09/01 2006, doi: 10.1590/S0103-97332006000600049.

[68] E. R. Jette and F. Foote, "Precision Determination of Lattice Constants," *The Journal of Chemical Physics,* vol. 3, no. 10, pp. 605-616, 1935/10/01 1935, doi: 10.1063/1.1749562.

[69] Y. Huang, S. Gao, Y. Tang, J. Ao, W. Yuan, and L. Lu, "The multi-functional stack design of a molybdenum back contact prepared by pulsed DC magnetron sputtering," *Thin Solid Films,* vol. 616, pp. 820-827, 2016/10/01/ 2016, doi: https://doi.org/10.1016/j.tsf.2016.09.058.

[70] J. H. Scofield, A. Duda, D. Albin, B. L. Ballard, and P. K. Predecki, "Sputtered molybdenum bilayer back contact for copper indium diselenide-based polycrystalline thin-film solar cells," *Thin Solid Films,* vol. 260, no. 1, pp. 26-31, 1995/05/01/ 1995, doi: https://doi.org/10.1016/0040-6090(94)06462-8.

[71] Y. G. Wu, E. H. Cao, Z. S. Wang, J. M. Wei, W. X. Tang, and L. Y. Chen, "Stress anisotropy in circular planar magnetron sputter deposited molybdenum films and its annealing effect," *Applied Physics A,* vol. 76, no. 2, pp. 147-152, 2003/02/01 2003, doi: 10.1007/s003390201314.

[72] K. Ogawa, T. Ohkoshi, T. Takeuchi, T. Mizoguchi, and T. Masumoto, "Nucleation and

Growth of Stress Relief Patterns in Sputtered Molybdenum Films," *Japanese Journal of Applied Physics,* vol. 25, no. Part 1, No. 5, pp. 695-700, 1986/05/20 1986, doi: 10.1143/jjap.25.695.

[73] K. Ernits *et al.*, "Characterisation of ultrasonically sprayed In_xS_y buffer layers for Cu(In,Ga)Se_2 solar cells," *Thin Solid Films,* vol. 515, pp. 6051-6054, 05/01 2007, doi: 10.1016/j.tsf.2006.12.168.

[74] M. Burgelman, P. Nollet, and S. Degrave, "Modelling polycrystalline semiconductor solar cells," *Thin Solid Films,* vol. 361-362, pp. 527-532, 2000/02/21/ 2000, doi: https://doi.org/10.1016/S0040-6090(99)00825-1.

[75] D. Herrmann *et al.*, "CIGS module manufacturing with high deposition rates and efficiencies," in *2014 IEEE 40th Photovoltaic Specialist Conference (PVSC)*, 8-13 June 2014 2014, pp. 2775-2777, doi: 10.1109/PVSC.2014.6925505.

[76] P. Jackson *et al.*, "Properties of Cu(In,Ga)Se2 solar cells with new record efficiencies up to 21.7%," *physica status solidi (RRL) – Rapid Research Letters,* https://doi.org/10.1002/pssr.201409520 vol. 9, no. 1, pp. 28-31, 2015/01/01 2015, doi: https://doi.org/10.1002/pssr.201409520.

BIOGRAPHICAL SKETCH

Meah Imtiaz Zulkarnain earned his MS in Engineering (Major: Electrical Engineering) from The University of Texas Rio Grande Valley (UTRGV) in August 2021. He earned his B.Sc in Electrical and Electronic Engineering from Khulna University of Engineering & Technology (KUET) of Bangladesh in 2012. Before joining UTRGV, he worked as a faculty member at the Department of Electrical and Electronic Engineering of International Islamic University Chittagong (IIUC) of Bangladesh for several years right after his graduation from KUET. He was awarded Presidential Graduate Research Assistantship (PGRA) to pursue his MS at the UTRGV. At UTRGV, he served as the graduate research and teaching assistant. His research interests include but not limited to fabrication and characterization of semiconductor materials and devices for applications ranging from green energy to microfluidic devices. He published one conference paper at the conference IMECE 2020 on the numerical modeling and performance analysis of CIGS solar cell which CHAPTER IV of this thesis is based on. He had been part of other research, too- one paper on the characterization of SiO_2/Si thin-film has been accepted for publication and presentation at IMECE 2021, and another one on microfluidic device at the conference FEDSM 2021. He is planning to submit another paper on the fabrication and characterization of Mo thin-films (based on CHAPTER III of this thesis) in a journal. Zulkarnain can be reached at imtiaz.zulkarnain@gmail.com.